2007

Investigation of ZrNi, ZrMn2 and Zn(BH4)2 metal/complex hydrides for hydrogen storage

Diego Escobar
University of South Florida

Scholar Commons Citation

Escobar, Diego, "Investigation of ZrNi, ZrMn2 and Zn(BH4)2 metal/complex hydrides for hydrogen storage" (2007). *Graduate Theses and Dissertations.*
http://scholarcommons.usf.edu/etd/701

Investigation of ZrNi, $ZrMn_2$ and $Zn(BH_4)_2$ Metal/Complex Hydrides for Hydrogen Storage

by

Diego Escobar

A thesis submitted in partial fulfillment
of the requirements for the degree of
Master of Science in Electrical Engineering
Department of Electrical Engineering
College of Engineering
University of South Florida

Major Professor: Elias K. Stefanakos, Ph.D., P.E.
Sesha S. Srinivasan, Ph.D.
Burton Krakow, Ph.D.
John T. Wolan, Ph.D.

Date of Approval:
March 23, 2007

Keywords: doping effect, catalyst, hydrogen absorption, hydride compressor,
mechanochemical synthesis, kinetics

ACKNOWLEDGEMENTS

I would like to express my deepest appreciation and gratitude to my advisor, Dr. Elias K. Stefanakos for his invaluable guidance, encouragement and support during the course of this research. His enthusiasm in this work has been a great inspiration. I want to express my special thanks to Dr. Srinivasan and Dr. Krakow for all their work, time and knowledge that they offered to me. Thanks are due to Dr. Wolan, for serving as a member of my thesis committee.

Special thanks are also extended Matt Smith, Michael Ulrich, Luis Rivera and other colleagues in the Clean Energy Research Center. I am greatly indebted to my family in Colombia and in the USA for their constant encouragement, support and faith in me.

TABLE OF CONTENTS

LIST OF TABLES

LIST OF FIGURES

LIST OF ABBREVIATIONS

DSC – Differential Scanning Calorimetry

XRD – X-Ray Diffraction

SDT – Simultaneous DSC and TGA

SEM – Scanning Electron Microscope

EDS – Energy Dispersive Spectroscopy

FT-IR – Fourier Transform Infrared Spectrometer

TGA – Thermo Gravimetric Analysis

BM – Ball Mill

PCT – Pressure Composition Temperature

TCD – Thermal Conductivity Detector

TPD – Temperature Programmed Desorption

TPR – Temperature Programmed Reaction

GC/MS – Gas Chromatography Mass Spectroscopy

INVESTIGATION OF ZrNi, $ZrMn_2$ AND $Zn(BH_4)_2$ METAL/COMPLEX HYDRIDES FOR HYDROGEN STORAGE

Diego Escobar

ABSTRACT

The demand for efficient and clean fuel alternatives has been increasing in recent years and is expected to become more pronounced in the future. Utilization of hydrogen as a fuel is one of the most promising energy resources due to its easy production, abundance, regeneration and not creation of greenhouse gases during its combustion. Although gaseous hydrogen has a very high energy content per unit weight, its volumetric energy density is rather low. The large scale use of hydrogen as a fuel crucially depends on the development of compact hydrogen storage materials with a high mass content of hydrogen relative to total mass and to volume.

Certain metals and alloys are capable of reversibly absorbing large amounts of hydrogen to form metal hydrides. They exhibit the highest volumetric densities of hydrogen and are very promising for hydrogen storage because of their efficiency, cost and safety. Some of the metal hydride families can also be used in hydrogen compressors.

The objective of this work is to investigate the synthesis and characterization behavior of intermetallic alloys ($ZrMn_2$, ZrNi) for hydrogen compression and of complex hydrides ($Zn(BH_4)_2$) for on-board hydrogen storage. An overview of hydrogen as a fuel and its storage means is provided, synthesis and characterization methods of metal hydrides are presented and the effect of mechanical milling and the catalytic doping of metal/complex hydrides are investigated in detail. The hydrogen storage alloys (hydrides) are extensively characterized using various analytical tools such as: XRD, SEM, EDS, TCD, FTIR and GC/MS. The thermal (heat flow and weight loss) and volumetric (storage capacity, kinetics, cycle life, etc) analysis have been carried out via DSC/TGA and high pressure PCT apparatus. Finally conclusions and recommendations for future work are provided to improve the absorption/desorption cycle of hydrogen storage in the compounds under investigation.

CHAPTER 1

INTRODUCTION

The world-wide power demand and consumption (Figure 1.1), is estimated in about 10,000 million equivalent tons of petroleum [1], it is covered in more than 87% by fossil fuels like the coal, petroleum and natural gas. This dependency has important economic and environmental repercussions. For the economic point of view, it is possible to emphasize that its production is centralized in certain zones of the world; it's governed primarily by political factors, which causes high and volatile prices.

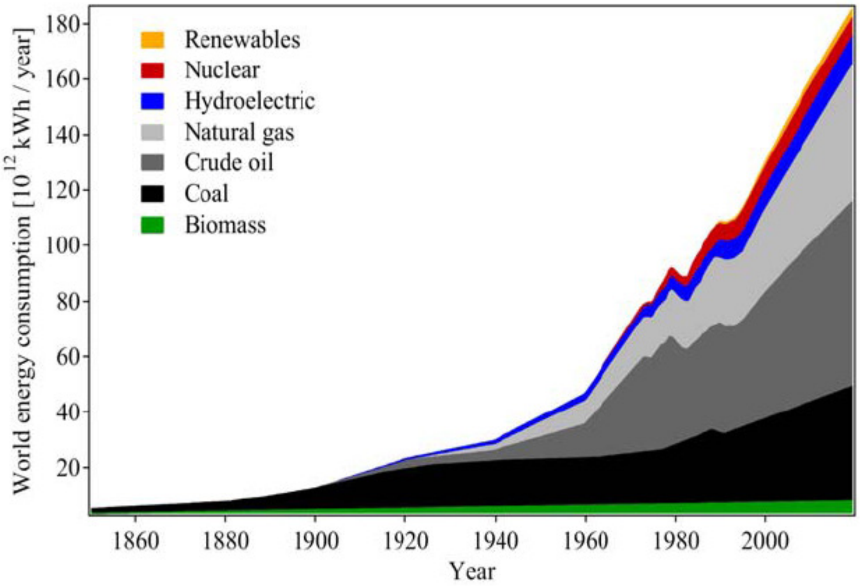

Figure 1.1 World energy consumption [2]

The population of human beings has increased in the last century by a factor of 6 but the energy consumption by a factor of 80 [3]. The world wide average continuous power consumption today is 2 kW/person. In the USA the power consumption is in average 10 kW/person and in Europe about 5 kW/person. Two billion people on earth do not consume any fossil fuels at all [1]. In absence of viable alternatives, the exhaustion of the petroleum reserves, expected in no more than 40 years [1], will cause a progressive increment in price until the levels reached might affect the global economic development.

As for the environmental concern, the fossil fuel combustion constitutes the main cause of emission of the greenhouse gases (carbon dioxide), responsible for the global warming effect of our planet. The major problem is the fact that a large amount, approximately 98% of carbon dioxide on earth is dissolved in the water of the oceans ($7.5 \cdot 10^{14}$ kg in the atmosphere, $4.1 \cdot 10^{16}$ kg in the ocean). Increasing temperature of water by approximately 3%/K decreases the solubility of carbon dioxide. If the average temperature of the oceans increases, the carbon dioxide solubility equilibrium between atmosphere and ocean shifts towards the atmosphere and leads to an additional increase of the greenhouse gas in the atmosphere.

This situation is not sustainable in the mid term and it points to be handled from the public administrations. A controlled transition towards a new form of production and consumption of power that is clean, safe and trustworthy is indeed mandatory.

1.1 Hydrogen: fuel of the future

Outlining an evolution of energy carriers towards more hydrogen rich fuels to avoid carbon dioxide emission shows how hydrogen is the ultimate end of the progression:

$$C_7H_8 \text{ (coal)} \rightarrow -CH_2- \text{ (oil)} \rightarrow CH_4 \text{ (natural gas)} \rightarrow H_2 \text{ (hydrogen)} \qquad (1.1)$$

The series also shows a development going from a solid to a liquid and then finally to a gaseous state energy carrier. Hydrogen is also viewed as the most promising clean fuel of the future because of its abundance (however, less than 1% is present as molecular hydrogen gas H_2), easy production and nonpolluting nature when burned [4,5]. It has been estimated that hydrogen makes up more than 90% of all the atoms or 75% of the mass of the universe [2].

Hydrogen is the cleanest fuel, and has a heating value three times higher than petroleum, hydrogen has the highest ratio number of valence electrons to protons (and neutrons) of all the periodic table of elements, one electron is accompanied by only one proton, the energy gain per electron is very high. The energy per mass of hydrogen ($33.3\ \text{kWh}\cdot\text{kg}^{-1}$) is almost three times larger than that of other chemical fuels (Table 1.1), e.g. liquid hydrocarbons ($12.4\ \text{kWh}\cdot\text{kg}^{-1}$) [1]. That means that the energy content of 0.33 kg of hydrogen corresponds to the energy content of 0.89 kg of gasoline.

Table 1.1 Properties of the fuels hydrogen, methane (natural gas) and gasoline [1]

Properties	Units	Hydrogen H_2	Methane CH_4	Gasoline $(-CH_2-)_n$
Lower heating value	[kWh $\cdot$kg^{-1}]	33.33	13.9	12.4
Higher heating value	[kWh $\cdot$kg^{-1}]	39.4	15.4	13.63
Self ignition temperature	[°C]	585	540	228-501
Flame temperature	[°C]	2045	1875	2200
Ignition limits in air	[Vol. %]	4-75	5.3-15	1.0-7.6
Min. ignition energy	[mWs]	0.02	0.29	0.24
Flame propagation in air	[m $\cdot$s^{-1}]	2.65	0.4	0.4
Detonation limits	[Vol. %]	13-65	6.3-13.5	1.1-3.3
Detonation velocity	[km.s^{-1}]	1.48-2.15	1.39-1.64	1.4-1.7
Explosion energy	[kg TNT.m^{-3}]	2.02	7.03	44.22

The term hydrogen economy responds to a future vision where this gas, generated by clean and economic means, would serve to fill the necessities of the society. This idea would reduce the present dependency on fossil fuels, since hydrogen could be generated from other primary sources like the renewable or nuclear ones. It also would diminish the atmospheric contamination and the emission of greenhouse gases, since the only by-product generated by hydrogen oxidation is water [6].

1.2 Present obstacles for hydrogen as a fuel

Although important technological advances have been made, the implementation of the hydrogen economy is not immediate and still requires answering important technological, economical and social challenges that are described below. From the point of view of the hydrogen production, it is necessary to consider that the present methods are expensive and are based mainly on turning fossil fuels into hydrogen gas at high pressure and temperature conditions. The processes based on renewable or nuclear energy are not developed enough and at an industrial level its cost could be even greater. On the other hand, in order to supply a global demand of this type of energy, a system of hydrogen distribution needs to be developed similar to the existing one for gasoline. Hydrogen storage is yet another challenge even more complicated to solve since the hydrogen state at STP is gas. At the present time, the development of solid-state absorbers of hydrogen (e.g. metal hydrides or complex hydrides) is being investigated for their feasibility. These systems show very high volumetric storage densities on a materials basis [7]. In the present study, an analysis of hydrogen storage is presented focusing on the interactions of hydrogen in metal.

The present price of fuel cells and their reliability are considered another important obstacle for the massive application of this technology. The use of electrodes with noble metals catalysts like palladium and platinum, with an elevated market price, and the poisoning problems, that dictate use of ultra pure hydrogen, are still in the process of investigation. Other obstacles to overcome are the security and safety, since hydrogen is inflammable and highly explosive when in contact with the oxygen of the atmosphere. For these reasons specific security norms are likely, which would be different from those used for other compounds like gasoline, butane and natural gas.

1.3 Project goals

The purpose of this project is to enhance knowledge of the fundamental interactions which hydrogen makes with metals and to use this comprehension to improve the behavior of these metal hydrides in hydrogen storage/compression applications. This project has three specific objectives:

- To develop metal hydride materials for hydrogen storage and hydrogen compression applications. Different techniques were used for synthesizing metal hydrides; the most important was the mechanochemical process where a planetary ball mill was used to make the metal/complex hydrides.
- To characterize metal hydride properties using analytical tools such as: XRD, SEM, EDS, FTIR, DSC/TGA, GC/MS, TCD and PCT in order to identify the hydrogen storage capacity, kinetics, cycle life, metal hydride structure, etc.
- To improve the physical properties which currently limit the usefulness of certain metal/complex hydrides for hydrogen storage application, this includes improving absorption and desorption kinetics, activation, purity and thermodynamic stability.

CHAPTER 2

HYDROGEN PRODUCTION AND STORAGE

2.1 Hydrogen production

2.1.1 Production of hydrogen based on fossil raw materials

At the present time, approximately 96% of the world-wide hydrogen production is obtained from fossil raw materials. All these methods involved obtaining the gas by one of the processes whose reactions are described below [8,9]:

- Reformer reaction (for methane):

  $CH_4 + 2H_2O \leftrightarrow CO_2 + 4H_2$ ($\Delta H_0 = +164$ kJ/mol; typical operation temperature 850 °C) (2.1)

  $CH_4 + H_2O \leftrightarrow CO + 3H_2$ ($\Delta H_0 = +205$ kJ/mol; o. temp. 1050 °C) (2.2)

- CO shift reaction (favored at lower temperature):

  $CO + H_2O \leftrightarrow CO_2 + H_2$ (operation temperature 130 °C) (2.3)

- Partial oxidation - reformer reaction:

  Natural gas: $CH_4 + \frac{1}{2}O_2 \rightarrow CO + 2H_2$ (1350°C) (Synthesis Gas) (2.4)

As it can be seen, the reaction products consist of mixtures of hydrogen, carbon monoxide (main products), carbon dioxide, water added in excess and other products formed in secondary reactions. The product proportions depend on the raw materials used. It is necessary to eliminate the remaining components until the hydrogen is sufficiently pure for its subsequent applications; it can be demanding for some fuel cells.

2.1.2 Production of hydrogen using renewable energy

It is known that over 70% of the earth is covered with water. The content of hydrogen in water measured by weight is 11.2%. There is definitely an abundant supply. The advantage in using hydrogen as fuel is that, during combustion, it binds itself to the oxygen in the air, and the by-product is water. Hydrogen can be produced from water by electrolysis. If the electricity is produced from a renewable technology (such as solar, hydro or wind) [8,9] then this process is free from greenhouse gases such as CO_2, CO, etc. The electrochemical splitting of water is well known and is given by the following equation:

$$H_2O \rightarrow H_2 + \frac{1}{2}O_2 \tag{2.5}$$

An important factor to consider is the recent developments to apply clean energies to the water electrolysis, like in the photovoltaic cell. The most commonly used equipment is the alkaline electrolyzer, which uses an alkaline solution, typically potassium hydroxide as an electrolyte. The reactions that take place in these systems are the following ones:

Cathode: $2H_2O \rightarrow H_2 + 2OH + 2e^-$ (2.6)

Anode: $2OH^- \rightarrow \frac{1}{2} O_2 + H_2O + 2e^-$ (2.7)

Cell: $H_2O \rightarrow H_2 + \frac{1}{2} O_2$ (2.8)

Other investigations aim for reversible electrolysis of hydrobromic acid [8]. The electrical energy necessary to separate this molecule is half that required for a water molecule. An investigation getting special interest in the USA is the photoelectrochemical hydrogen production. This procedure is able to divide the water molecule into hydrogen and oxygen, using only solar light. Unlike the photovoltaic systems, these don't need wiring or external converters. The solar radiation harvesting system is able to generate enough voltage to separate the water.

In reactions similar to those used for separating hydrogen from fossil raw materials, the feedstock may be replaced by biomass, which is renewable. This is one of the most promising approaches. Advanced studies are based on biomass gasification combined with a shift reaction as shown in equation 2.3

Another method in the development is the use of certain type of algae and photosynthetic bacteria [9] that can produce hydrogen under certain conditions. The algae pigments absorb the energy of the sun and the cell's enzymes act like a catalysts to divide the water into hydrogen and oxygen.

2.2 Hydrogen storage

In order to use hydrogen as a general source of energy, hydrogen storage and transport should be economical and efficient. This supposes a considerable change compared to the transport and storage of conventional fossil fuels, due to its low density. At the present time, there are different ways (compressed gas, liquid form, chemically combined or adsorbed in porous solids) to store hydrogen, for both the stationary applications and the transportation sector. This depends on diverse factors like: (i) the way it is going to be used in its final stage, (ii) the energy density required, (iii) the amount of gas to be stored, (iv) the length of the storage time, (v) the existence of other possible sources of energy available, (vi) the costs, (vii) necessities of maintenance, (viii) installation and (ix) operation costs.

In the case of the use of hydrogen energy as fuel for transportation, one of the main problems to be solved is the lack of an adequate storage system in the vehicle, which can fulfill the safety requirements, costs, and the required provision characteristics. The Department of Energy of the United States has the objective to achieve a hydrogen storage weight efficiency (relative weights of stored hydrogen and the total storage system) of 6% and a volumetric hydrogen density of 60 kg·m^{-3} [10]

The hydrogen molecule H_2 can be found in various forms depending on the temperature and the pressure which are shown in the phase diagram (Figure 2.1)

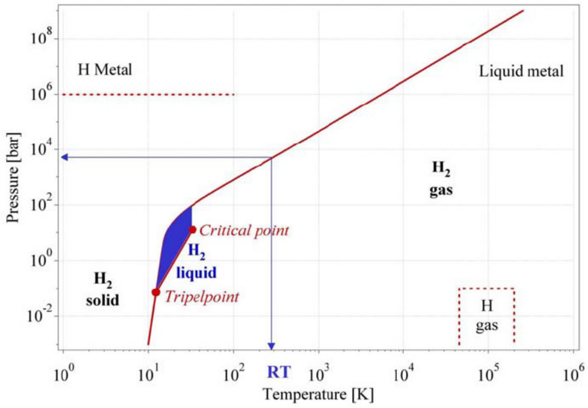

Figure 2.1 Primitive phase diagram for hydrogen [11]

At low temperature hydrogen is a solid (-262°C) with a density of 70.6 kg·m^{-3} and is a gas at higher temperatures (0°C) with a density of 0.089886 kg·m^{-3} and a pressure of 1 bar. A small zone between triple point and the critical point exhibits the liquid hydrogen with a density of 70.8 kg·m^{-3} at -253 °C [11]. At ambient temperature (298.15 K), hydrogen is a gas and can be described by the Van der Waals equation (2.9):

$$p = \frac{nRT}{V-nb} - a\left(\frac{n}{V}\right)^2 \tag{2.9}$$

Where p is the gas pressure, V the volume, T the absolute temperature, n the number of moles, R the gas constant ($R = 8.314\ m^3 \cdot Pa \cdot K^{-1} \cdot mol^{-1}$), a is the dipole interaction or repulsion constant ($a = 2.476 \cdot 10^{-2}\ m^6 \cdot Pa \cdot mol^{-2}$) and b is the volume occupied by the hydrogen molecules itself ($b = 2.661 \cdot 10^{-5}\ m^3 \cdot mol^{-1}$).

Storage basically implies to reduce the enormous volume of the hydrogen gas; it can be done compressing the hydrogen, decreasing the temperature below the critical temperature or reducing the repulsion interaction between hydrogen molecules. The reversibility of the hydrogen uptake and release excludes all covalent hydrocarbon compounds as hydrogen carriers because the hydrogen is only released from the compounds if being heated to temperatures above 800 °C [1]. The four principal methods of hydrogen storage are discussed below.

2.2.1 High pressure gas cylinders

Hydrogen is usually produced and used in gaseous form and could be stored in this state at high pressures. This type of storage (pressures over 20MPa) [12] requires thick walled heavy containers and generates security concerns on vehicles, at storage depots and in distribution systems.

The value of high gas densities at high pressures is degraded by the increment of the thickness and weight of the pressurized cylinder walls. Equation 2.10 related the wall thickness d_w, the outer diameter of the cylinder d_o, the overpressure Δp and the tensile strength of the material σ_v [1]:

$$\frac{d_w}{d_o} = \frac{\Delta p}{2 \cdot \sigma_v + \Delta p} \tag{2.10}$$

The principal materials used for build the gas cylinder are: austenitic stainless steel (e.g. AISI 316 and 304 and AISI 316L and 304L above 300°C to avoid carbon grain-boundary segregation), copper, aluminum core encased with fiberglass (composite) and plastic core encased with fiberglass (composite).

Figure 2.2 shows the volumetric density of hydrogen inside the cylinder and the ratio of the wall thickness over the outer diameter of the pressure cylinder made of stainless steel with a theoretical tensile strength of 460 MPa; versus the H_2 gas pressure.

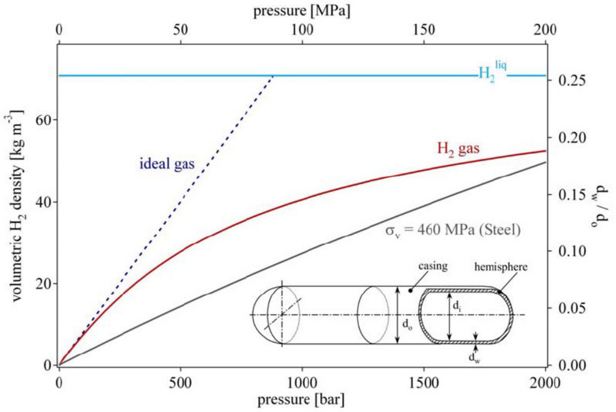

Figure 2.2 Volumetric density of H_2 and wall thickness ratio versus the H_2 pressure [1]

When comparing this alternative with the handling of other fuels, the storage of gaseous hydrogen at high pressures is not competitive due to its low density and to the high cost of the containers and the compression process of hydrogen. Problems also arise with heating of tanks on fast filling, which may limit the rate at which tanks can be refilled. Pre-cooling of the hydrogen or the use of heat exchangers may be required to overcome this barrier.

2.2.2 Liquid hydrogen

The possibility of storing the hydrogen in its liquid state in cryogenic containers requires very low temperatures of storage (21.2 K), making volatilization loss inevitable even when using the efficient techniques of isolation. In addition, the high consumption of power achieve the cooling (approximately 30% of the stored energy) causes this option to be economically nonviable, except in cases where the hydrogen cost is not a critical factor and the fuel is consumed in a short period of time after being stored (for example, in aerospace applications). The volumetric density of liquid hydrogen is 70.8 $kg \cdot m^{-3}$ and slightly higher than that of solid hydrogen (70.6 $kg \cdot m\text{-}^{3}$) [11].

The simplest liquefaction cycle is the Joule-Thompson cycle .The gas is first compressed, and then cooled in a heat exchanger, before it passes through a throttle valve where it undergoes an iso-enthalpic Joule-Thomson expansion, producing liquid. The cooled gas is separated from the liquid and returned to the compressor via the heat exchanger [1].

The free enthalpy change between gaseous hydrogen at 300K and liquid hydrogen at 20K is 11640 $kJ \cdot kg^{-1}$ [13]. The necessary theoretical energy (work) to liquefy hydrogen from RT is $W_{th} = 3.23$ kWh·kg^{-1}, the technical work is about 15.2 kWh·kg^{-1} (due to volatilization loss), almost half of the lower heating value of the hydrogen combustion (33.33 kWh·kg^{-1})

2.2.3 Physisorption of hydrogen

Recently, the possibility of carrying out the hydrogen storage by means of adsorption in a porous solid has been considered, which would present the advantage of being a safer form for hydrogen storage and simpler to handle, reducing the necessity of high pressures for its storage.

The adsorption of a gas on a surface is a consequence of the field force at the surface of the solid that is called the 'adsorbent', which attracts the molecules of the gas or vapor that is called 'adsorbate'. The mechanism for the adsorption of supercritical gases on any kind of adsorbents follows two basic rules: the monolayer adsorption mechanism, and the exponential decrease of adsorption with an increment in temperature. The adsorption capacity of hydrogen on a material depends on the specific surface area of the material and higher temperatures will lower the adsorption capacity [12]. The total storage capacity in a porous solid is, however, not only the adsorption capacity, but also the sum of contributions due to adsorption on solid surface and that due to compression in the void space.

In this sense, the first published works based on carbon nanostructures from Dillon et al. [14] showed exceptional capacity of storage of 5 to 10 mass% by weight. Since then and up until now, a concerted effort is being dedicated to the study of carbon nanostructures with high specific surface (fibers, nanotubes and activated carbons);

concluding that the amount of hydrogen adsorbed at a liquid nitrogen temperature (77 K) is proportional to specific surface BET of the carbon nanostructure, independently of the geometric structure of the carbon nanotubes.

Equation 2.11 estimates the quantity of absorbate in the monolayer surface of the solid:

$$S_{ml} = \frac{\sqrt{3}}{2} \cdot \left(\sqrt{2 \cdot N_A} \cdot \frac{M_{ads}}{\rho_{liq}} \right)^{\frac{2}{3}} \tag{2.11}$$

Where S_{ml} is the minimum surface area for one mol of adsorbate in a monolayer on a substrate, ρ_{liq} is the density of the liquid, M_{ads} is the molecular mass of the adsorbate and N_A is the Avogadro constant ($N_A = 6.022 \cdot 10^{23}$ mol^{-1}). For the case of carbon as the substrate and hydrogen as the adsorbate, the maximum specific surface area of carbon is $S_{spec} = 1315$ m$^2 \cdot$g^{-1} (single side graphene sheet) and the maximum amount of adsorbed hydrogen is M_{ads}= 3.0 mass% [1].

A possible way for enhancement of adsorption capacity is cryo-adsorption method. This technology is credible due to the cost of cool provided by liquid nitrogen is cheap, and the activated carbon can be used for long, and the boiling-off of hydrogen is replaced by the boiling-off of nitrogen.

2.2.4 Metal hydrides

Numerous transition metals, and their alloys, can be used to store hydrogen in form of metallic hydrides. These hydrides are formed by the reaction with hydrogen, being this one absorbed by the metallic structure, and being able to be absorbed due to small variations of pressure, occupying interstitial sites of the metal lattice. The basic reaction of the hydrogen absorption/desorption in a metal is given by the following equation:

$$M + 1/2\, H_2 \underset{}{\overset{T,\,P}{\rightleftarrows}} MH + \text{Energy} \tag{2.12}$$

Low temperatures drive this equation to the right and high temperatures drive it to the left. Some metal hydrides absorb and desorb hydrogen near ambient temperature and near atmospheric pressure, and the volumetric density of the hydrogen atoms present in the host lattice is extremely high. A volumetric density of 115 kg/m^3 was reached in $LaNi_5H_6$, which exceeds liquid or compressed gaseous hydrogen by far [1,15]. A comparison between metal hydrides and other different ways for storing hydrogen is shown in table 2.1. However, all the reversible hydrides working around ambient temperature and atmospheric pressure consist of transition metals; therefore, the gravimetric hydrogen density is limited to less than 3 wt%.

Table 2.1 Comparison among different ways of storing hydrogen [16]

Storage Method	ρm (mass %)	ρv (kg H_2 m^{-3})	T (K)	P (bar)	Phenomena and remarks
High pressure gas cylinders	13	< 40	303	800	Very high pressures, heavy systems, slow filling.
Liquid hydrogen in cryogenic tanks	Size dependent	70.8	21	1	Expensive, volatilization loss, high consumption of power
Adsorbed hydrogen (Carbon nanotube)	~2	20	193	100	large specific surface area, reversibility problems, low temperatures

Table 2.1 (Continued)

Absorbed on interstitial sites in a host metal (Metal hydrides)	~2	150	303	1	Fully reversible, Highest volumetric density, moderated temperatures and pressure
Complex compounds	<18	150	>373	1	Problems with reversibility

In contrast to the interstitial hydrides, hydrogen may be also bound ionically or covalently. Depending on the nature of the bonds, these materials are hence categorized as either "saline (salt-like)" (e.g. MgH_2, LiH) or as "complex" hydrides (e.g. $NaAlH_4$, $Zn(BH_4)_2$). Unlike the metallic hydrides, hydrogen is released via cascade decompositions from the complex hydrides, and the step reactions may occur for different conditions.

A deeper explanation of the metal hydrides properties such as thermodynamics, kinetics and isothermal pressure composition is given in the next chapter.

CHAPTER 3

METAL HYDRIDES

Hydrogen storage by metal hydrides comprises an intermetallic alloy phase that has the capability to absorb and hold vast amounts of hydrogen by chemical bonding [17]. An appropriate hydrogen storage matrix should have the capacity to absorb and release hydrogen without compromising the matrix structure. Metal hydrides are prepared by reaction between a metallic phase and hydrogen. When exposed to hydrogen at certain pressures and temperatures, these phases absorb large quantities of hydrogen gas and form the corresponding metal hydrides. If this is the scenario, the hydrogen is distributed compactly throughout the intermetallic lattice. Metal hydrides represent an exciting process of hydrogen storage which is inherently safer than the compressed gas or liquid hydrogen storage. Additionally, some intermetallics (including metals and alloys) store hydrogen at a higher volume density than liquid hydrogen.

The qualities required to make these intermetallics useful include the facility to absorb and release large amounts of hydrogen gas, many times without damaging the storage material and with good selectivity (only hydrogen absorption). Moreover, suitable metal hydrides absorb and release hydrogen at rates that can be controlled by adjusting temperature and/or pressure.

As mentioned in the second chapter, a typical relation of metal hydrides with hydrogen can be expressed as $M + \frac{x}{2} H_2 \longleftrightarrow MHx$ + Heat, where M represents the intermetallic matrix and H is hydrogen. The effect is reversible and the direction is determined by the pressure (and temperature) of the hydrogen gas. If the pressure is above a certain level (the equilibrium pressure), the effect proceeds to the right to form the hydride; whereas below the equilibrium pressure, hydrogen is liberated and the intermetallic matrix returns to its original state. The equilibrium pressure, itself, depends upon temperature. It increases due to expansion with an increment in temperature (and vice versa).

3.1 Classification of the hydrides

In general, hydrides are classified according to the nature of the bonding of hydrogen to the host lattice such as covalent, saline or ionic, and metallic, all of these classes bearing different bonding characteristics [18]. Such a classification doesn't always clarify the characteristic features of the compound in question. For example, lithium, hydride is classified as a saline hydride, where in reality it actually exhibits some covalent characteristics. The rare-earth hydrides are normally classified in the metallic hydride group, whereas they exhibit some characteristics similar to those of volatile and saline hydrides (e.g. high heat of formation).

3.1.1 Ionic hydrides

Ionic hydrides are created by reaction between a strongly electro-positive alkali (or alkaline-earth) metal and hydrogen, which becomes strongly electronegative because of the electron transfer. Contrary to the covalent hydrides, the bonding in the ionic hydrides results from the strong electrostatic forces between the dissimilar charges of the two different ions. The ionic hydrides are usually crystalline, show high heats of formation and high melting points. The ionic alkali and alkaline earth hydrides have a higher density than the pure alkali (45 to 75 %) and alkaline-earth metals (20 to 25 %) [19].

3.1.2 Covalent hydrides

Covalent hydrides are found in the solid, liquid or gaseous phases. The bonding between hydrogen and the other constituents is characterized by sharing of valence electrons on a relatively equal basis. In general, molecules with covalent bonding are not strongly attracted to each other. The lack of strong intermolecular forces yields a degree of volatility and a low melting point. Covalent hydrides are generally thermally unstable, and this instability goes up with increasing atomic weight of the non-hydrogen element(s). Typical covalent hydrides are carbon hydrides, boron hydrides, germanium hydrides, etc. Covalent hydrides normally exhibit low symmetric structures.

3.1.3 Metallic hydrides

Metallic hydrides are normally formed by the transition metals, for example ScH_2 [19]. They generally exhibit metallic characteristic properties such as high thermal and electrical conductivity, hardness, luster, etc. Due to the wide homogeneity ranges adopted by metallic hydrides, they have occasionally been considered as solid solutions of hydrogen in the interstitials of metal, alloy or intermetallic matrices.

3.2 Metal hydride formation

At a large distance from the metal surface the energy difference between a hydrogen molecule and two separate hydrogen atoms is the dissociation energy ($H_2 \rightarrow 2H$, $E_D = 435.99$ kJ·mol^{-1}). The first attractive interaction of the hydrogen molecule approaching the metal surface is the Van der Waals force leading to the physisorbed state ($E_{Phys} \approx 10$ kJ·mol^{-1}) more or less one hydrogen molecule radius (≈0.2 nm) from the metal surface. Closer to the surface the hydrogen has to overcome an activation barrier in order to dissociate and create the hydrogen metal bond. The height of the activation barrier depends on the surface elements involved. Hydrogen atoms sharing their electrons with the metal atoms at the surface are in the chemisorbed state ($E_{Chem} \approx 50$ kJ·mol^{-1}·H_2). The chemisorbed hydrogen atoms may have a high surface mobility, interact with each other and form surface phases at considerably high coverage. In the following step, the chemisorbed hydrogen atoms can jump into the subsurface layer and finally diffuse to interstitial sites through the host metal lattice. An interstitial hydrogen atom contributes its electron to the band structure of the metal; this process is depicted in Figure 3.1

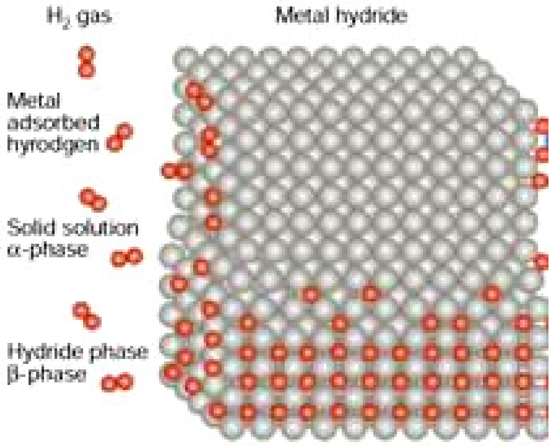

Figure 3.1 Schematic representation of the dissociation of hydrogen-gas molecule [2]

In the solid solution, α-phase, the hydrogen to metal ratio is small ($H/M < 0.1$) and hydrogen is exothermically dissolved in the metal. The metal lattice expands relative to the hydrogen concentration by approximately 2 to 3 $Å^3$ per hydrogen atom [20]. At greater hydrogen concentrations in the host metal ($H/M > 0.1$) a strong H-H interaction due to the lattice expansion becomes significant and the hydride phase (β-phase) nucleates and grows. The hydrogen concentration in the hydride phase is commonly found to be $H/M = 1$.

The volume expansion between the coexisting α- and the β-phase [21] corresponds in many cases 10 to 20% of the metal lattice. Therefore, at the phase boundary large stresses are created that frequently lead to a decrepitation of brittle host metals including intermetallic compounds resulting in a final hydride powder with a representative particle size of 10 to 100 μm.

3.3 Hydride properties

3.3.1 Pressure–composition–temperature (PCT)

An idealized representation of pressure- concentration- temperature isotherms for the α solid solution phase and β hydride phase is shown in Figure 3.2

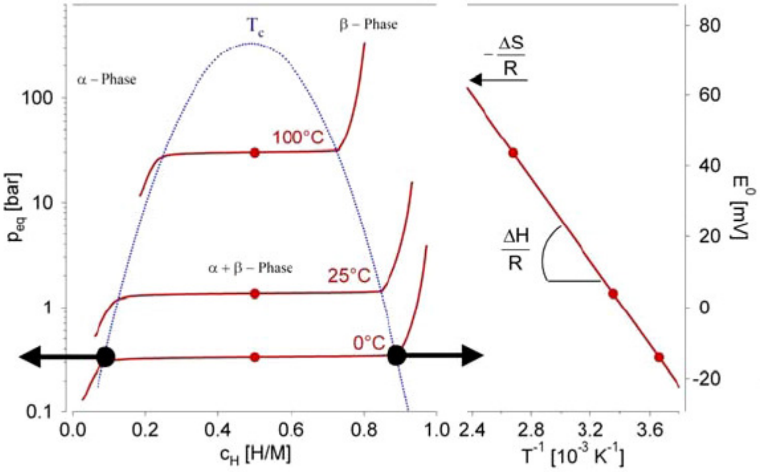

Figure 3.2 Effect of temperature on the general features of the P-C isotherms [2]

A plateau is observed on the pressure versus hydrogen/metal ratio for fixed temperature. When the reaction is complete, another sharp pressure rise is seen if more hydrogen is added. At a certain temperature, the plateau pressure reflects one point on a pressure-temperature (Van't Hoff) plot. The log of pressure versus reciprocal temperature is linear with a negative slope and is related to the heat of reaction (heat of hydriding); the plateau pressures must increase with temperature due to the linear relationship between pressure and temperature.

An increment in isothermal temperature causes the plateau pressure to increase and, at the same time, reduces the width of the plateau which represents the miscibility regime of the α- and β-phase. This narrowing process of the plateau with increasing of temperature continues until, eventually, at a certain ‘critical temperature’, T_c, the plateau disappears totally, reducing the miscibility of the two phases to zero, and the α- phase converts continuously into the β-phase. The slope and length of the equilibrium plateau is of particular importance for hydrogen storage application; a flat plateau enables the reversible absorption and desorption of hydrogen from a metal simply by raising or lowering the surrounding hydrogen pressure above or below the plateau pressure.

The equilibrium pressure as a function of temperature is related to the changes ΔH and ΔS of enthalpy and entropy, in that order, by the Van’t Hoff equation [22-24]:

$$\ln\left[p(H_2)/p^\circ\right] = \Delta H/RT - \Delta S/R \tag{3.1}$$

Where $p(H_2)$ is the hydrogen equilibrium pressure at α to β hydride phase conversion, determined from PCT isotherms; p^o is the standard pressure, R is the gas constant and T is the temperature. The enthalpy, ΔH of hydride formation is an important parameter characterizing the alloy as a proper hydrogen absorber for various applications. In general, the difference in standard entropy (ΔS) between a metal hydride alloy and its hydride is small and is on the order of 10 $J \cdot mol^{-1} \cdot K^{-1}$. The modification in entropy with hydride formation is mainly provided by the loss of the standard entropy of hydrogen gas (130.858 $J \cdot mol^{-1} \cdot K^{-1}$ at 298 K), which means that ΔS can be assumed to be a constant and does not depend on the nature of the metal hydride alloy [2]. The knowledge of ΔH particularly is significant to the heat management needed for practical engineering devices and is a fundamental measure of the M–H bond strength. The Van’t Hoff plot (lnP vs 1 /T) is a practical way to compare hydrides due to their thermal stabilities.

Most practical hydriding metals do not show perfectly flat plateaux or zero hysteresis [25] due to defects in the lattice or disorder in the atomic arrangement which creates slightly different potential for crystallographically identical interstitial sites and the irreversible elastic after-effects [26]. Figure 3.3 represents real metal hydrides PCT plot including the mathematical and numerical definitions of hysteresis, plateau slope and hydrogen storage capacity. In particular, there are a few ways to show the H-capacity. The reversible capacity, $\Delta(H/M)_r$, is defined as the plateau width, which can be considerably less than the maximum capacity, $(H/M)_{max}$. In practice, depending on available pressure and temperature ranges, engineering capacity is frequently somewhere between $\Delta(H/M)_r$ and $(H/M)_{max}$

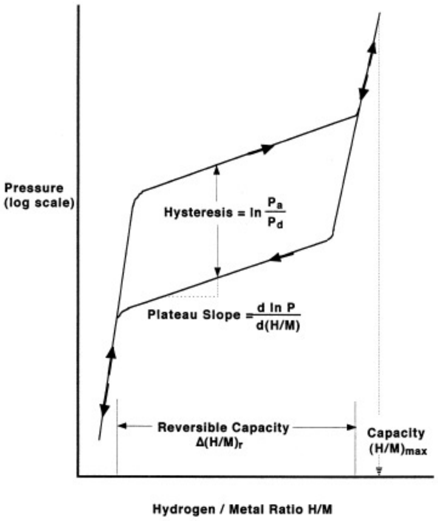

Figure 3.3 Sloping plateau and hysteresis effect in a real metal hydride [20]

Hydrogen storage capacity can be shown in either atomic H/M ratio or weight percent. In calculating wt%, both H and M (not only M) are included in the denominator.

Adding up, it is sometimes useful to express capacity in volumetric terms, e.g., number of H atoms per unit volume.

3.3.2 Activation

The process needed to hydride a metal the first time and bring it up to maximum H-capacity and hydriding/dehydriding kinetics is called activation. The ease of initial H_2-penetration depends on surface structures and barriers, such as dissociation, catalytic species and oxide layers. A second stage of activation involves internal cracking of metal particles to amplify reaction surface area.

3.3.3 Decrepitation

This process is the self-pulverization of large metal particles into powder, a common phenomenon that comes about from a combination of a change in the hydriding volume and the brittle characteristic of hydriding alloys (especially when they contain some H in solution) [27]. The morphology of the decrepitated powder affects heat transfer as well as the tendency of powder migration into undesirable places like valve seats. A bad factor is that most hydride powders have poor heat transfer coefficients and require engineering means for thermal enhancement for example Al foam, internal fins, etc. The morphology of the powder can have an effect on packing, which in turn can lead to internal gas impedance and container deformation.

3.3.4 Kinetics of hydriding and dehydriding

In order to keep the weight and volume of hydride small, it is very important to maintain short cycle times for loading and unloading hydrogen. Heat transfer has been shown to be the rate limiting process controlling hydrogen uptake or removal. This is the result of the low-conductivity of the finely divided powder and poor heat transfer between the particles and the container wall [27]. Hydrogen flow is not rapid enough to decrease these heat transfer resistances. Supper and coworkers [28] showed that it is just as important to improve both the heat transfer and the hydrogen flow to achieve high gas transfer.

The most common method to evaluate the kinetics of a material is simply to measure the concentration of hydrogen absorbed or desorbed versus time, but there are some factors that could effect this measurement, such as quantity of sample, sample shape, porosity, thermal (bulk and grain-to-grain) conductivity, thermal contact with the sample holder, size distributions of particles, particle shape, applied hydrogen over-pressure and the purity of the gas.

3.3.5 Gaseous impurity resistance

There can be several types of damage and degradation of performance due to the alloy–impurity concentrations [29]: (1) poisoning, where capacity is rapidly lost without a concurrent decrease of initial kinetics; (2) retardation, where kinetics are quickly lost without loss of ultimate capacity; (3) reaction, where the alloy is slowly corroded; (4) innocuous, where there is no surface damage but there can be pseudo-kinetic decreases due to inert gas blanketing, an interparticle gas diffusion problem. Damages from poisoning and retardation are for the most part recoverable in contrast to reaction damages that are usually unrecoverable.

3.3.6 Cyclic stability

This property is referred to the repeatability of the hydride/dehydride process and widely varies for different alloys or compounds [30]. Alloys and intermetallic compounds are normally metastable relative to disproportionation, the tendency to break up metallurgically to form stable, not easily reversible hydrides. Even if very pure H_2 is used, disproportion can occur with a resultant loss of reversible capacity.

3.3.7 Safety

Safety usually centers on pyrophoricity, the tendency for a hydride powder to burn when suddenly exposed to air, such as an accidental tank rupture. But the term can also include toxicity that results from accidental ingestion or inhalation.

3.3.8 Alloy cost

The alloys cost has been influenced by several factors, which include raw materials cost, melting and annealing costs, metallurgical complexities, profit and the degree of PCT precision required for the specific application.

3.4 Metal hydride families

Hydrogen is a highly reactive element and has been found to form hydrides and solid solutions with thousands of metals and alloys [20]. A hydride 'family tree' of the elements, alloys and complexes is shown in Figure 3.4

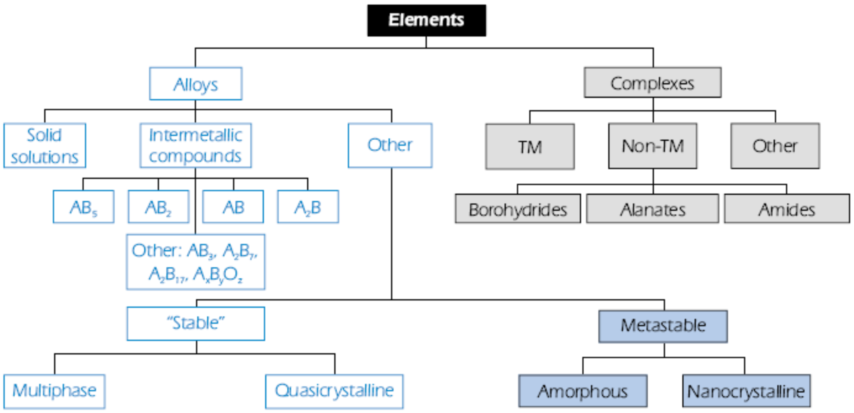

Figure 3.4 Family tree of the elements, alloys and complexes [20]

3.4.1 Elements

The majority of the 91 natural elements below hydrogen in the periodic table will form hydrides under appropriate conditions such as: VH_2, NaH, LaH_2, ZrH_2, etc. Unfortunately the PCT properties are not very suitable for the 1–10 atm, 0–100°C range used for practical hydrogen storage. Only vanadium is in the range and there has been extensive study of solid solutions of V and other metals. Pd has been used for over 100 years for H-storage, but it is very costly, it doesn't hold much H and it requires heating temperatures above 100°C to release atomic hydrogen.

3.4.2 Alloys

To prepare useful reversible hydrides, strong hydride forming elements A are combined with weak hydriding elements B to form alloys (especially intermetallic compounds) that have the desired intermediate thermodynamic affinities for hydrogen. A good example of this characteristic is the combination of La (forming LaH_2 with 25 °C, $P_d = 3x10^{-29}$ atm and $\Delta H_f = -208$ kJmol^{-1} H_2) with Ni (NiH, 25 °C, $P_d = 3400$ atm, $\Delta H_f = -8.8$ kJmol$^{-1}H_2$) to form the intermetallic compound $LaNi_5$ ($LaNi_5H_6$, 25°C, $P_d = 1.6$ atm, $\Delta H_f = -30.9$ kJmol$^{-1}H_2$). This ability to 'interpolate' between the extremes of elemental hydriding behavior opened the door to the modern world of reversible hydrides.

3.4.2.1 AB_5 intermetallic compounds

The AB_5 family has an exceptional versatility because many different elemental species can be substituted (at least partially) into the A and B lattice sites. A-elements tend to be one or more of the lanthanides (elements 57–71), Ca or other elements such as Y, Zr, etc. The B-elements are based on Ni with many other possible substitutional elements such as Co, Al, Mn, Fe, Cu, Sn, Si, Ti, etc. Modern commercial AB_5 hydriding alloys are for the most part based on the use of the lanthanide mixture or mischmetal (Mm=Ce+La+Nd+Pr) for the A site and Ni+Al+Mn+Co+… on the B-site.

Hydrogen storage-capacity is on the uncomfortably low side, not passing 1.3 wt. % on the plateau basis. Alloy raw material cost is high, at least by comparison to other systems (AB_2 and AB) that are discussed below, the AB_5 alloys are easy to activate, hardly requiring any heating. They decrepitate on the 1st H/D cycle to fine powder which is mildly pyrophoric if suddenly exposed to air, a well-known property that must be included in safety considerations. Both easy activation and pyrophoricity indicate the AB_5 alloys do not form defensive oxide layers. Intrinsic kinetics of the AB_5 alloys are generally very good.

3.4.2.2 AB_2 intermetallic compounds

Like the AB_5 compounds, the AB_2 intermetallics represent a large and versatile group of hydriding materials with good PCT properties at ambient temperature. The A-elements are often from the IVA group (Ti, Zr, Hf) and/or rare earth series (n_o. 57–71). The B- elements can be a variety of transition or non-transition metals with somewhat of a preference for atomic numbers 23–26 (V, Cr, Mn, Fe). A large variety of substitutions are possible for both A- and B- elements, thus providing a high degree of fine tuning of PCT properties.

The decisive advantages in regard to hydrogen storage and related thermal applications are, high hydrogen capacity, ease of activation, very rapid rates of absorption and desorption, long cycling life, and low cost of materials. The main disadvantages for hydrogen storage are high ΔH values (moderate stabilities of hydrides). These properties make these compounds good for hydrogen compression applications. An excellent example is ZrMn2 that contents 3.6 atoms of hydrogen and ΔH=-53.0 kJ/molH_2, showing a high hydrogen content and a high T_{dec}, related to the high ΔH [31]. The high T_{dec} and the high hydrogen content makes this compound good for hydrogen compression.

3.4.2.3 AB intermetallic compounds

The first example of a reversible intermetallic hydride was demonstrated with the AB compound, ZrNi by Libowitz in 1957 [32]. The hydride $ZrNiH_3$ has a 1 atm desorption temperature of about 300°C, too high for hydrogen storage applications but suitable for hydrogen compression. The properties are investigated in the results chapter.

These intermetallic alloys show good volumetric and gravimetric reversible H-capacities, competitive with the best of the AB_5's and AB_2's. Activation is pretty slow and hard for the ZrNi-based alloys. In any event, it may take a day or so and high pressures (50+ atm) for total activation. The passive oxide films that can form on ZrNi (and its derivatives) don't result in a high degree of sensitivity to gaseous impurities in the H_2, used; hence these alloys are resistant to impurities. Cyclic stability of the lower plateau is great, but the upper plateau tends to drift higher with H/D cycling.

3.4.2.4 A_2B intermetallic compounds

A is typically of the Group IVA elements Ti, Zr or Hf and B is a transition metal, typically Ni. Another family is based on Mg_2Ni [33]. Unfortunately, the A_2B's offer little in the 0–100 °C, 1–10 atm range, at least with the present state of the art. They are definitely more stable. H-capacity and cost properties of Mg_2Ni are attractive, but desorption temperatures are too elevated for most applications. Mg_2Ni is not very amenable to modification of PCT properties by ternary and higher-order substitutions. Various attempts to lower desorption temperatures have not been especially successful.

3.4.2.4 Other intermetallic compounds

In addition to the AB_5, AB_2, AB and A_2B intermetallic compounds discussed above, various other families of intermetallics have been shown capable of reversible hydriding/dehydriding reactions [34,35]. Examples include AB_3, A_2B_7, A_6B_{23}, A_2B_{17}, A_3B and others. Most structures involve long-period AB_5 and AB_2 stacking sequences and are thus crystallographically related to these two classic families. Most have narrow plateaux with long sloping upper legs (e.g., $GdFe_3$) or multiple plateaux (e.g., $NdCo_3$ or Pr_2Ni_7).

3.4.3 Complex hydrides

The group one, two and three light elements, e.g. Li, Mg, B, Al, can form a large variety of metal-hydrogen complexes. They are very interesting due to their light weight and the number (often 2) of hydrogen atoms per metal atom. The principal distinction between the complex hydrides and the previously described metallic hydrides is the transition to an ionic or covalent compound of the metals upon hydrogen absorption.

The hydrogen in the multifaceted hydrides is often located in the corners of a tetrahedron with boron or aluminum in the center. The negative charge of the anion, $[BH_4]^-$ and $[AlH_4]^-$ is compensated by a cation e.g. Li^+ or Na^+ [36].

There have been reports that there are about 70 known complex hydrides; some of those, such as $BaReH_9$ with 2.7 wt% of hydrogen, [37] have been reported to dehydride below 100 °C, but the low hydrogen content renders them ineffective as storage materials. The one family of complex hydrides that contains as much hydrogen as the aluminum hydrides is the borohydrides. The borohydrides vary greatly in hydrogen content, up to a maximum of 20.8 wt% for $Be(BH_4)_2$. This compound is normally not considered because of the toxicity of beryllium [37], however, there are numerous other known borohydrides. These hydrides release hydrogen slowly. Unlike the metallic hydrides, hydrogen is released via cascade decompositions in complex hydrides, and the step reactions call for different circumstances. Therefore, there is a big difference between the theoretical and the practically attainable hydrogen capacities. An example of the decomposition of a borohydride ($Zn(BH_4)_2$) is given by equation 3.2 [38]

$$Zn(BH_4)_2 \longrightarrow Zn + 2B + 4H_2 \tag{3.2}$$

Which shows $Zn(BH_4)_2$ thermally decomposing into the constituent elements with release of hydrogen. The main reason that complex hydride compounds have not been considered for hydrogen storage before is their reported lack of reversibility [38]. Recent reports of the catalysts that assist in the hydrogenation/dehydrogenation of complex hydrides of aluminum suggest the examination of other complex hydrides, especially borohydrides [39].

Some researchers have thought of complex hydrides as a promising solution to the hydrogen storage problem, maybe because this group of compounds has not been well studied with respect to behavior as a hydrogen carrier [40].

As a summary, in Figure 3.5 is shown various compounds of different groups (AB, AB_5, AB_2 and complex hydrides), comparing their volumetric hydrogen density and their gravimetric hydrogen density.

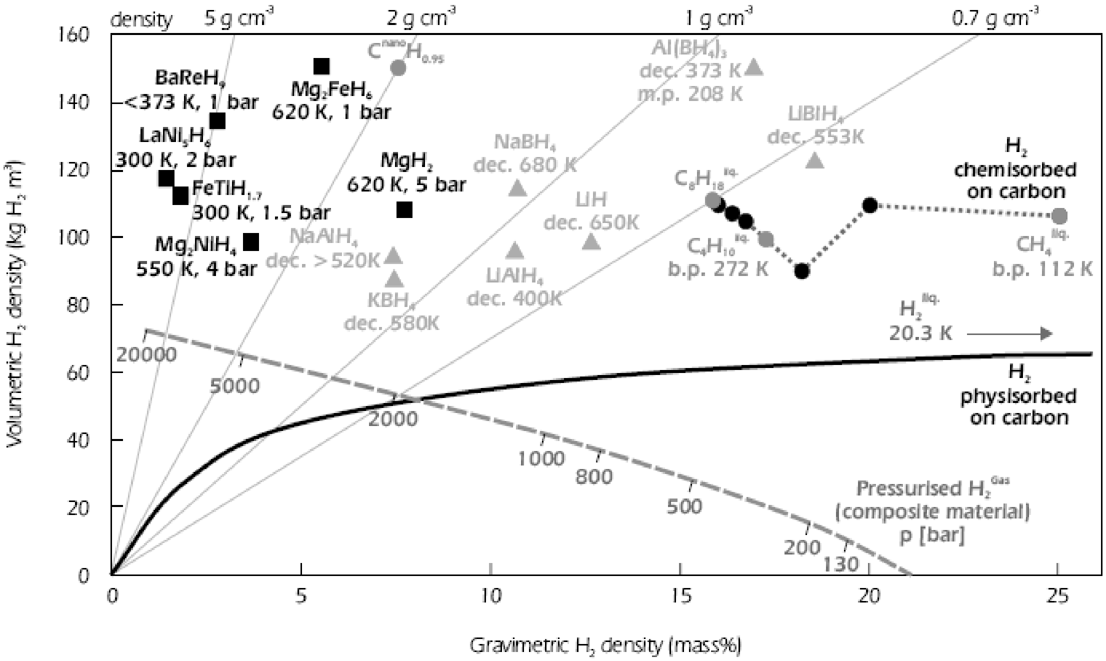

Figure 3.5 Volumetric and gravimetric densities for various H_2 storage forms [41]

3.5 Methods to improve kinetics

The kinetic behavior of a material is controlled by mechanisms which are determined by specific material properties; therefore, it should be possible to improve kinetics by altering these material properties [42].

3.5.1 Presence of other elements (catalytic effect)

Introducing other element(s) may alter the surface and the bulk properties of the metal hydride providing active sites for dissociation and may also create diffusion paths into the bulk. Many diverse elements have been investigated as possible catalysts to accelerate adsorption and desorption of hydrogen [43]. These include predominantly titanium, zirconium and iron. However, despite intensive search, titanium based materials still appear to have both the most favorable kinetics and also the highest reversible storage capacities. One should keep in mind, though, that both the actual catalyst precursor and the method of doping deeply influence the performance of the resulting materials.

The dotted red curve in Figure 3.6 shows the desired reaction path of thermal decomposition of a hydride material, which can be obtained by use of a suitably tailored catalyst. The storage material of choice is (thermodynamically) moderately stable; the barriers for both decomposition and hydrogen absorption are relatively small, with low $T_{dec.}$

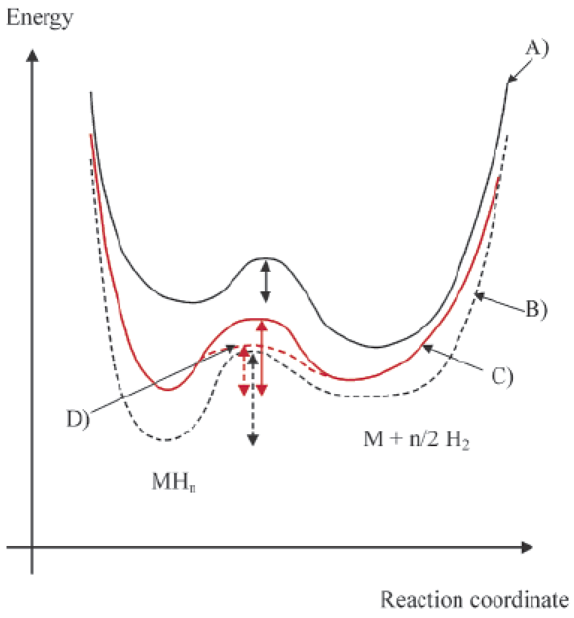

Figure 3.6 Reaction path for hydrogen evolving from different metal hydrides [43]

In the above figure, the curve shows the metal hydride: (A) Thermodynamically very unstable with low activation barrier and low T_{dec} and stores hydrogen irreversibly, (B) Thermodynamically very stable with high activation barrier and high T_{dec} and stores hydrogen reversibly, (C) Thermodynamically slightly stable with intermediate T_{dec} and stores hydrogen irreversibly, (D) Target situation: catalytically enhanced thermodynamically slightly stable with low T_{dec} and stores hydrogen reversibly; vertical arrows represent the activation barrier for the decomposition process.

3.5.2 Intimate contact (mechanochemical synthesis)

Intimate contact between two different phases may improve kinetics by enhanced diffusion through inter-phase grain boundaries [44,45]. This can be produced by mechanically milling a mixture of phases together. Significant progress has recently been reported in the mechanochemical synthesis of Zinc borohydrides [46]. Apparently careful ball milling of Sodium borohydride and Zinc Chloride helps to improve the stability and the T_{dec} of the hydrogen desorption process of the material for hydrogen storage applications based on the formation of a material with a formal composition of $Zn(BH_4)_2$ [47]. This simple and inexpensive method appears to be especially powerful because the thermodynamic stability of Zinc borohydride is decreased as compared to that of Sodium borohydride. It might be applicable for other metal hydrides. Ball-milling is also successful for other families of compounds. When coupled with catalysis, it has been shown to noticeably improve the reversibility of hydrogen storage of $NaAlH_4$ and some borohydride compounds. It’s believed that high-energy ball-milling might become a necessary (pre)treatment for a successful solid hydrogen storage material. Furthermore, the economic facet of ball-milling is also favorable: this process ranks among the most cost effective methods for materials’ homogenization and for the deliberate introduction of modified nanostructured surfaces.

An improvement in the contact between catalyst and metal hydride in the solid phase proves to be among the most decisive factors for achieving fast kinetics of hydrogen transformations.

3.5.3 Crack formation

Kinetics may be enhanced by crack formation due to lattice expansion during hydriding. These cracks bring clean metal surfaces into contact with hydrogen. The oxygen-free surface may promote the hydrogen dissociation reaction and diffusion into the bulk.

3.5.4 Increment in the surface-to-bulk ratio of the material

The overall kinetics may be increased by increasing the specific surface area. One way to do that is simply to reduce the average particle size or depositing the material as thin coating on another (hopefully catalytic) substrate; this will decrease the diffusion barrier created by the initial hydride layer formed at the surface of a particle.

3.6 Hydride applications

3.6.1 H-storage

Stationary storage usually involves storage of enormous amounts of hydrogen that requires big quantities of hydride alloy, making the alloy cost an important property. On the other hand, vehicular storage usually requires high hydrogen weight percent [48]; most existing hydrides fall short of what is desired in this property. Easy activation to minimize container pressure and temperature requirements for the one-time activation is important this application. In both cases, appropriate resistance to gaseous impurities is desirable in case impure H_2 is used or the inevitable unintentional introduction of air occurs. In both cases, PCT properties should be roughly in the ambient temperature and pressure so that waste heat from the environment or vehicle engine (or fuel cell) can be used for endothermic H_2 desorption.

3.6.2 Compression

The compression of gaseous H_2 using thermal swings of hydride beds is an open-ended process and generally requires the alloy to have good impurity resistance (impure H_2 pumped) and cyclic stability (high temperatures involved). H/D cycling is relatively fast, so good kinetics and heat transfer are needed [50,51]. If rapid cycling can be reached, then relatively small inventories of alloy are needed and alloy cost becomes secondary to other properties. Good H-capacity is needed so that parasitic heat losses associated with thermal swings are at their lowest. PCT properties must be adjustable to the input and output pressures desired and the input and heat sink temperatures available.

The basic elements of the simplest single-stage hydride hydrogen compressor and the cyclic mode of operation (PC isotherms and van’t Hoff plots) are shown in Figure 3.7

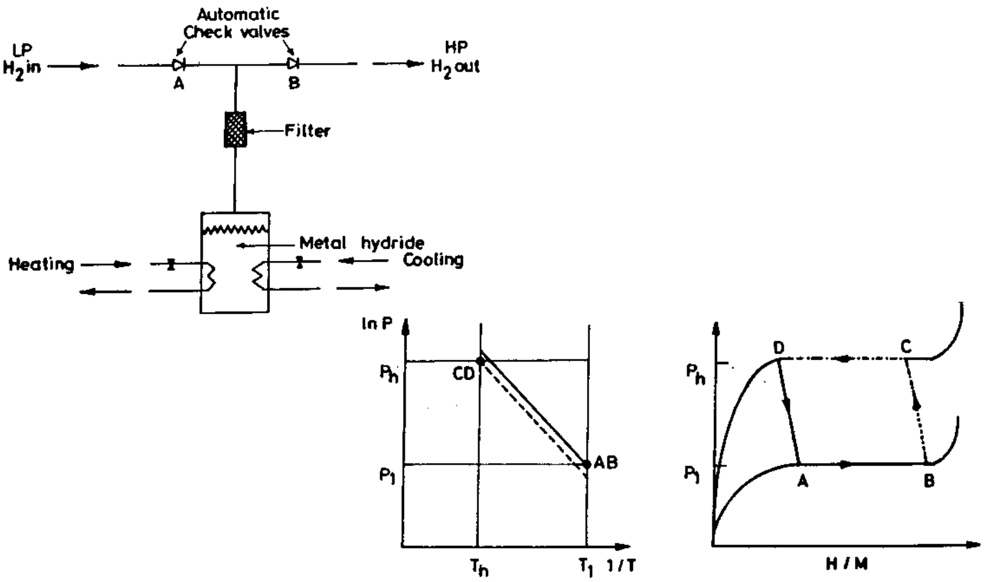

Figure 3.7 Elements and principle of operation of a hydride hydrogen compressor [26]

First, the metal alloy, M, is saturated with hydrogen isothermally at temperature T_l. The H-content increases at pressure P_l along the line AB on the T_l isotherm. The hydrogen is admitted through the inlet valve A. Next, the temperature of the hydride material (MH_x) is sharply raised from T_l to T_h by switching from the cooling to the heating fluid. This causes the pressure of the hydrogen to jump to P_h; the equilibrium (dissociation) pressure at T_h. This pressure rise is indicated by the dotted line BC. The increased pressure of the gas forces the inlet valve A to close, while the outlet valve B opens out automatically to discharge the gas (by desorption along CD on the T_h isotherm) into the external receiver. The pressure of hydrogen is thus raised from P_l to P_h simply by raising the temperature of the hydride from T_l to T_h. After the hydride has been depleted of hydrogen (point D), the system is cooled down to T_l by switching back to cooling water circulation, and the pressure returns to the initial value, P_l (point A). Then the cycle ABCD is repeated.

3.6.3 Closed thermodynamic systems

This class of hydride applications includes the following: (1) heat engines, where heat is turned into to mechanical energy in an expansion engine; (2) heat storage, for example solar heat; (3) heat pumps, where low-temperature heat is ‘upgraded’ to higher temperature; and (4) refrigerators, where heat is converted to refrigeration. Most are expected to cycle rapidly and involve considerably high temperatures, so good kinetics and cyclic stability is important. Like compressors, good capacity is desirable and PCT must be carefully adjusted to the application.

3.6.4 Separation

Separation can be divided into two types [20]: (1) H_2 separation from other gases; and (2) H-isotope separation. The first type can be further divided into gross separation, purification and gettering. All three subtypes depend on impurity tolerance, tailored PCT properties and other properties that are of specific application. For the case of getters, to remove trace amounts of H_2 from vacuum systems or other gases, very low room-temperature plateau pressures are required. H-isotope separation requires special properties involved with kinetic and PCT property differences among protium, deuterium and tritium.

CHAPTER 4

EXPERIMENTAL APPROACH

4.1 Experimental details

The manufacturers, descriptions and purities of the starting materials are shown in table 4.1

Table 4.1 Starting material references

Material	Purity	Description	Manufacturer
Zr	99.99%	Powder, 3um	Sigma-Aldrich
Mn	99+%	Powder, 325 mesh	Sigma-Aldrich
ZrNi 30/70 (weight)	99.99%	Powder, 325 mesh	Sigma-Aldrich
ZrNi 70/30 (weight)	99.99%	Powder, 325 mesh	Sigma-Aldrich
NaBH4	98%	10-40 mesh	Sigma-Aldrich
ZnCl2	99.999%	Reagent grade	Sigma-Aldrich
TiCl3	99.999%	ReagentPlus powder	Sigma-Aldrich
TiF3	99.999%	Powder	Sigma-Aldrich
Ni	99.99%	Nano powder, 10nm	QuantumSphere
Ni	99.9%	Nano powder, 90nm	Sigma-Aldrich
Ti	99.98%	Powder, 325 mesh	Sigma-Aldrich

Table 4.1 (Continued)

Ti	98.5%	Nano powder, 100nm	Sigma-Aldrich
Zn	99+%	Nano powder, 35nm	Sigma-Aldrich
Fe	99.5%	Nano powder, 100nm	Sigma-Aldrich
MgH2	98%	Powder	Alfa Aesar

The initial materials were used without pretreatment or further purification, with the exception of Zr, nano Fe and nano Ti. Since these powders are immersed in oil, an extraction procedure using Hexane solvent have been carried out in the glove box in order to separate the oil from the powder, and a vacuum process was followed to dry the powder.

All sample handling was carried out in a glove box under a nitrogen filled atmosphere to reduce the oxygen and moisture level down to <1 ppm. The mixtures in the present investigation were mechanically milled in a high energy Fritsch pulverisette planetary mono mill P6 using a stainless steel balls and bowl (80 ml) sealed with a viton O-ring. The ball to powder weight ratio and milling speed are optimized to 20:1 and 300 rpm respectively. Milling duration has been varied as 20 min., 12h, and 48h, depending on the sample; for $ZrMn_2$ synthesis, a mixture of Zr and Mn in a molar ratio 1:2 was used, the milling time was 48 hours with hydrogen flushing/purging every 4 hours in order to avoid air inside the bowl; a similar process was carried out for ZrNi synthesis. The starting materials ZrNi 70/30 ($Zr_{1.5}Ni$) and ZrNi 30/70 ($ZrNi_{3.63}$) were ball milled in a 5.26:1 molar ratio for 12 hours with hydrogen purging every 4 hours. For the $Zn(BH_4)_2$ preparation, a milling time of 20 minutes was standardized and applied, using a molar ratio of the initial compounds $NaBH_4$ and $ZnCl_2$ of 2 to 1; the same procedure has been followed for synthesizing doped complex hydrides. After ball milling, the as-synthesized compounds were transferred from the milling bowl into respective sample holders in the glove box for further characterization measurements.

In the heat flow and weight loss analysis, samples were loaded in aluminum and alumina pans respectively in the nitrogen gas filled glove box. The measurements have been performed using a DSC Q10 (aluminum pan) and a SDT Q600 (alumina pan) model from TA Instruments. The thermal measurements were analyzed using a Universal Analysis software tool.

X-ray diffraction (XRD) patterns were collected on a Philips X'pert diffractometer with CuKα radiation of $\lambda = 5.4060$ Å. The incident and diffraction slit width used for the measurements are 1° and 2° respectively. The collimating mask of 10 mm was used throughout the analysis, Phase identification and particle size calculation has been carried out using PANalytical X'pert Highscore software, version 1.0e. The samples were protected from air and moisture by wrapping it with thin foil, which shows diffraction peaks in the 2θ range of 21–28°.

The B-H bond stretch of the $NaBH_4$ and the undoped and doped $Zn(BH_4)_2$ samples were compared via a Perkin-Elmer One FTIR spectrometer.

The isothermal volumetric sorption measurements have been carried out by Hy-Energy's PCT equipment. The volume calibration without and with sample were performed at a constant temperature with accuracy of ±1° C. The dehydrogenation and rehydrogenation parameters such as pressure and temperature have been optimized for the efficient hydrogen storage characteristics. During sorption the sample temperature and applied pressure were monitored and recorded by a Lab View software program. The analysis of the measurements such as full absorption/desorption kinetics, cycle life and PCT were calculated using Hy-Analysis macros in the Igor program.

The microstructures of the samples in the different stages were observed by Hitachi S800 scanning electron microscope (SEM) and local phase composition was determined in the energy dispersive X-ray spectrometry (EDS) mode using the same instrument. A fixed working distance of 5mm and a voltage of 20KV were used. Genesis software was used to analyze the SEM images and EDS mappings.

Temperature programmed desorption (TPD) technique was carried out by Quantachrome Instruments Autosorb-1 equipment. The carrier gas used for the TPD and TPR measurement were nitrogen and argon(95%):hydrogen(5%) pre-mixed gases respectively. The thermal desorption/reduction profiles were recorded and analyzed using TPRWIN software package.

The thermal decomposition behaviors of the samples were examined by a GC/MS triple quadrupole (320-MS GC/MS) upon heating up to 150 °C with a heating rate of 5 °C /min under a helium flow.

4.2 Synthesizing methods and equipments

4.2.1 High energy ball mill (BM)

The objectives of the ball milling process include particle size reduction, mixing or blending, and particle shape changes. The most common mill used for these purposes has been a planetary ball mill; a bowl sits on a grinding platform and rotates in a direction opposite to the direction of the base fixture. This action is a lot like the "teacup and saucer" rides commonly found in amusement parks. In planetary action, centrifugal forces alternately add and subtract. The grinding balls roll halfway around the bowls and then are thrown across the bowls, impacting on the opposite walls at high speed. Grinding is further intensified by interaction of the balls and sample. Planetary action gives up to 10 g acceleration. The schematic cross-section diagram of the planetary ball mill principle is illustrated in Figure 4.1.

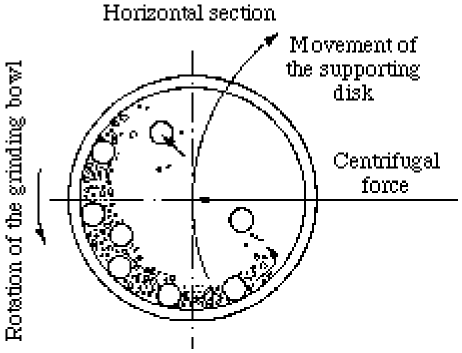

Figure 4.1 Schematic cross-section of a planetary ball mill [52]

In the planetary mono mill pulverisette 6, grinding bowls rotate around their own axes while also orbiting around a central axis reaching a speed up to 650 rpm [53]. As a result, forces are exerted on the grinding balls and the material which are constantly changing direction and amount. Optimum grinding ball movements are obtained due to design of geometry and transmission ratios.

The high-energy ball-milling process is becoming a necessary (pre)treatment tool for a successful solid state preparation of hydrogen storage materials. An increase in the active nanostructured surface of the crystallites, and an improvement in the contact between catalyst and hydrogen storage materials in the solid phase stand out among the most important factors for achieving fast kinetics of hydrogen transformations [54]. Another important factor in the success of this instrument is its economy; it is an inexpensive and rapid process when compared with other synthesizing methods such induction melting, quenching, sintering, etc.

4.2.2 Nitrogen filled glove box (dry box)

All the metal/complex hydride samples and the sample holder preparation for the analytical tools were carried out in a nitrogen atmosphere glove box manufactured by Innovative Technology Inc, USA. The oxygen and moisture level inside the box are controlled and lowered to the order of <1 ppm by continuously purging with nitrogen gas.

A glove box is a sealed container that is designed to allow workers to manipulate objects that are in an inert atmosphere. Built into the sides of the glove box are two gloves with which workers can perform tasks inside the box without breaking the seal or allowing potential damage to the worker's hands.

The principal components of the glove box used are: (i) gloves that are usually sized large (8 inches) so that anyone can get their hands in, (ii) vacuum pump, (iii) electronic sensors, that monitor oxygen and water content, (iv) two chambers, called the antechambers or ports that are used for insertion or removal of objects that are handled in the glove box. Each antechamber has two doors, one that can be opened only from the inside of the box and one that can be opened only from the outside. The antechamber can be evacuated with a pump or filled with nitrogen gas; (v) the gauge controls, they control the upper and lower pressure limits inside the glove box, if the pressure in the box gets too high, the controller automatically opens a valve to the vacuum pump to relieve the excess pressure and prevent the gloves from blowing off, likewise, if the pressure is too low, the controller fills the box with nitrogen; (vi) the pedatrol, it is a foot pedal that allows workers to manually adjust the pressure inside the glove box and finally (vii) the purification system with automatic valves that maintains the inside atmosphere less than 1 ppm level of O_2 and H_2O respectively [55]. The incoming purging nitrogen gas passes through a molecular sieve which continuously absorbs the contaminants to keep the glove box dry. The schematic diagram of the system one glove box is shown in Figure 4.2

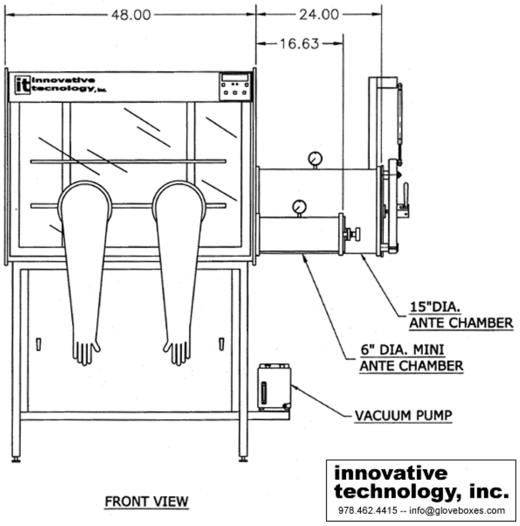

Figure 4.2 Schematic diagram of system one glove box [55]

4.2.3 Solvent purification system

The principal objective of the solvent purification system is to remove water and oxygen in order to produce dry, deoxygenated and high-purity solvents on demand. Solvents like pentane, hexane, isopropanol, tetrahydrofuran (THF), ether and toluene are purified in “Pure Solv 400-5-MD” equipment, manufactured by Innovative Technology Inc, USA; in this system a purification grade solvent is pushed from its storage container under low nitrogen pressure through two stainless steel columns containing activated alumina and copper. Trace amounts of water and oxygen are removed producing dry, deoxygenated solvent. The processed solvent is drained into in a storage flask where it can be dispensed, under nitrogen, using standard syringe techniques.

4.2.4 Annealing (tube furnace) system

After the ball milling process, some compounds such as ZrNi and $ZrMn_2$ lose their crystallinity due to the high energy ball collisions against the sample powder. With a proper heating process, the crystal structure of these compounds can be recovered. Figure 4.3 shows the schematic diagram and the real annealing system used. The main component of this heating system is the tube furnace, manufactured by Thermolyne, it can reach temperatures in the range of 100 and 1200 °C.

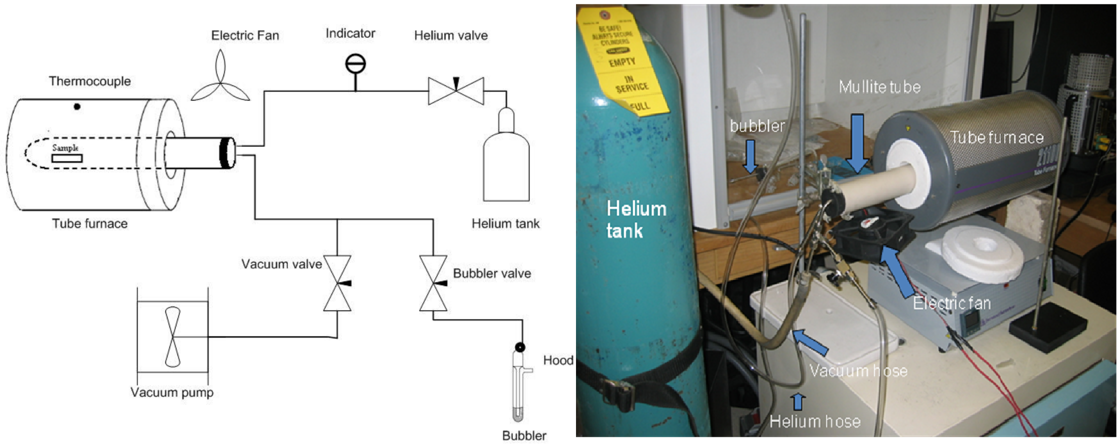

Figure 4.3 Schematic diagram and real look of the annealing arrangement

The operation of the annealing system above is as follows: the sample is pelletized in a press at 10000 tons and loaded in a ceramic boat (figure 4.4) inside the glove box to prevent oxidation. The boat is introduced in a mullite tube which has a melting point of 1680 °C. After inserting the mullite tube with the sample in the tube furnace a vacuum/helium purge cycle is done in three alternative cycles, to avoid oxygen/moisture inside the tube and in the lines. This cycling process is manually operated, first the helium and bubbler valves remain closed and the vacuum valve is opened. After 15 minutes of evacuation, the vacuum valve is closed and the helium valve is opened, when the indicator shows no negative pressure, the bubbler valve is opened; the helium flush is continued for 15 minutes. Finally after that the two valves are turned to close position and the vacuum valve is opened again.

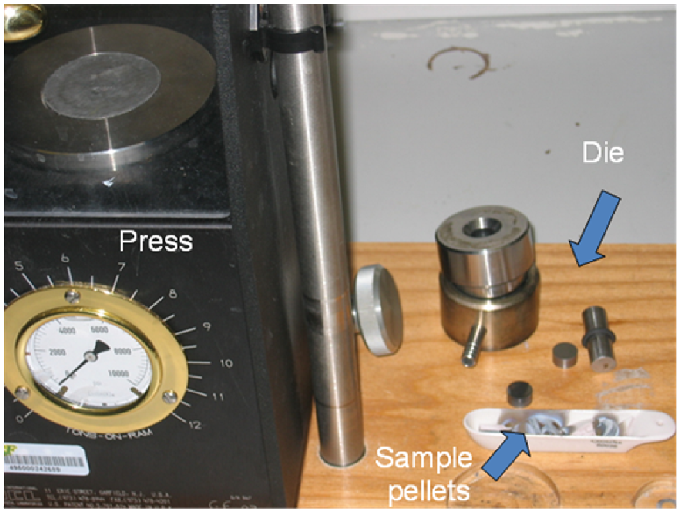

Figure 4.4 Press system, crucible and annealed pellets

In the annealing process, the vacuum pump and the valve are turned off, the helium and bubbler valves are opened and the tube furnace is turned on to start heating. The electric fan is used to prevent melting of the rubber stopper.

4.3 Analytical tools description

4.3.1 Differential scanning calorimetry (DSC)

This thermo-analytical tool measures the difference in the amount of heat required to increase the temperature of a sample and an inert reference as a function of time and temperature.

The specific Q10-P differential scanning calorimeter manufactured by TA instruments consists of two sealed pans, one is the sample pan and the other is the reference pan (which is generally an empty standard pan) inside a helium filled chamber at 50 psi gas pressure. Figure 4.5 shows the schematic diagram of the DSC cell. The heat flow difference between the two pans is monitored while they are heated, or cooled, uniformly. This can be done at a constant temperature (isothermally) or by changing the temperature at a constant rate [56].

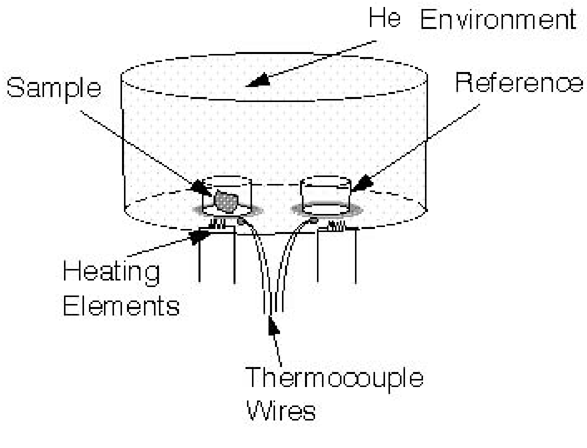

Figure 4.5 DSC cell schematic

The basic principle in this technique is that, when the sample undergoes a physical transformation such as a phase transition, more (or less) heat will need to flow to it than the reference to maintain both the reference pan and the sample pan at the same temperature. The process can be exothermic or endothermic depending whether more or less heat flows to the sample. Endothermic heat flows into the sample as a result of either warming or some endothermic process (glass transition, melting, evaporation, etc.) and exothermic heat flows out if the sample as a result of either cooling or some exothermic process (crystallization, oxidation, etc.).

4.3.2 Thermogravimetric analysis (TGA)

Thermogravimetric analysis uses heat to force reactions and physical changes in the materials under investigation. TGA measures the amount and rate of change in the weight of a material due to dehydration, decomposition, and oxidation as a function of temperature or time in a controlled atmosphere. Characteristic thermogravimetric curves occur for specific materials due to unique sequences of physicochemical reactions occurring over specific temperature ranges and heating rates.

The specific TGA used is the Q600 series; it provides a true simultaneous (SDT) measurement of weight change (TGA) and heat flow (DSC) on the same sample. A matched Platinum/Platinum-Rhodium thermocouple pair embedded in the ceramic beams provides direct sample [57], reference, and differential temperature measurement and a dual balance mechanism gives an accurate weight loss/gain measurement. The schematic cross-sectional diagram of Q600 SDT is shown in Figure 4.6

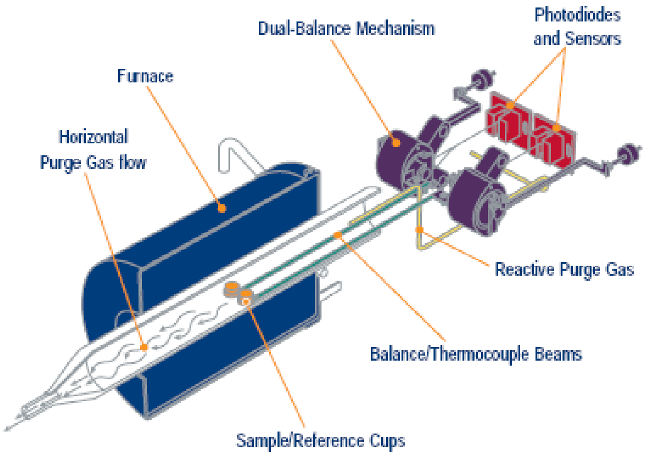

Figure 4.6 Q600 balance/furnace schematic diagram [58]

The balance operates on a null-balance principle. At the zero position, equal amounts of light shine on the two photodiodes. If the balance moves out of the null position an unequal amount of light shines on the two photodiodes. Current then is applied to the meter movement to return the balance to the zero position. The amount of current applied is proportional to the weight loss or gain.

4.3.3 X-ray diffractrometer (XRD)

X-ray Powder Diffraction (XRD) is an efficient analytical technique used to characterize and identify unknown crystalline materials. Monochromatic x-rays are used to determine the interplanar spacings of the unknown materials. X-rays are electromagnetic radiation similar to light, but with a much shorter wavelength. They are produced when electrically charged particles of sufficient energy are decelerated. In an x-ray tube, the high voltage maintained across the electrodes draws electrons toward a metal target (the anode). X-rays are produced at the point of impact, and radiate in all directions.

With this technique the samples are analyzed as powders with grains in random orientations to insure that all crystallographic directions are "sampled" by the beam. The basic principle of operation of the XRD spectrometer is based on Bragg's law. When the Bragg conditions for constructive interference are obtained, a "reflection" is produced, and the relative peak height is generally proportional to the number of grains in a preferred orientation.

According to Bragg's law to obtain constructive interference, the path difference between the two incident and the scattered waves, which is $2.d.\sin\theta$, has to be a multiple of the wavelength λ. For this case, the Bragg law then gives the relation between interplanar distance d and diffraction angle θ:

$$2.d.\sin\theta = n.\lambda \tag{4.1}$$

Where n is an integer, λ is the wavelength of x-rays, d is the spacing between the planes in the atomic lattice, and θ is the angle between the incident ray and the scattering planes; Since λ is known, θ can be measured, the d-spacings can be calculated using the Bragg's equation. In the Figure 4.7 is shown the basic principles of constructive interference of the scattered x-rays.

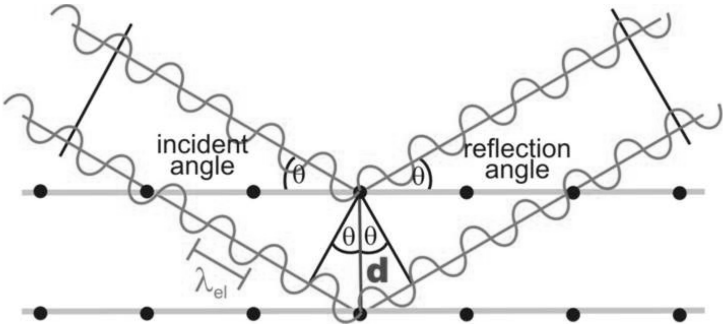

Figure 4.7 Constructive interference of reflected waves

The basic geometry of an x-ray diffractometer is shown in Figure 4.8, it has a source of monochromatic radiation and an x-ray detector situated on the circumference of a graduated circle centered on the powder specimen. The detector and specimen holder are mechanically coupled with a goniometer so that a rotation of the detector through 2θ degrees occurs in conjunction with the rotation of the specimen through θ degrees, a fixed 2:1 ratio. Divergent slits, located between the x-ray source and the specimen, and between the specimen and the detector, limit scattered (non-diffracted) radiation, reduce background noise, and collimate the radiation.

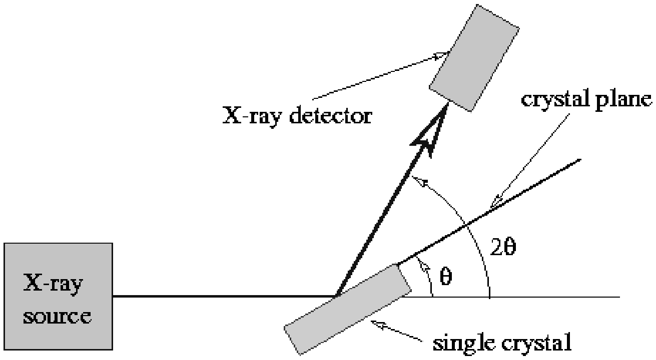

Figure 4.8 Basic geometry of an x-ray diffractometer

4.3.4 Scanning electron microscope (SEM)

The Scanning Electron Microscope (SEM) is a type of microscope capable of producing high resolution images of a sample surface using electrons rather than light to form an image. Electron microscopy takes advantage of the wave nature of rapidly moving electrons. Where visible light has wavelengths from 4,000 to 7,000 Angstroms, electrons accelerated to 10,000 KeV have wavelengths of 0.12 Angstroms. Optical microscopes have their resolution limited by the diffraction of light to about 1000 diameters magnification. The Hitachi S800 scanning electron microscope in the present study is limited to magnifications of around 3,000,000.

The SEM uses the secondary electrons when a focused electron beam is incident on the specimen to form the image. The secondary electron signal provides information about the surface of a specimen. Since secondary electrons do not diffuse much inside the specimen, they are most suitable for observing fine structure of the specimen surface. Figure 4.9 shows the signals generated in an electron beam and specimen interaction.

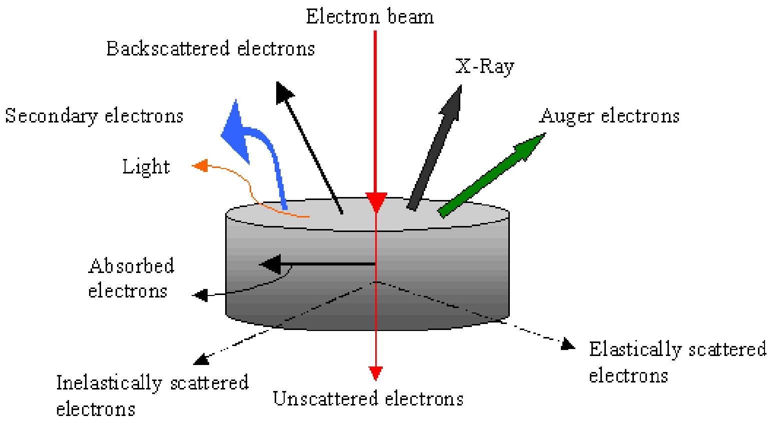

Figure 4.9 Electron beam and specimen interaction signals [59]

The basic diagram of the operation of the Hitachi S800 SEM is shown in Figure 4.10. Electrons from a filament in an electron gun are beamed at the specimen inside a vacuum chamber. That beam is collimated by electromagnetic condenser lenses, focused by an objective lens and then swept across the specimen at high speed. The secondary electrons are detected by a scintillation material that produces flashes of light from the electrons. The light flashes are then detected and amplified by a photomultiplier tube.

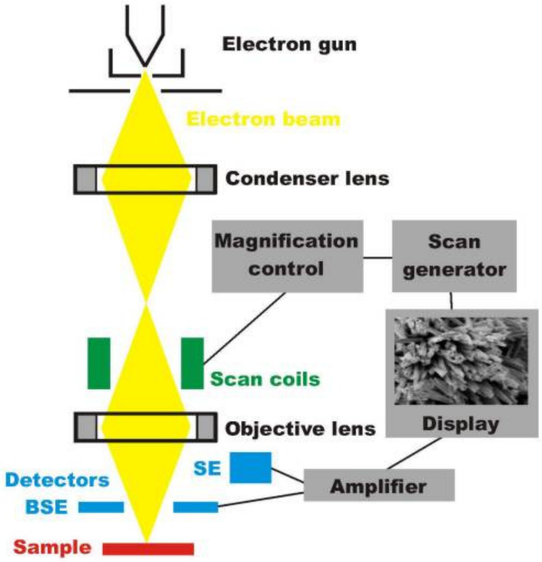

Figure 4.10 Schematic working principle diagram for a SEM [60]

4.3.5 Energy dispersive x-ray spectroscopy (EDS)

Another important signal that can be analyzed by the Hitachi S800 SEM, when the electron beam- specimen interaction occurs is the x-ray emission. EDS identifies the elemental composition of materials imaged in a Scanning Electron Microscope (SEM) for all elements with an atomic number greater than boron (B). Most elements are detected at concentrations of order 0.1% excluding hydrogen. When the electron beam of the SEM hits the sample surface, it generates x-ray fluorescence from the atoms in its path. The energy of each x-ray photon is characteristic of the element which produced it. The EDS microanalysis system collects the x-rays, sorts and plots them by energy, and automatically identifies and labels the elements responsible for the peaks in this energy distribution. The liquid nitrogen cooled detector is used to capture and mapped the x-ray counts continuously.

4.3.6 Pressure composition temperature (PCT) apparatus

The instrument used is the PCTPro-2000 manufactured by Hy-Energy, USA. It is an automated Sieverts type instrument for measuring gas absorption/desorption properties of materials designed mainly for hydrogen storage and metal hydride applications. Important measurements that can be done with this instrument are PCT, gas sorption kinetics, heat-of-formation, cycle-life kinetics, cycle-life PCT, volume calibration and packing density measurements. Most of the concepts were explained in chapter 3.

In the Sieverts technique, a calibrated reference volume at a constant temperature is filled with gas to a measured pressure and then opened to the sample chamber, the gas uptake by the sample is calculated from the change in the gas pressure in the system. Hydrogen uptake is represented by the hydrogen-to host atomic ratio, H/X, by analogy with the hydrogen-to-metal ratio for a metal, H/M. Similarly, the gas release by the sample is measured from the gas pressure difference in the system. A helium bottle (purity 99.9999%) is used for calibrating the volume and for purging air from the line. The Sieverts type volumetric hydrogen sorption system is shown in Figure 4.11, where Res 1 and Res 2 are the gas reservoirs.

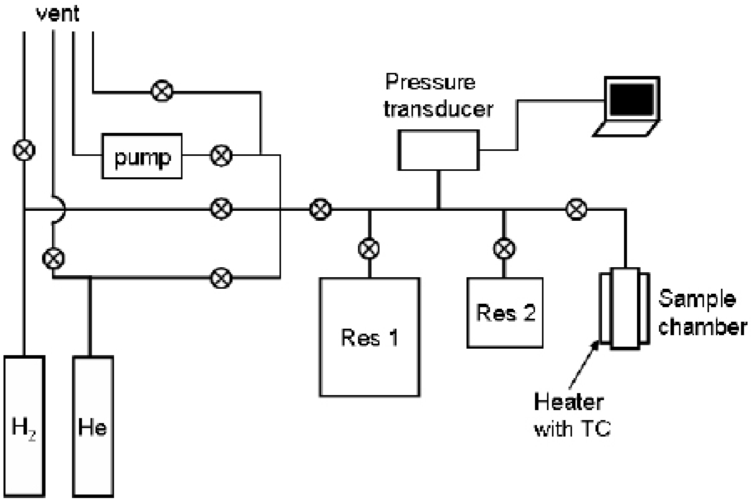

Figure 4.11 Sieverts type volumetric apparatus [61]

As it is mentioned above the PCTPro-2000 is a Sieverts' type instrument that uses the difference in pressure to calculate the amount of hydrogen absorbed or desorbed, the basic indicator diagram developed by Hy-Energy is depicted below in Figure 4.12

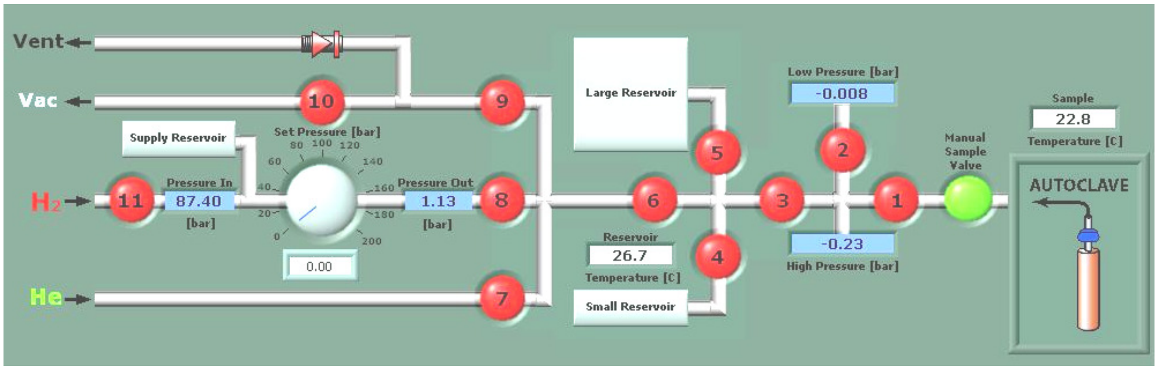

Pressure In 87.40 [bar]

0.00

Pressure Out 1.13 [bar]

Reservoir 26.7 Temperature [C]

Low Pressure [bar] -0.008

-0.23 High Pressure [bar]

Sample 22.8 Temperature [C]

Figure 4.12 Indicator diagram of the PCTPro-2000 apparatus

Valves 1 to 11 are air operated automatic valves and they are normally closed, except valve 1 which is a normally open valve. The description of the valve operation is as follow:

- Valve 1 - Main valve that delivers aliquots of gas to and from the sample. It is a normally open valve because it maintains its open position for the majority of the measurement time. It is closed only when reservoir volumes are being charged with gas and during some preparation processes.
- Valve 2 - Protects the low-pressure transducer from manifold pressures that are greater than the maximum allowable pressure of the low-pressure sensor.
- Valve 3 - Admits gas into the upper manifold. The smallest calibrated reservoir volume consist of the upper manifold between valves 1, 2 and 3; it has a total volume on the order of 5 cubic centimeters.
- Valve 4 - Provides access to the medium sized calibration volume that has a volume of approximately 145 cubic centimeters.
- Valve 5 - Provides access to the largest of the calibration volumes. This volume is approximately one liter.
- Valve 6 - Separates the lower manifold from the gas supply and vacuum manifold.
- Valve 7 - Supplies helium gas to the gas supply manifold to facilite purging, leak testing and calibrations.
- Valve 8 - Provides hydrogen to the gas supply manifold.
- Valve 9 - Connects the gas supply manifold to the vent and vacuum system.

- Valve 10 - Connects the vent system to the vacuum line.
- Valve 11 - Test gas supply valve that connects to the test gas supply line.

4.3.7 Thermal programmed desorption or reaction (TPD/TPR)

The rate of hydrogen absorption (reaction) of a metal hydride sample is function of temperature as shown in the metal hydrides chapter. The temperature at which the maximum rate is observed is characteristic of the metal hydride, the metal and its interaction with the hydrogen gas. Temperature Programmed Reaction (TPR) is a technique in which the amount of reaction is monitored as a function of temperature. The temperature is raised in a linear fashion so that a suitable detection system can record a characteristic reaction profile or fingerprint of the sample being tested. The monitoring is done with a high sensitivity thermal conductivity detector (TCD).

In an analogous manner, gases that were previously absorbed during chemisorption process can be desorbed by ramping again the temperature to sufficiently high values to break the chemical bonds holding the gas molecules (or atoms); again the TCD signal is proportional to the quantity of molecules desorbed as thermal energy overcomes the binding energy. This type of experiment is called Temperature Programmed Desorption (TPD).

In Figure 4.13 is illustrated the basic diagram of the Autosorb-1 equipment manufactured by Quantachrome Instruments.

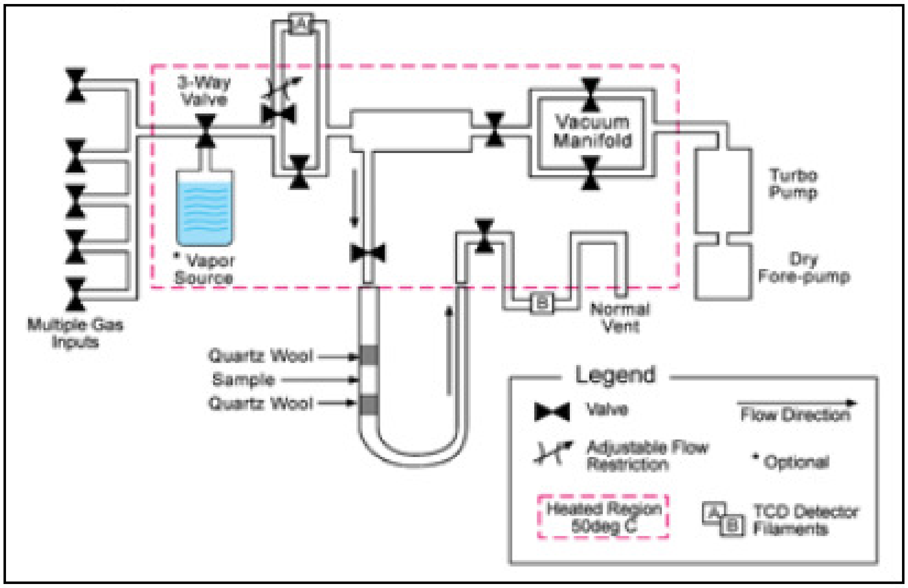

Figure 4.13 Basic diagram of the Autosorb– 1 TPD/TPR apparatus [62]

The sample between two quartz wool pieces is purged with nitrogen in order to avoid oxygen in the sample and inside the lines. Then for the TPR measurement, a mixture of 95% Argon and 5% hydrogen flows over the sample with a temperature ramping, a monitoring process is conducted recording the amount of hydrogen absorbed based on the signal in the B TCD detector filament and compared with the A TCD filament. For the TPD measurement the hydrogen mixture is replaced by nitrogen and the TCD is changed to TPD option.

4.3.8 Fourier transform infrared spectrometer (FT-IR)

Infrared (IR) spectroscopy is a chemical analytical technique, which measures the infrared intensity versus wavelength of light. Based upon the wavenumber, infrared light can be categorized as far infrared (4 ~ 400cm^{-1}), mid infrared (400 ~ 4,000cm^{-1}) and near infrared (4,000 ~ 14,000cm^{-1}). Infrared spectroscopy detects the vibration characteristics of chemical functional groups in a sample. When an infrared light interacts with the matter, chemical bonds will stretch, contract and bend. As a result, a chemical functional group tends to absorb infrared radiation in a specific wavenumber (frequency) range regardless of the structure of the rest of the molecule.

In a Fourier transform infrared spectrometer, the light passes through an interferometer which creates constructive and destructive interference pattern of two light beams, the recombined beam passes through the sample. The sample absorbs all the different wavelength characteristics of its spectrum, and this subtracts specific wavelengths from the interferometer. The detector now reports variation in energy versus time for all wavelengths simultaneously. A laser beam is superimposed to provide a reference for the instrument operation. A basic diagram of the Perkin-Elmer Spectrum One FTIR Spectrometer is shown in Figure 4.14

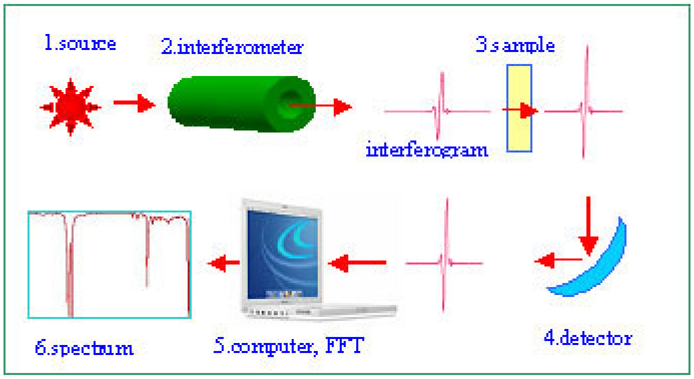

Figure 4.14 Perkin-Elmer Spectrum One FTIR spectrometer diagram [63]

Determining these frequencies allows identification of the sample's chemical environment, since chemical functional groups are known to absorb radiation at specific frequencies. The intensity of the absorption is related to the concentration of the component. Intensity and frequency of sample absorption are depicted in a two-dimensional plot called a spectrum. Intensity is generally reported in terms of percent transmittance, the fraction of the light that passes through it.

4.3.9 Gas chromatography and mass spectroscopy (GC-MS)

Two techniques are combined to form a single method of analyzing mixtures of chemicals or evolving gas. Gas chromatography separates the components of a mixture and mass spectroscopy characterizes each of the components individually. By combining the two techniques, the qualitatively and quantitatively composition of a solution containing a number of chemicals can be known.

Gas chromatography is a chemical analysis instrument for separating chemicals in a complex hydride sample. A gas chromatograph uses a flow-through narrow tube known as a column, through which different chemical constituents of a sample pass in a gas stream known as the mobile phase at different rates depending on their various chemical and physical properties and their interaction with a specific column filling, called the stationary phase. As chemicals exit the end of the column, they are detected and identified electronically, those that interact faster will exit (elute from) the column first. The function of the stationary phase in the column is to separate different components, causing each one to exit the column at a different time (retention time). Changing the carrier gas flow rate and the temperature can alter the retention time.

As the individual compounds exit from the GC column, they enter the electron ionization (mass spectroscopy) detector. There, they are bombarded with a stream of electrons causing them to break apart into fragments. These fragments can be large or small pieces of the original molecules. The positive fragments which are produced (cations and radical cations) are accelerated in a vacuum through a quadrupole ion analyzer (Figure 4.15) and are sorted on the basis of mass-to-charge (m/e) ratio. Since the bulk of the ions produced in the mass spectrometer carry a unit positive charge, the value m/e is equivalent to the molecular weight of the fragment.

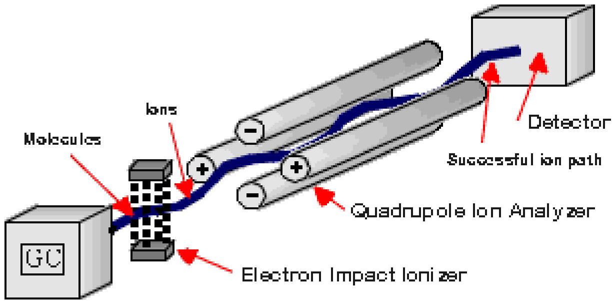

Figure 4.15 General schematic of a mass spectrometer [64]

CHAPTER 5

EXPERIMENTAL RESULTS

5.1 $ZrMn_2$ alloy

According to [65], a method of preparing an alloy of zirconium and manganese suitable for storing hydrogen consists in two steps: make an intimate mixture of Zr and Mn in correct stoichiometric ratio and heat the sample between 900 and 1150 °C. As discussed in the last chapter, the intimate mixture is done using a straightforward, repeatable, and inexpensive procedure, ball milling under H_2 atmosphere. The annealing was applied for 10 hours in a helium atmosphere at 1100 °C.

5.1.1 XRD results

Figure 5.1 demonstrates the representative X-ray diffraction profiles of Zr-Mn mixtures subjected to ball milling and subsequent annealing. The Zr-Mn mixtures ball milled for two different milling duration (10h and 24h) exhibit identical x-ray patterns with a diffraction peak from the (411) Mn lattice plane. However, for the case of 24h ball milled and annealed sample at 1100 ºC, in addition to Mn reflections, peaks correspond to $ZrMn_2$ and ZrO_2 are indexed with the increasing crystallinity; the peak comparison was done using PANalytical X'pert Highscore software (see Appendix A) and based on the literature [65-69]. Besides, we have calculated the crystallite sizes and lattice strains of high intensity Mn peaks based on the Scherrer's formula. These are given in the Table 5.1. Ball mill induced nanocrystallization and subsequent annealing at high temperature thus improves the formation of $ZrMn_2$ intermetallic phase.

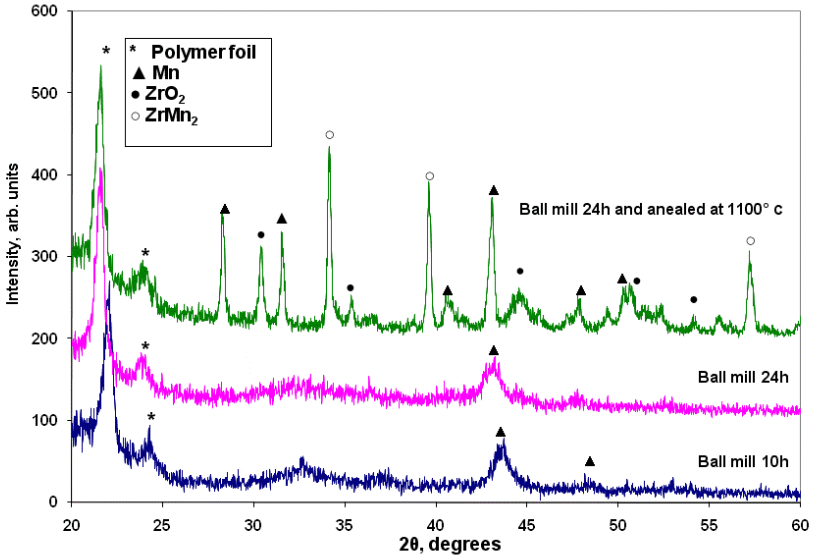

Figure 5.1 XRD spectra of $ZrMn_2$ alloy, ball milled (under H_2) and annealed

Table 5.1 Crystallite size and lattice strain for the Mn reflection based on Scherrer's formula

Sample details	Peak position (° 2θ)	Phase (hkl)	FWHM (° 2θ)	Crystallite size (nm)	Lattice strain (%)
Zr-Mn mix (BM 10h)	43.186	Mn (411)	0.787	12.4	0.861
Zr-Mn mix (BM 24h)	43.580	Mn (411)	0.787	12.5	0.852
Zr-Mn (BM 24h + Annealed 10h)	43.058	Mn (411)	0.275	48.8	0.283
Zr-Mn (BM 48h + Annealed 10h)	43.438	Mn (411)	0.236	62.9	0.234

The differences between the x-ray profiles of the Zr-Mn mixtures ball milled for 24 and 48 hours and then annealed at 1100 °C are shown in Figure 5.2. Reduction in the relative intensities of Mn and ZrO_2 peaks are observed with longer ball milling times, especially in the angular range of 27 to 33°. The larger crystallite size of ~62.9 nm was found for the 48h ball milled and annealed samples (Table 5.1).

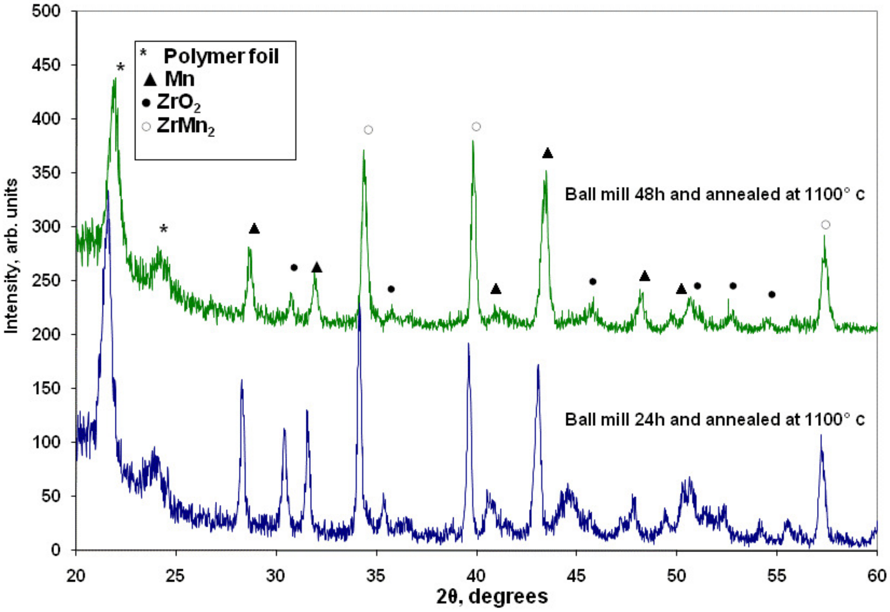

Figure 5.2 XRD spectra of ball milled and annealed $ZrMn_2$ alloy

For the systematic peak identification and profile comparison, additional experiments were carried out. A sample of pure Zirconium and pure Manganese were annealed separately for 8 hours at 1100 °C in air, oxidizing the two elements and forming zirconium oxide and manganese oxide respectively. The Zr-Mn mixture with stoicheometric ratio of 1:2 has been manually mixed in a mortar for 15 minutes. Figure 5.3 shows the XRD profiles of the pure elements (Zr, Mn), oxides (ZrO_2, MnO) , Zr-Mn mixture and the intermetallic $ZrMn_2$ phase as obtained from the 48h ball milled and annealed sample. Though partial formation of $ZrMn_2$ is present after ball milling the Zr-Mn mixture and subsequent annealing at high temperature, the XRD profiles exhibit evidence of unreacted Zr and Mn and their oxide peaks. This may be due to the lack of a complete conversion into alloy and the getter activity of the parent metals.

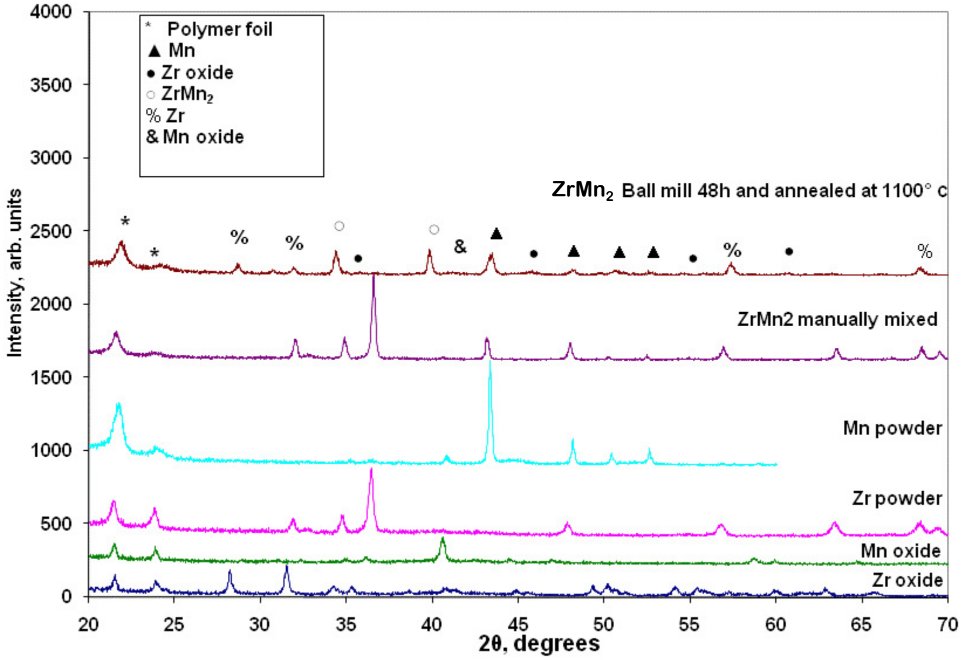

Figure 5.3 XRD profiles of the pure elements (Zr, Mn), oxides (ZrO_2, MnO), Zr-Mn mixture and ball milled-annealed $ZrMn_2$ alloy

In order to synthesize a high purity $ZrMn_2$ intermetallic alloy, an extensive investigation was conducted. The sample after being ball milled for 48 hours was pelletized at a pressure of 7500 psi and then annealed, keeping the same parameters of the powder sample.

The light purple line in Figure 5.4 shows a reduction in the relative intensity of the Zr peaks (28.5, 33°) and Mn peaks (43, 47.5, 50, 53°) compared with the green line. This explains that pelletizing before annealing enhances a better reaction of the Mn and

Zr due to the shorter diffusion paths between the particles. The structural characterization of the $ZrMn_2$ mixture before and after hydrogenation is shown in Figure 5.5. It can be seen that the XRD profiles of the sample before and after hydrogenation exhibits no change in the profile shape (FWHM), the relative intensities, number of peaks and negligible formation of hydride peaks. Hence it complements the result of poor hydrogenation-dehydrogenation kinetics as explained in the next section.

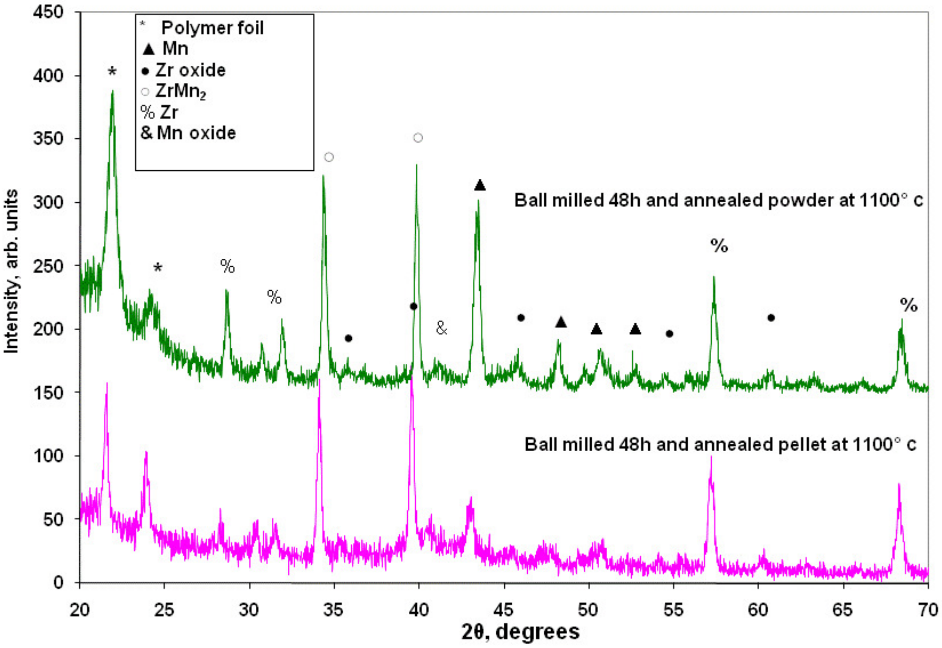

Figure 5.4 XRD spectra of $ZrMn_2$ with different annealed samples

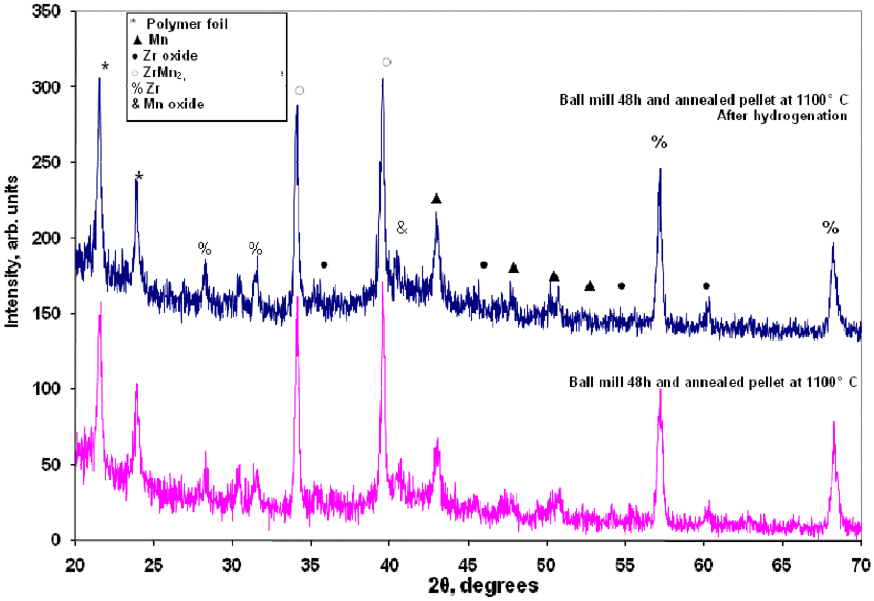

Figure 5.5 XRD spectra of $ZrMn_2$ before and after hydrogenation

5.1.2 PCT and desorption kinetics analysis

For the PCT and desorption kinetics measurements, a first evacuation process of the sample is completed for 4 hours, and cycle-life kinetics at 300 °C for 5 hours to remove the surface oxide layer and activating the material. The hydrogen desorption kinetics of the 48 hour ball milled alloy without annealing is presented in Figure 5.6; the concentration of hydrogen in is too low ($\sim 1*10^{-3}$ total weight %) and no substantial difference is seen even at 350 and 390 °C. On the other hand, the desorption kinetics of the sample after being ball milled, pelletized and annealed is shown in figure 5.7, here the hydrogen concentration is comparatively better and it invariably depends on the dehydrogenation temperature; for example, the hydrogen content at 300 °C is 0.014%, at 350 °C is 0.016% and at 390 °C is 0.026%.

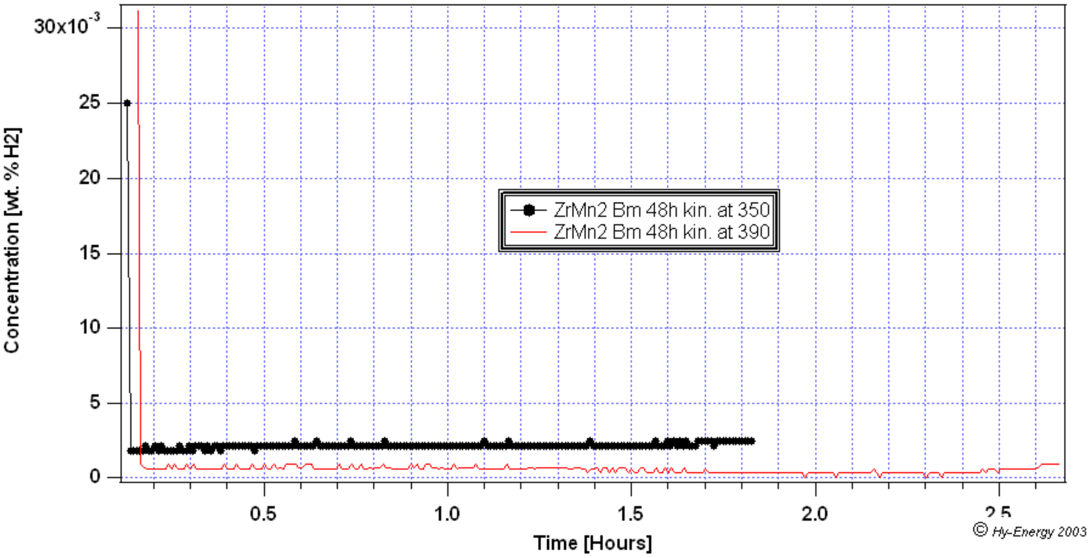

Figure 5.6 Desorption kinetics of ball-milled $ZrMn_2$ mixture at 350 and 390˚C

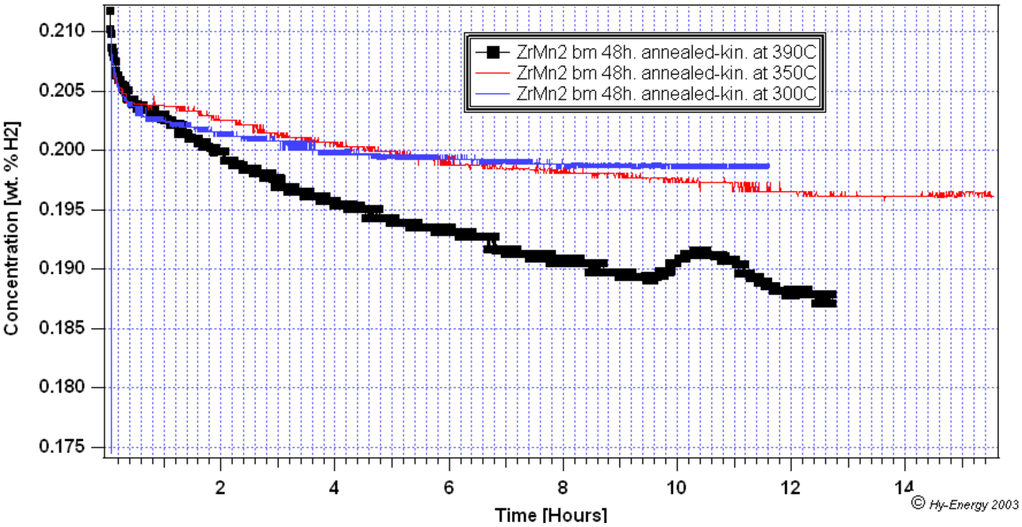

Figure 5.7 Desorption kinetics of ball milled-annealed $ZrMn_2$ alloy at 300, 350 and 390˚C

Although a significant improvement in the hydrogen storage property (~ 26 times greater) was accomplished with the annealing treatment, the hydrogen content of the metal hydride is still too low for a useful hydrogen compression device.

A possible way to improve the hydrogen storage capacity of this metal hydride is descry ibed by [66-69], whereas, an arc melting process is applied to the Zr-Mn powder mixture, heating the sample above the highest melting point of both elements (3371 °F, 1855 °C). Other experiments were carried out using different analytical tools but no practical information was observed, for example in PCT, no plateau pressure was obtained.

5.2 ZrNi alloys

As it is mentioned on chapter 3, the AB_2 and AB metal hydride families and mostly the Zr based have optimum characteristics for hydrogen compression applications. The principal features of these compounds are moderate high hydrogen decomposition temperature, fast kinetics, relative high equilibrium pressures and hydrogen content.

ZrNi is more thermally stable, presents better impurity resistance and kinetics compared with ZrMn2. In this study three compositional alloys were investigated: (i) ZrNi 30/70 by weight, (ii) ZrNi 70/30 by weight and (iii) the ZrNi (1:1). Prior to the analytical runs, the as-received commercial ZrNi 30/70 and ZrNi 70/30 samples were mixed manually in a mortar inside the glove box for 15 minutes; for the ZrNi alloy, a mixture of ZrNi 70/30 ($Zr_{1.5}Ni$) and ZrNi 30/70 ($ZrNi_{3.63}$) in a molar ratio of 5.26:1 was ball milled for 12 hours at 300 rpm and annealed at 1100 °C for 10 hours. Although there is vast information available about ZrNi alloys [71-77], the intermediate compositional alloys ZrNi 70/30 and ZrNi 30/70 have been sparsely studied [70].

5.2.1 XRD analysis

Figure 5.8 shows the XRD profiles of the “as-received” ZrNi 30/70 and ZrNi 70/30 alloys, all the peaks were indexed and matched by the XRD information given in [70-72]. An extensive analysis of ZrNi 30/70 (pink curve) profile was also done based on the Highscore software. A close matching of $ZrNi_5$ intermetallic phase has been found and the complete data analysis is given in Appendix B. For the ZrNi 70/30, the XRD (blue curve) peaks are closely matched with the library reflections of $ZrNiH_3$ and ZrH_2 (see Appendix B).

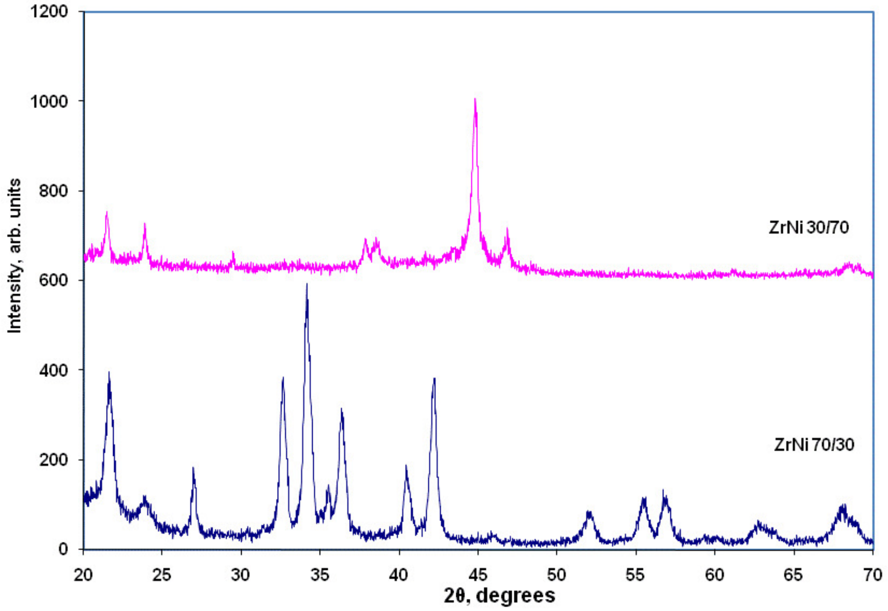

Figure 5.8 XRD spectra of ZrNi 30/70 and ZrNi 70/30

The XRD analysis of the ball milled ZrNi molar ratio 1:1 is represented in Figure 5.9. Three different ball milling times (such as 3, 5 and 12h) were used. Although the patterns show amorphous structures, incipient peaks at 36.2 and 43.5° represent the ZrNi phases. The full width at half maximum (FWHM) of the ZrNi reflection decreases with increasing milling duration and hence reduction in the crystallite sizes.

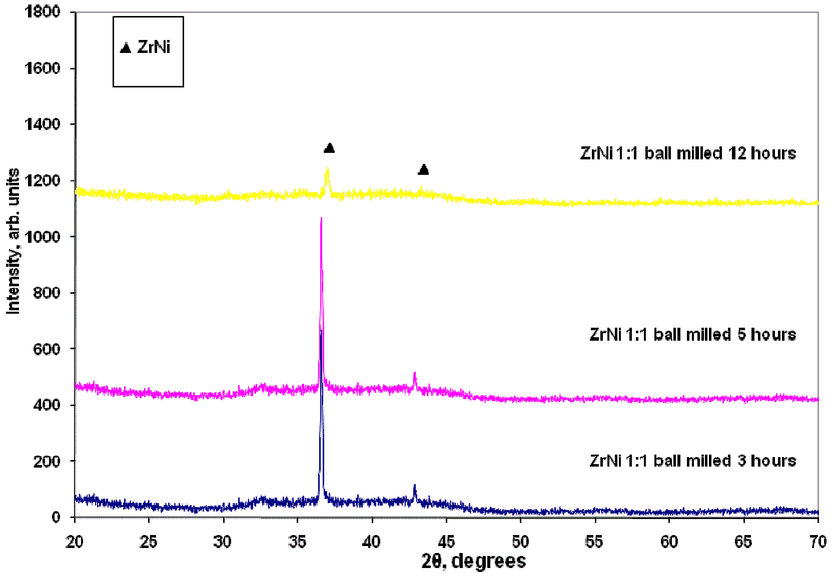

Figure 5.9 XRD spectra of ZrNi 1:1 ball milled 3, 5 and 12 hours

In order to obtain perfect crystalline structures, the ZrNi samples after being ball milled are subjected to pelletization and annealing at 1100 °C for 10 hours. The XRD spectra of the hand mixture and ball milled (3h, 5h and 12h)-annealed samples are shown in Figure 5.10. The light blue line profile represents the ZrNi alloy, ball milled 12 hours and annealed for 10 hours. It can be seen, in addition to ZrNi peaks formation at 27, 35.8, 39.1, 44.2 and 50°, other undesirable peaks from the parent compounds such as ZrNi 70/30 and ZrNi 30/70 are still present, indicating incomplete reaction. Another undesirable peak (ZrNi oxide) occurs at 32.2° due to the possible air exposition in the ball mill or anneal process is seems plausible. The ZrNi structure at 5 and 12 hours ball milled, shows no significant differences, meaning that similar ZrNi structures can be achieved with short milling times (5 hours)

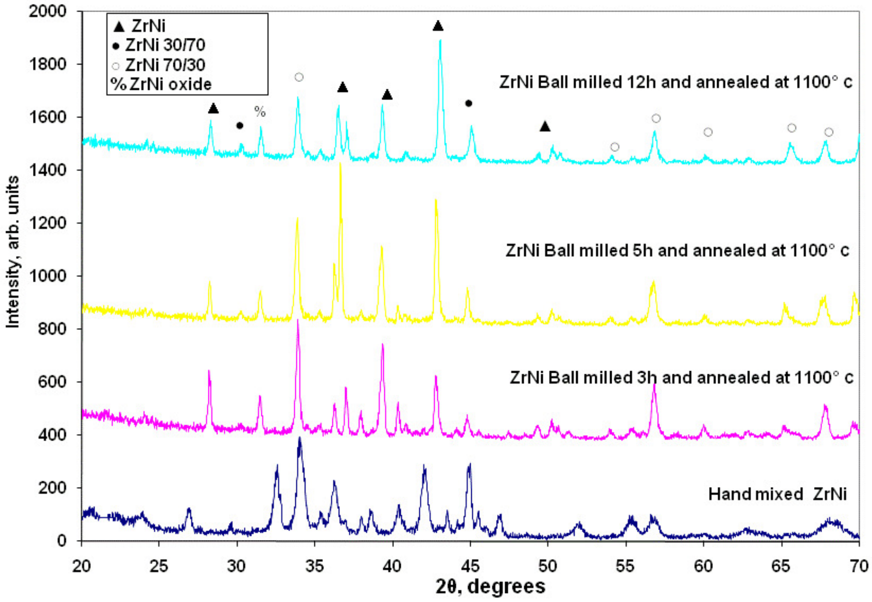

Figure 5.10 XRD spectra of ball milled-annealed ZrNi 1:1 alloy

5.2.1.1 XRD analysis before and after hydrogenation

The XRD analysis of ZrNi70/30 before and after hydrogenation is shown in Figure 5.11 below.

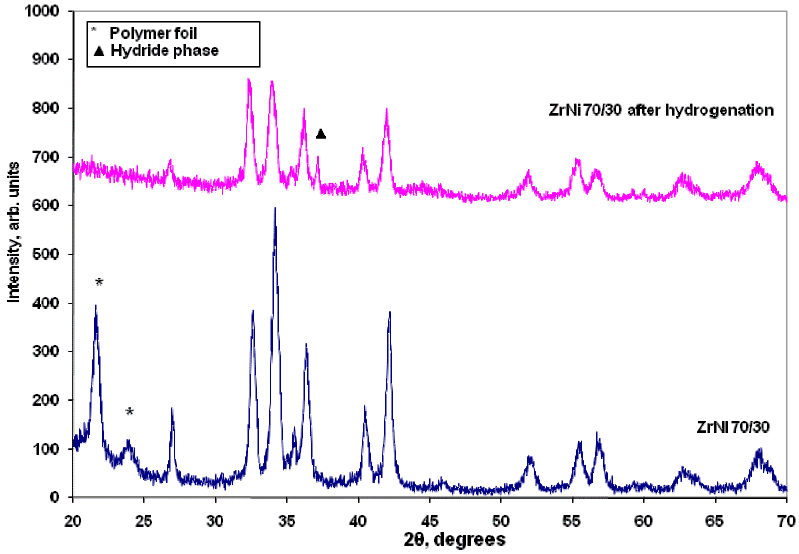

Figure 5.11 XRD spectra of ZrNi 70/30 before and after hydrogenation

The XRD spectra of ZrNi 70/30 in Figure 5.11 shows a significant change in the intensity of the peaks in ZrNi 70/30 hydride compared with the unhydrided sample (33.2, 34.2, 36.5 and 43°) and the presence of a new peak (36.7°) attributed to the ZrNi 70/30 hydride phase. The crystallite sizes of the $ZrNiH_3$ (~48 nm) and ZrH_2 (~39 nm) are calculated and comparable with the unhydrided sample (see Appendix B).

The 12h ball milled ZrNi 1:1 before and after hydrogenation shows a peak height increment of 450% at 36.6° (Figure 5.12), even though, there is a relative change in the structure. The hydrogen storage property seems very poor as obtained from the PCT measurement as explained in the next section. This is due to ball mill induced amorphization.

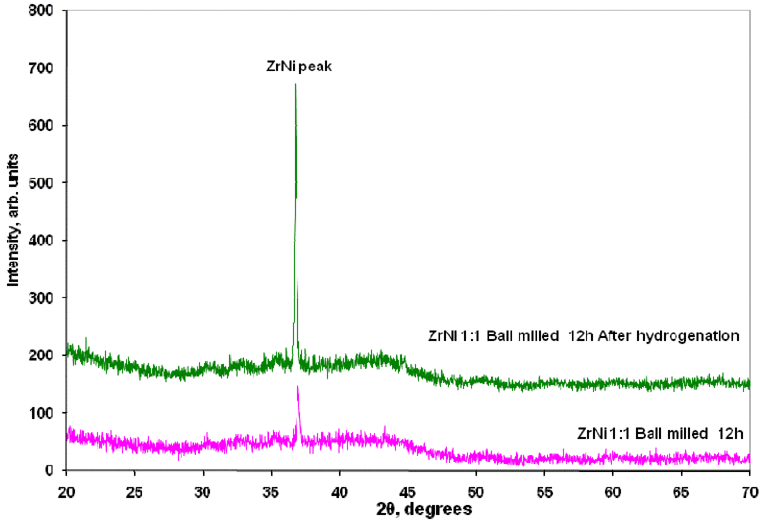

Figure 5.12 XRD spectra of ball milled ZrNi 1:1 before and after hydrogenation

Similarly, in Figure 5.13 the XRD profiles of the hydride and unhydride ZrNi ball milled-annealed samples are shown. The main difference occurs at 35.4 and 43.4°, showing a slight variation in the structure and reduction in the relative intensities due to hydrogen-metal reaction to form ZrNi metal hydride. The average crystallite sizes of ZrNi sample before and after hydrogenation are found to be ~88 and ~48 nm respectively. This suggests that at least 50% particle size reduction can be achieved during hydrogenation and dehydrogenation cycle which in turn causes lattice expansion.

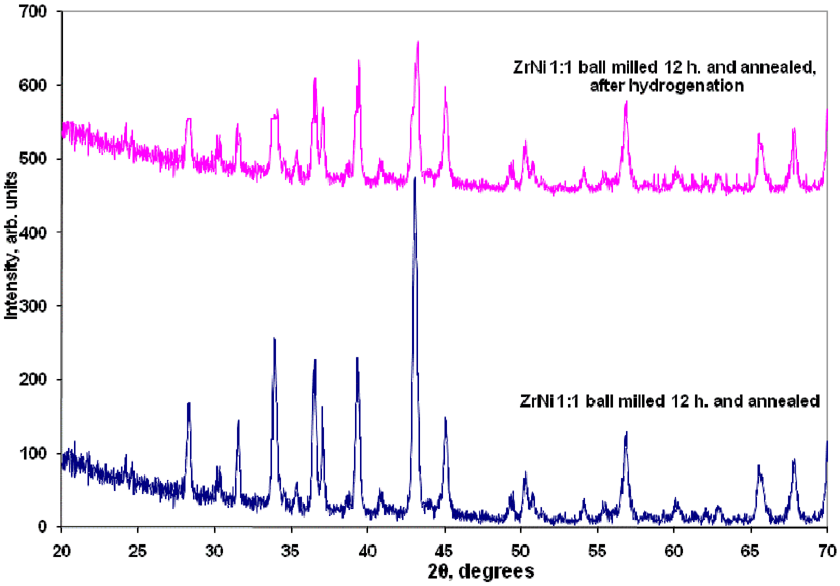

Figure 5.13 XRD spectra of 12h ball milled-annealed ZrNi 1:1 before and after hydrogenation

5.2.2 PCT analysis

Before the kinetics and PCT measurements all the samples (ball milled ZrNi, ball milled/annealed ZrNi, ZrNi 30/70 and ZrNi 70/30) were evacuated at 300 ˚C for 4 hours with the intention of removing O_2 and moisture, after that, a cycle-life kinetic at 300 °C for 5 hours was applied in order to activate the samples. Desorption kinetics of ZrNi 1:1 after being ball milled 12 hours is shown in Figure 5.14. A desorption concentration of 0.02-0.05 wt.% of hydrogen was obtained in the temperature range of 350 °C-390 °C, the reduced hydrogen desorption is attributed to the amorphous structure of as-milled alloy.

Furthermore the kinetics analysis exhibits very slow rate of hydrogen desorption; small quantities of hydrogen continue releasing from the sample after 1 hour.

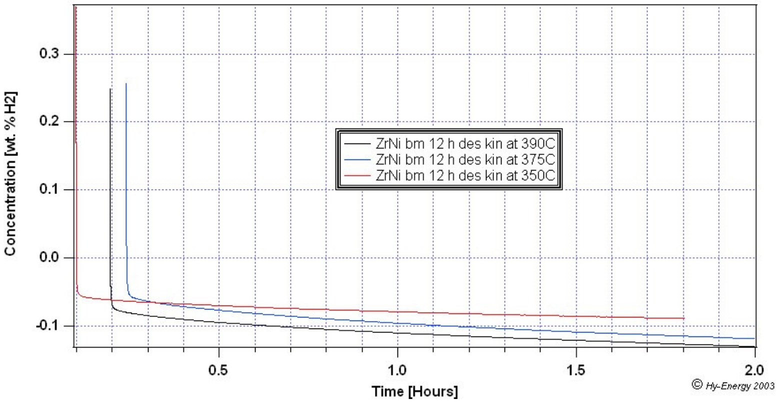

Figure 5.14 Desorption kinetics of ball milled 12h ZrNi 1:1 at 350, 375 and 390 ˚C

An improvement in the kinetics was achieved when the sample was annealed for 10 hours at 1100 °C (Figure 5.15), the hydrogen is completely released after 0.8 hours at 375 and 350 °C, nevertheless, the hydrogen concentration is still low (0.05%). A possible explanation is given in the XRD patterns, not all the ZrNi 70/30 reacts with ZrNi 30/70 to form the saturated ZrNi 1:1 alloy.

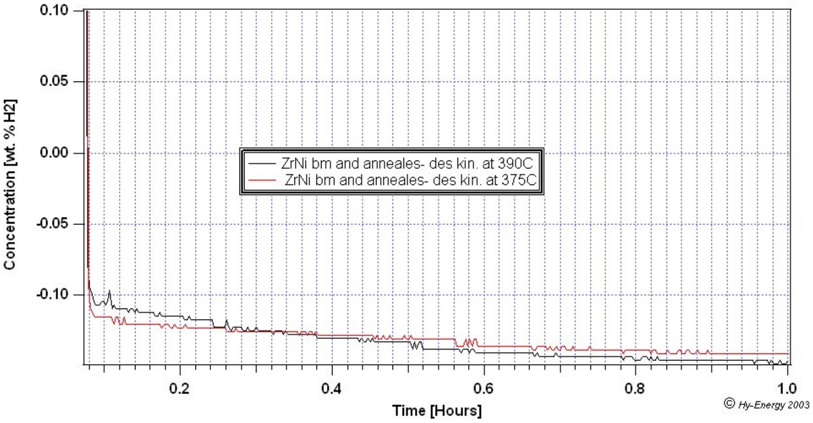

Figure 5.15 Desorption kinetics of ball milled-annealed ZrNi 1:1 at 375 and 390˚C

Figure 5.16 represents the desorption kinetics of ZrNi 30/70 at three different temperatures, 300, 350 and 390 ºC respectively. A complete hydrogen desorption is achieved in 1.75 hours and a hydrogen concentration of 0.37-0.4 wt.% was obtained in the temperature range of 300-390 ˚C. Although the hydrogen content is 8 times greater than ZrNi sample (given in Figure 5.15), the kinetics is rather low for a useful hydrogen compressor applications.

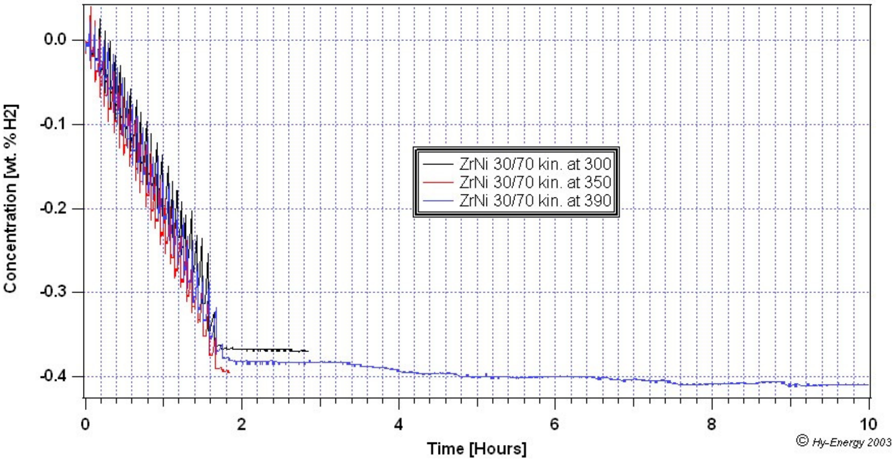

Figure 5.16 Desorption kinetics of ZrNi 30/70 at 300, 350 and 390 ˚C

The desorption kinetic curves of ZrNi 70/30 at various operating temperatures are shown in Figure 5.17. A hydrogen content of 0.7% at 390 ˚C, 0.72% at 375 ˚C, 0.75% at 350 ˚C, 0.7% at 325 ˚C and 0.58% at 300 ˚C is observed. An average total desorption time for the different temperatures of 0.1 hours is seen. As it can be noted, dehydriding kinetics depends strongly on the temperature of the reacting material (metal-metal hydride)

.

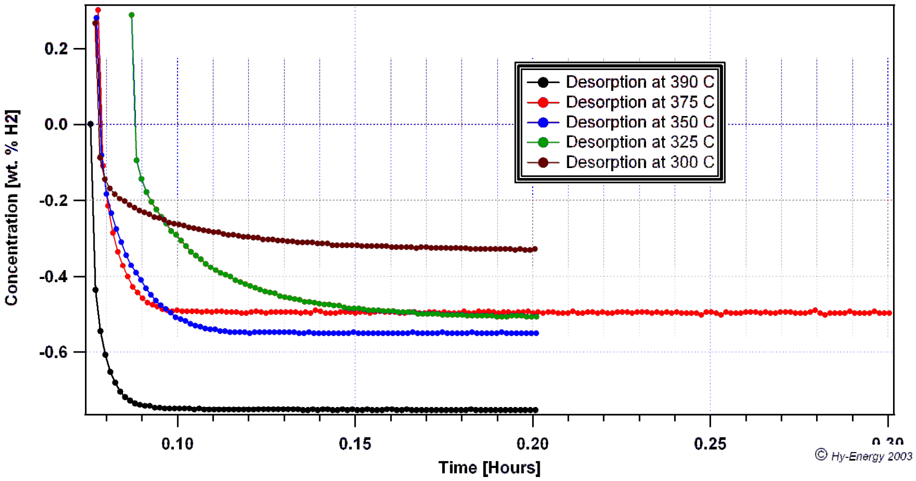

Figure 5.17 Desorption kinetics of ZrNi70/30 at 300, 325, 350, 375 and 390 ˚C

For the quantitative analysis of desorption rate, the data has been plotted in terms of hydrogen pressure at different desorption temperatures (see Figure 5.18). The desorption rate at different temperatures obtained from Figure 5.18 are given in the Table 5.2. It is concluded from this table that the rate of desorption at 390º C is about 5-6 times faster than the sample desorbed at 300 ºC.

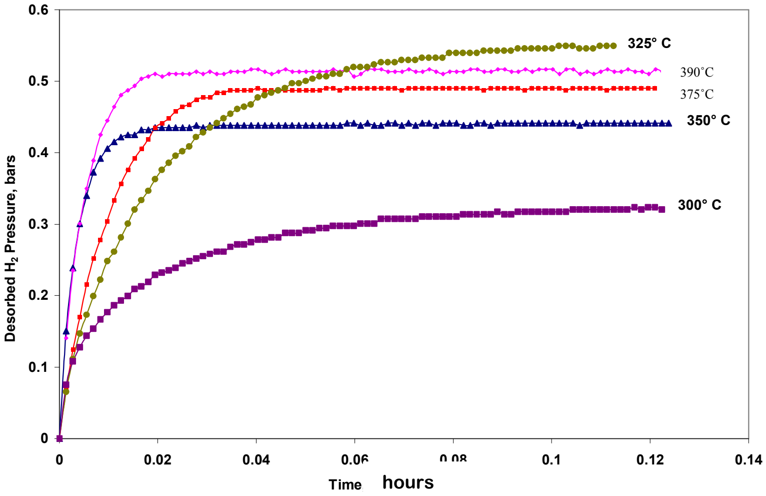

Figure 5.18 Desorption kinetics of ZrNi70/30 at 300,325, 350, 375 and 390˚C in desorbed H_2 pressure units

Table 5.2 Desorption rate with temperature for ZrNi 70/30

Temperature (ºC)	Desorption completion time (minutes)
300	130
325	110
350	90
375	30
390	20

The PCT absorption-desorption diagram of the ZrNi 30/70 alloy is depicted in Figure 5.19. Absence of a well defined plateau pressure for the absorption and desorption curves at various temperatures is an indication of low hydrogen absortion by the mixture at these temperatures. Very high pressures are needed (60 bars) for getting a total absorption-desorption of 0.39 wt%.

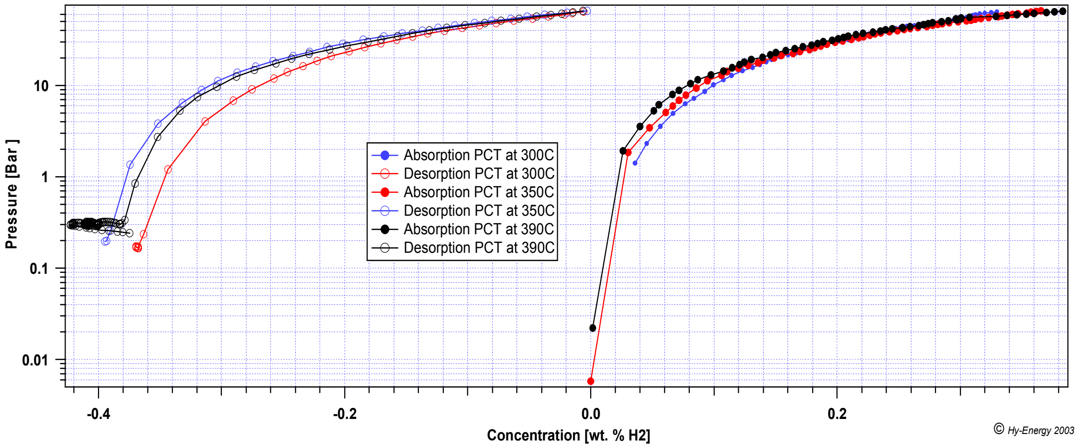

Figure 5.19 Absorption and desorption PCT of ZrNi30/70 at 300, 350 and 390 ˚C

Figure 5.20 illustrates the PCT absorption-desorption result for the ZrNi 70/30 alloy, giving evidence of a typical metal hydride behavior. The plateau region is the most important segment of a PCT plot, which represents the pressure of hydrogen in equilibrium with the metal-metal hydride (α+β) phases, representing the dissociation pressure of the metal hydride at the desired temperature; the temperature indicates the thermal stability of the metal hydride. Moreover, when the temperature rises from 300, 325 , 350, 375 and 390 ˚C causes the plateau pressure to increase and, at the same time, reduces the width of the plateau which represent the miscibility regime of the α and β phase.

As an example, at 375 ˚C hydrogen content of 1 wt% is reached at 13 bars. The enthalpy calculation from the Van’t Hoff equation, based on the PCT desorption plots is shown in appendix C; the enthalpy is an important feature in the hydrogen compressor design.

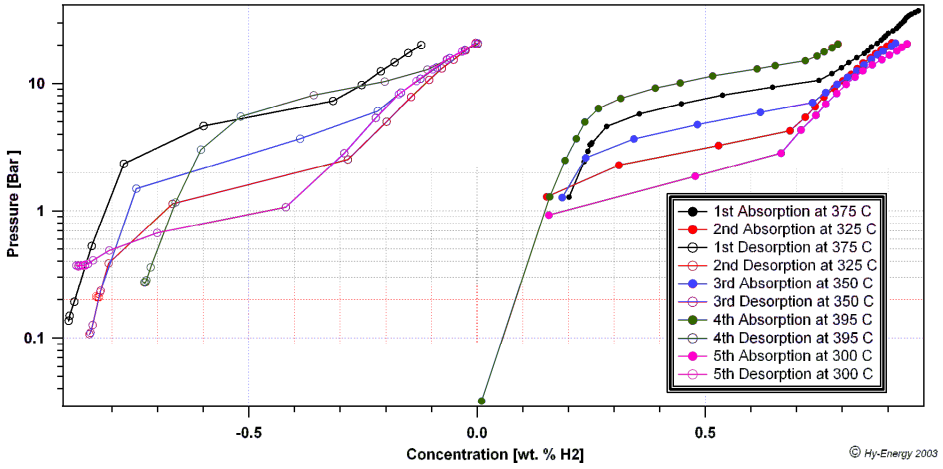

Figure 5.20 Abs/des PCT of ZrNi70/30 at 300, 325, 350, 375 and 390 ˚C

A comparison between ball milled ZrNi and ZrNi 70/30 absorption/desorption PCT at 395 ˚C is shown in Figure 5.21. As can be seen, the lack of a well defined plateau pressure region in the ZrNi alloy, produce a very poor hydrogen concentration. According to the investigation ZrNi 70/30 alloy presents a metal hydride behavior, low kinetics, moderate high equilibrium pressures, and moderate high hydrogen content, conditions that make this alloy the most convenient for hydrogen compression applications.

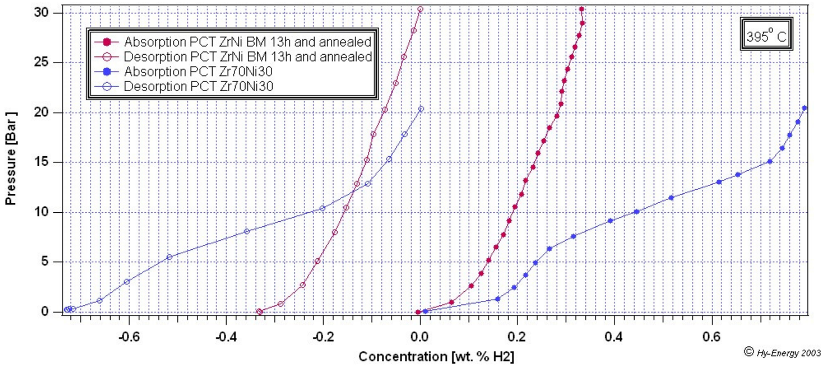

Figure 5.21 Abs/des PCT comparison between ZrNi and ZrNi 70/30 at 395˚C

5.2.3 TGA analysis for ZrNi30/70 and ZrNi70/30

The gravimetric weight loss due to hydrogen decomposition from ZrNi 30/70 is shown in Figure 5.22. The sample powder has been hydrogenated in the PCT apparatus at 390 °C for 4 hours at 50 bars. As it can be noted, the gravimetric weight loss is around 0.09% at 350 °C. Again the TGA profile exhibits weight loss with single step reaction according to the well know metal hydride equation,

$$2ZrNiH_3 = ZrNi + 3H_2 \tag{5.1}$$

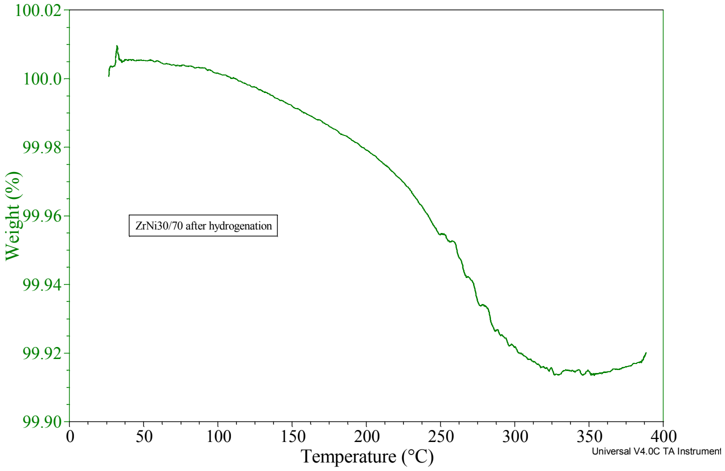

Figure 5.22 TGA profile of ZrNi 30/70 after hydrogenation

Hydrogen decomposition from ZrNi 70/30 reaches a value of 0.62% at 300 °C (Figure 5.23), making the hydrogen desorption property almost 7 times greater compared with ZrNi 30/70 alloy. In the same graph (Figure 5.23), the TGA profile of ZrNi 70/30 is compared with the same hydride alloy after being exposed to air for 30 minutes at room temperature, showing a reduction of 0.2% hydrogen decomposition at 300 °C due to the influence of O_2/moisture picked up by the sample.

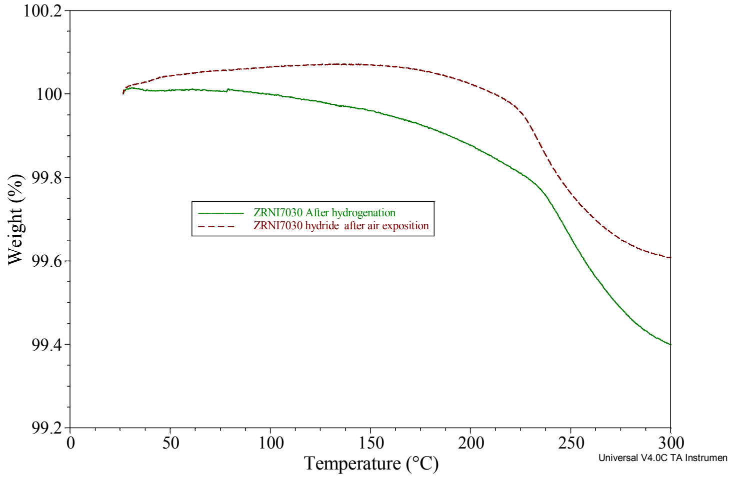

Figure 5.23 TGA profile of hydrogenated ZrNi 70/30 before and after air exposition

5.2.4 SEM imaging of ZrNi 70/30

Figure 5.24 shows the SEM images of ZrNi 70/30 powder particles before and after PCT hydrogenation cycles. Initially, the powder particles present inhomogeneous distribution with irregular morphology. Larger size particles are present in the sample before PCT hydrogen absorption in the order of 10 µm, after PCT hydrogenation runs, the particle average size brought down to is the order of 3 µm. It was also found cracks formed after PCT due to interaction of hydrogen with the metal lattice thus cause the lattice expansion to an appreciable amount; this is a common feature in metal hydrides. A zoom in the crack area of the particle after PCT is shown in Figure 5.25, the image was zoomed 30000x and the crack width is about 0.1 um.

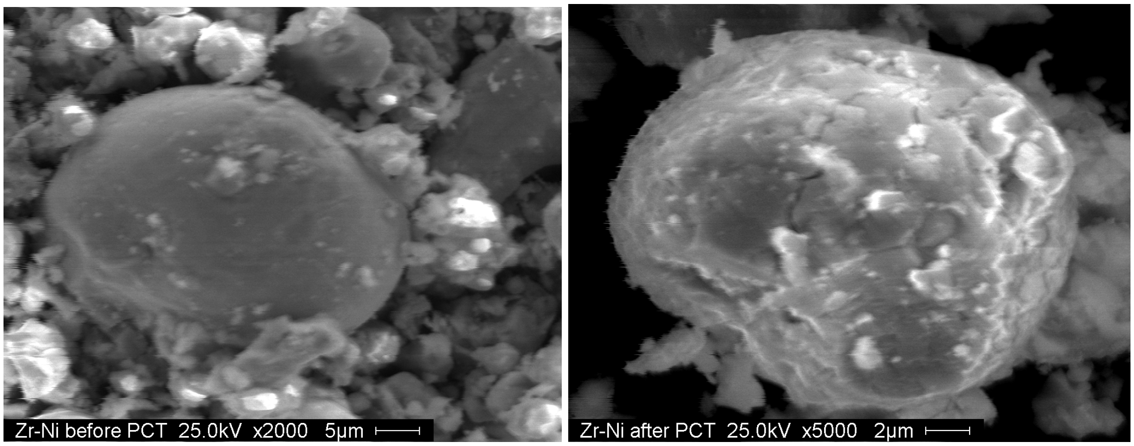

Figure 5.24 SEM image of ZrNi 70/30 before and after PCT runs

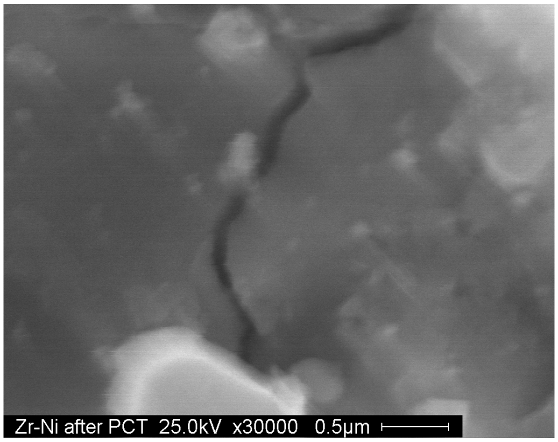

Figure 5.25 SEM image at the large magnification of ZrNi 70/30’s crack

5.3 $Zn(BH_4)_2$ complex hydride

Zinc borohydride $Zn(BH_4)_2$ (8.5 wt% theoretical hydrogen storage capacity) has been synthesized by mechanochemical reaction between $NaBH_4$ and $ZnCl_2$, according to the stoichiometric reaction as reported by [46]

$$2NaBH_4 + ZnCl_2 \longrightarrow Zn(BH_4)_2 + 2NaCl \qquad (5.2)$$

5.3.1 Undoped $Zn(BH_4)_2$ analysis

Figure 5.26 represents the X-ray diffraction pattern of the complex mixture ($2NaBH_4+ZnCl_2$) mechanically milled under N_2 for different time durations (30 min, 2h, 4h and 8h). As it can be seen, there are NaCl peaks and small satellite peaks corresponding to Zn-complex hydride structure present in the material, results expected from the stoichiometric equation 5.2. The structure remains the same at the different milling durations except the full width at half maximum (FWHM) of the peaks decreases with increase of milling duration.

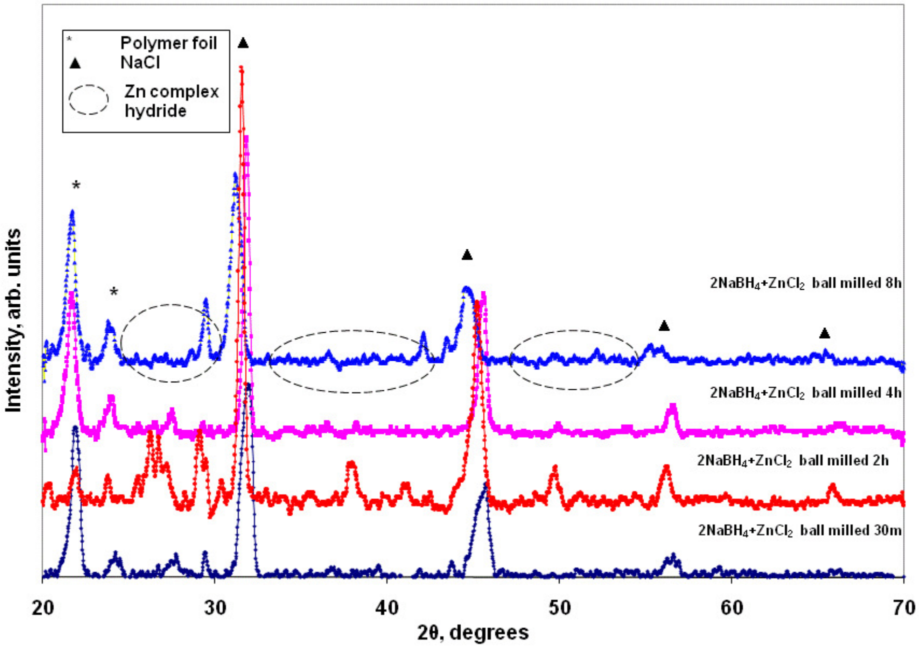

Figure 5.26 XRD patterns of $2NaBH_4$+$ZnCl_2$ mixture milled under N_2 ambient for different time durations

The gravimetric weight loss due to hydrogen decomposition of $NaBH_4$ and $Zn(BH_4)_2$ at different milling times is shown in Figure 5.27. The weight loss due to thermal decomposition of the $Zn(BH_4)_2$ ball milled with different time durations are given in Table 5.3

Table 5.3 Gravimetric weight loss with milling time of $Zn(BH_4)_2$

Ball milling time	Weight loss (%)
20 minutes	9.85
30 minutes	9.1
2 hours	6.674
4 hours	6.382
8 hours	5.22

It can be noted the hydrogen decomposition decreases with increasing milling durations; this is attributed to the releasing of hydrogen due to the collision between the powder and the balls. The result yields an optimum milling duration of 20 minutes for synthesizing $Zn(BH_4)_2$, a milling time below 20 minutes doesn’t complete the reaction (equation 5.2). The weight loss in $NaBH_4$ is almost zero due to its high thermal decomposition (~400 °C) [78,79]

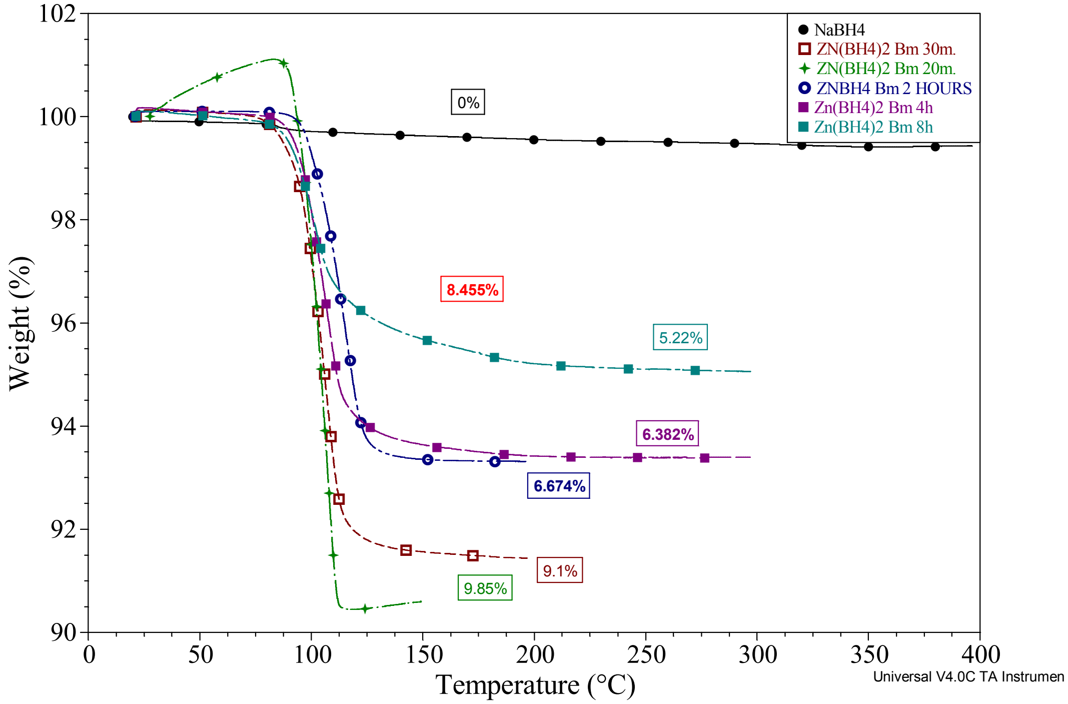

Figure 5.27 TGA profiles of $2NaBH_4+ZnCl_2$ at different milling times

In order to explore the degradation stability of as-synthesized $Zn(BH_4)_2+2NaCl$, the samples are stored inside a N_2 filled glove box for number of days. Figure 5.28 shows a comparison between the XRD profiles of $2NaBH_4 + ZnCl_2$ immediately after ball milled for 20 min. (orange line) and stored sample in N_2 ambient for 3 days (purple line).

It is clearly demonstrated that there is no change in the structure, relative intensities and number of complex hydride reflections even after three days. In the same graph the NaCl XRD is shown, the NaCl peaks at 32, 45.3, 57.1 and 62.52° are matched perfectly with the $2NaBH_4 + ZnCl_2$ ball milled sample, giving evidence of the formation of $Zn(BH_4)_2 + 2NaCl$.

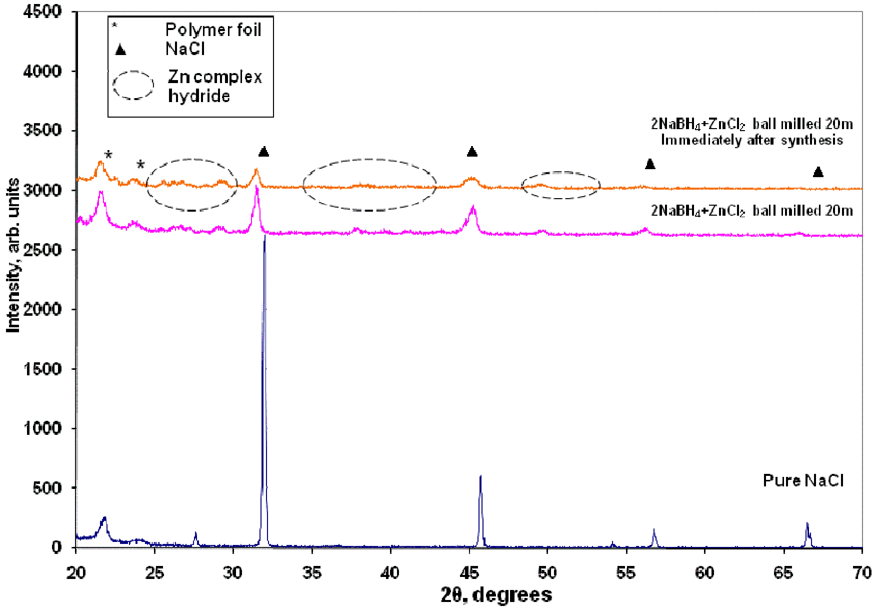

Figure 5.28 XRD profile of $2NaBH_4$+$ZnCl_2$ at different stages and pure NaCl

The FT-IR spectra of $Zn(BH_4)_2$+NaCl has been plotted together with $ZnCl_2$, $NaBH_4$, pure NaCl and is shown in Figure 5.29. As the NaCl shows a 0% flat transmission, the FT-IR spectra of the $Zn(BH_4)_2$ + NaCl should represent the spectra of $Zn(BH_4)_2$ alone. The characteristic Zn–Cl stretching appears at 1603 cm^{-1}. The ionic structure of $NaBH_4$ exhibits three bands in the infrared spectrum, a B–H stretching at 2200–2400 cm^{-1}, a Na-H stretching at 1427-1460 cm^{-1}, and a BH_2 bending at 1108 cm^{-1} [46]. In $Zn(BH_4)_2$ spectra, a band from B–H stretching between 2089 and 2451 cm^{-1}, a

Zn–H stretching at 1404 cm^{-1}, and a BH_2 deformation at 1115 cm^{-1} are detected, which are typical bands observed in Zinc borohydride [46]. The FT-IR result also indicates that $Zn(BH_4)_2$ was indeed formed by mechanochemical reaction for 20 minutes. Another investigation pertaining to degradation stability analysis was carried out in the FT-IR (Figure 5.30), the spectra of the sample immediately ball milled was compared with the sample after 3 days of being in a N_2 atmosphere at room temperature, showing no change in the bonding band stretching of the samples and giving evidence again of a very stable material and complementary with results of XRD profiles (Figure 5.28).

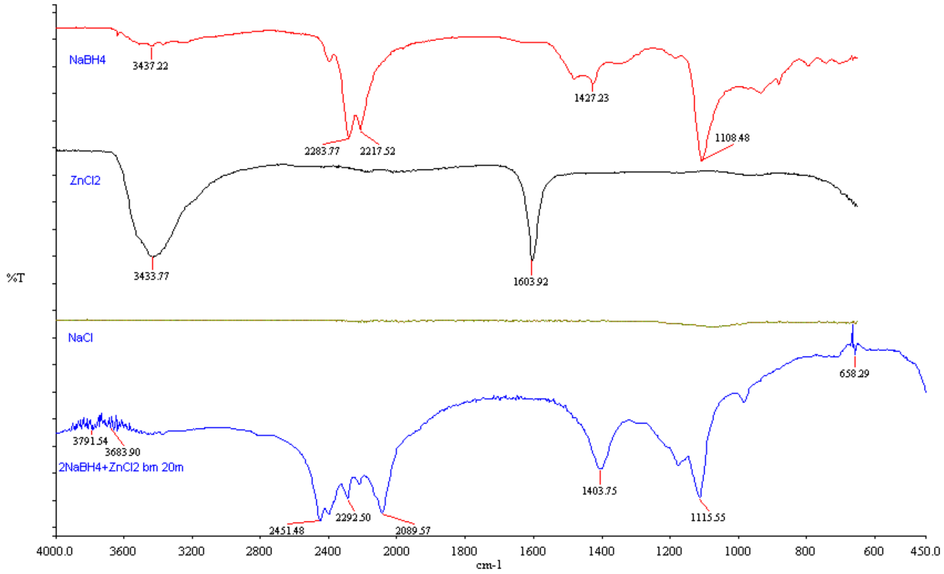

Figure 5.29 FTIR spectra of $NaBH_4$, $ZnCl_2$, NaCl, $2NaBH_4$+$ZnCl_2$ ball milled mixture

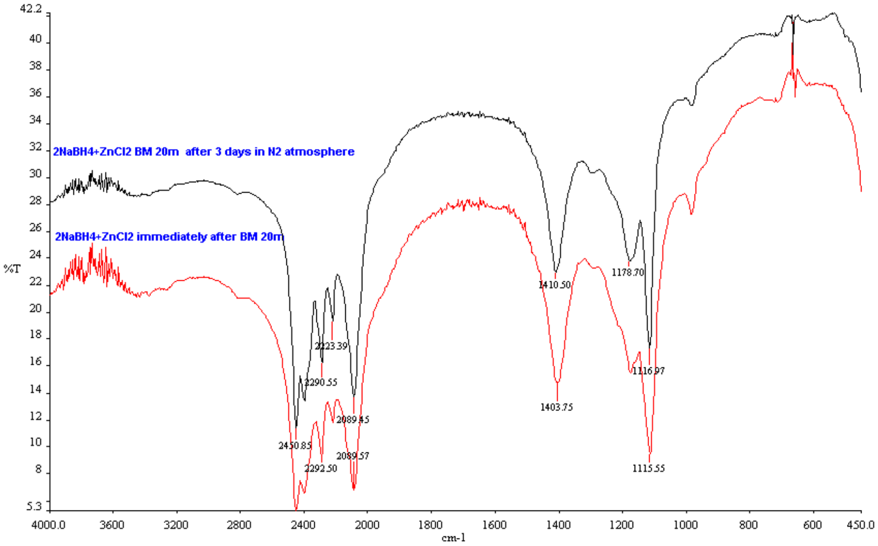

Figure 5.30 FTIR spectra of $2NaBH_4$+$ZnCl_2$ ball milled mixture immediately loaded and after 3 days

The purification process was performed to extract NaCl from the result mixture under nitrogen/vacuum Schlenk manifold technique, using dry tetrahydrofuran (THF) as obtained from the solvent purification system. After stirring overnight the mixture was filtered, the liquid phase was removed by canulating with a double-ended needle and THF was removed under reduced pressure, a white powder-like material was obtained with moderate yield and characterized by XRD (Figure 5.31). All the peaks in the extracted sample match perfectly with the peaks observed in a pure sample of NaCl, meaning that a successful separation/extraction was carried out.

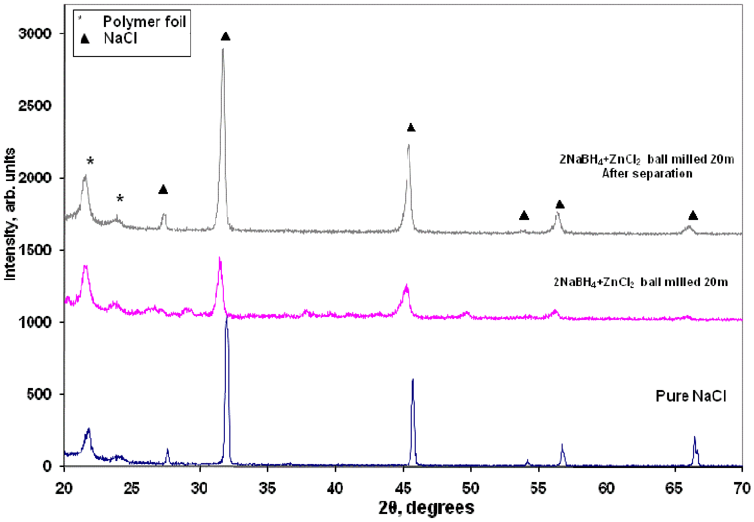

Figure 5.31 XRD pattern of $2NaBH_4+ZnCl_2$ mixture before and after purification

This same extracted sample is analyzed by the Energy Dispersive Spectroscopy (EDS) technique (Figure 5.32). As Figure 5.32 shows, the sodium and chlorine peaks are present which again confirms and conclude the XRD results. Other peaks such Carbon and Oxygen are due to the tape used for hold the powder and to the oxidation of the sample when it was loaded, respectively.

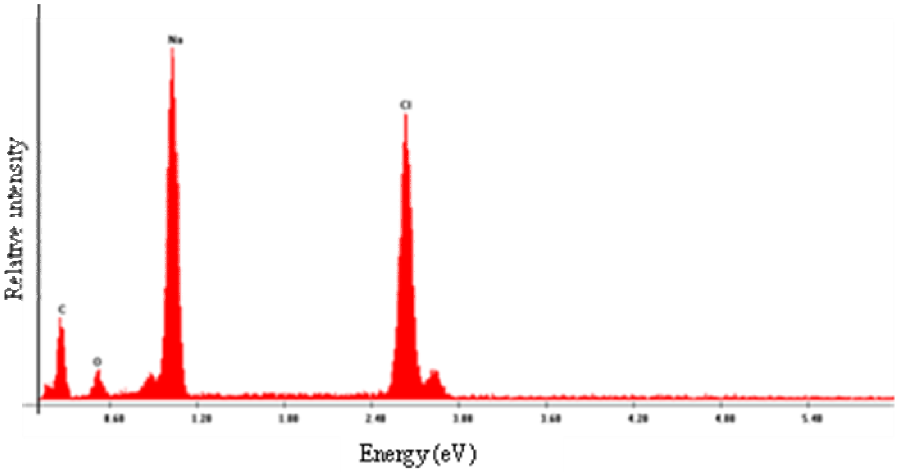

Figure 5.32 EDS profile of the extracted sample of $Zn(BH_4)_2+2NaCl$ after purification

The surface morphology of the as-milled $Zn(BH_4)_2$+2NaCl and 1RH-DH (Rehydrpgenation-Dehydrogenation) cycle sample is shown in Figure 5.33. The as-milled compound shows nanoclusters of complex hydride islands throughout the surface. The microstructure of the sample is highly porous and different contrast evidences the presence of unreacted NaCl byproducts on the surface. On the other hand the hydrogenated samples exhibit the uniform particle shapes and homogeneous structure.

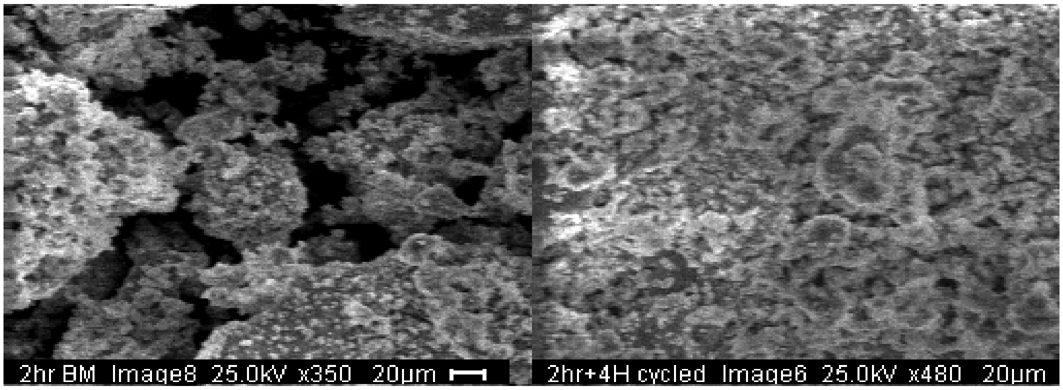

Figure 5.33 SEM of $Zn(BH_4)_2$+2NaCl mixture before and after hydrogenation

5.3.2 Doped $Zn(BH_4)_2$ analysis

As mentioned in chapter 3, a way to alter the surface and the bulk properties of the metal hydride is by introducing other element(s), many diverse elements have been investigated as possible catalysts to accelerate adsorption and desorption of hydrogen in borohydrides, however no reports are available for the catalytic doping of complex hydride $Zn(BH_4)_2$. In the present investigation catalyst dopants such as $TiCl_3$, TiF_3, nano Ni, nano Fe, Ti, nano Ti, Zn and MgH_2 are used in order to lower the decomposition temperature of $Zn(BH_4)_2$ in the range of 50-100 °C, without a significant reduction in the hydrogen content per total weigh, for getting a practical compound for on-board hydrogen storage applications.

The XRD profiles shown in Figure 5.34 correspond to the mixture of $2NaBH_4+ZnCl_2$ +Xmol%$TiCl_3$ (X=0.5, 1.0, 1.5, 2.5) ball milled under an ambient of N_2 gas for 20 minutes. The presence of NaCl and $Zn(BH_4)_2$ remain the same at the different concentrations and no traces of $TiCl_3$ was found. The simultaneous TGA and DSC patterns for the undoped and $TiCl_3$ doped samples are shown in Figure 5.35. The DSC analysis shows for the undoped $Zn(BH_4)_2$ there is an endothermic peak identified as a melting transition peak [46] at 93 °C, the same endothermic peak appears at the same temperature for the doped samples, meaning that the transition phase didn't change with the dopants. The TGA analysis shows a starting decomposition point for the doped and undoped samples at 93 °C, the same temperature in which the melting transition occurs. A complete weight loss due to thermal decomposition for the Xmol% doping complex hydride is given in Table 5.4

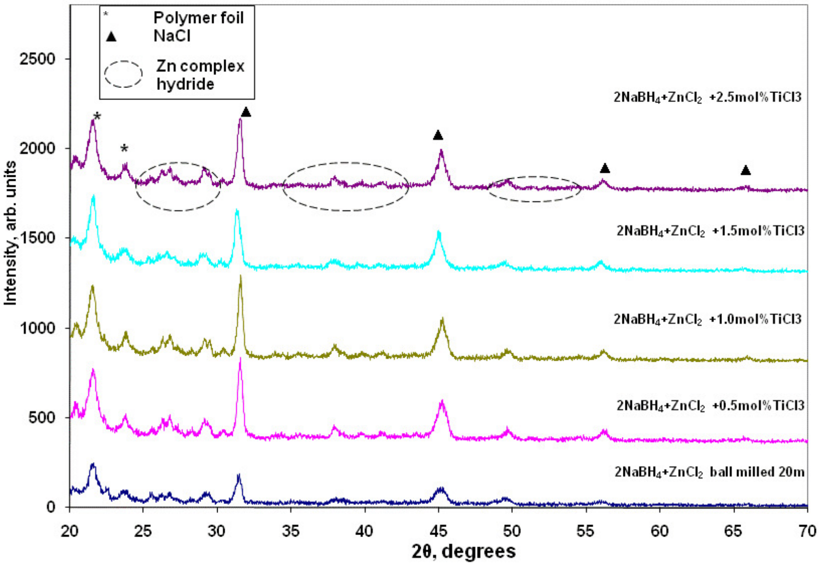

Figure 5.34 XRD patterns of $2NaBH_4+ZnCl_2$, doped with Xmol% of $TiCl_3$

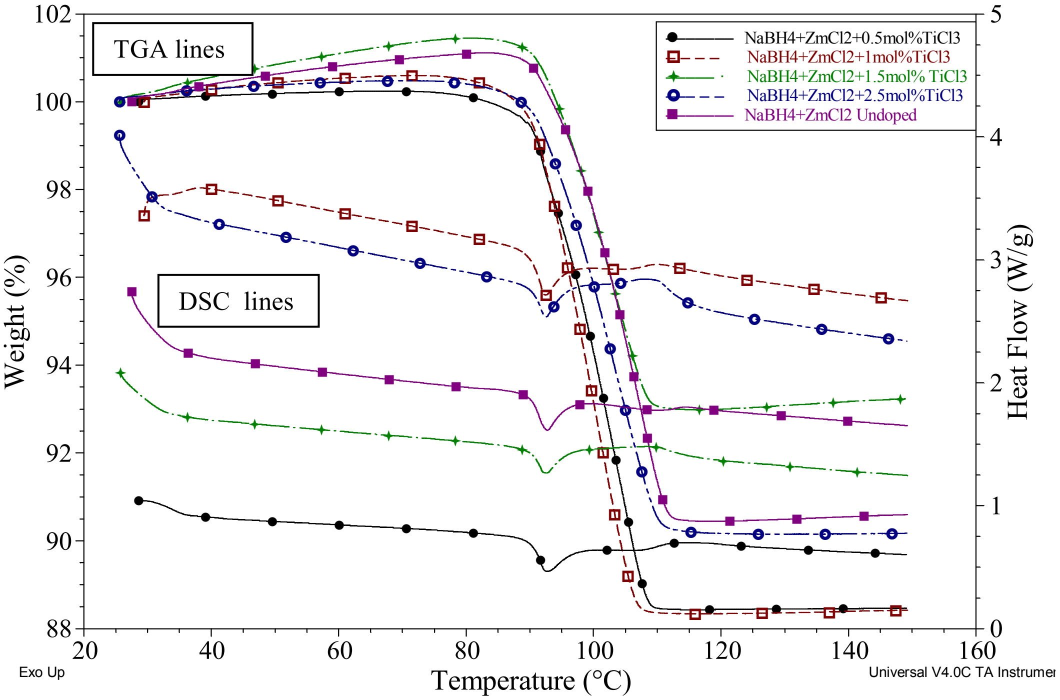

Figure 5.35 TGA and DSC profiles of $2NaBH_4+ZnCl_2$ doped with Xmol% $TiCl_3$

Table 5.4 Gravimetric weight loss, decomposition temperature and amount of catalyst doping for the $Zn(BH_4)_2$ and undoped sample

Sample	Decomposition T (ºC)	Weight loss (%)
Undoped $Zn(BH_4)_2$	112	9.5
0.5 mol% $TiCl_3$ doped	109	11.5
1.0 mol% $TiCl_3$ doped	107	11.6
1.5 mol% $TiCl_3$ doped	111	7.0
2.5 mol% $TiCl_3$ doped	111	9.8

As can be seen, an improvement of 5 °C in the completeness of the decomposition is achieved when $Zn(BH_4)_2$ is doped with 1.0 mol% of $TiCl_3$, additionally 2% more of weight loss is achieved by adding this dopant.

Figure 5.36 shows the XRD profiles corresponding to the mixture of $2NaBH_4+ZnCl_2$ +Xmol%TiF_3 (X=0.7, 1.4, 2.1) ball milled under an ambient of N_2 gas for 20 minutes. As the XRD patterns for $TiCl_3$ samples shown above, the presence of NaCl and $Zn(BH_4)_2$ remain the same at the different concentrations and no presence of $TiF3_3$ was found. The TGA and DSC patterns for the undoped and TiF_3 doped samples are shown in Figure 5.37. Additionally a sample of $2NaBH_4+ZnCl_2$ was ball milled for 15 minutes and 1.4 mol% of TiF3 was then added, and ball milled together for other 15 minutes; the TGA and DSC analysis is also shown in Figure 5.37

The DSC analysis shows the same melting transition peak [46] at 93°C for the undoped and doped samples. The TGA analysis shows the following relation: a complete weight loss of 9.5% take place at 112 °C for undoped $Zn(BH_4)_2$; with a doping of 0.7 mol% of TiF_3 a complete weight loss of 12% is reached at 107 °C, for a doping of 1.4 mol% a loss of 12.5% is achieved at 105 °C and a doping of 2.1 mol% produces a weight loss of 11.2% at 108 °C. For the experiment of adding 1.4 mol% TiF3 after ball milling, the weight loss is 8.8% and is complete at 150 °C, meaning that a better hydride material is formed when $2NaBH_4$ and $ZnCl_2$ is ball milled together with the catalyst. A difference in temperature of 7 °C in the entire decomposition of the sample is achieved when $Zn(BH_4)_2$ is doped with 1.4 mol% of TiF_3 and also an increment in the weight loss of 3wt%

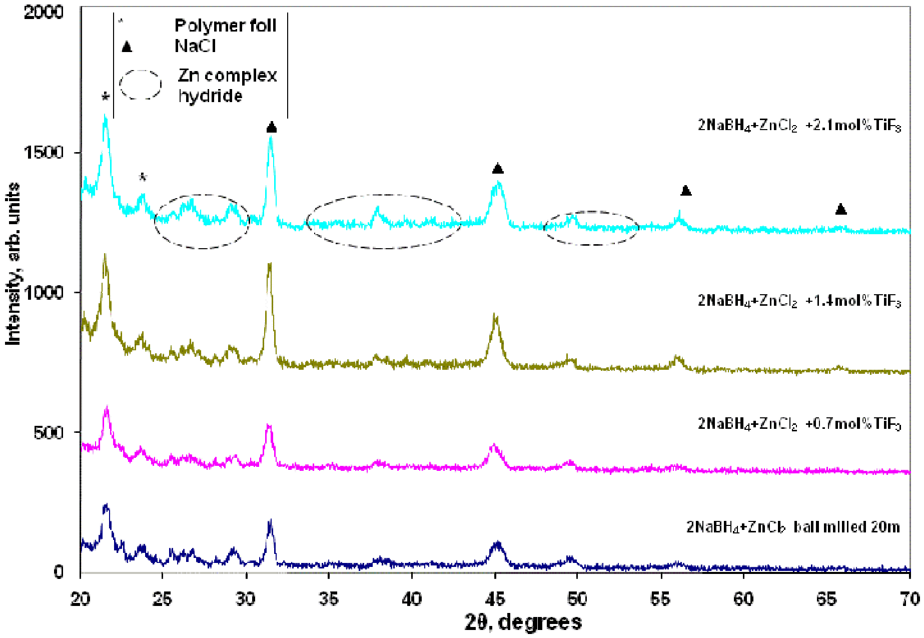

Figure 5.36 XRD patterns of $2NaBH_4$+$ZnCl_2$, doped with Xmol% of TiF_3

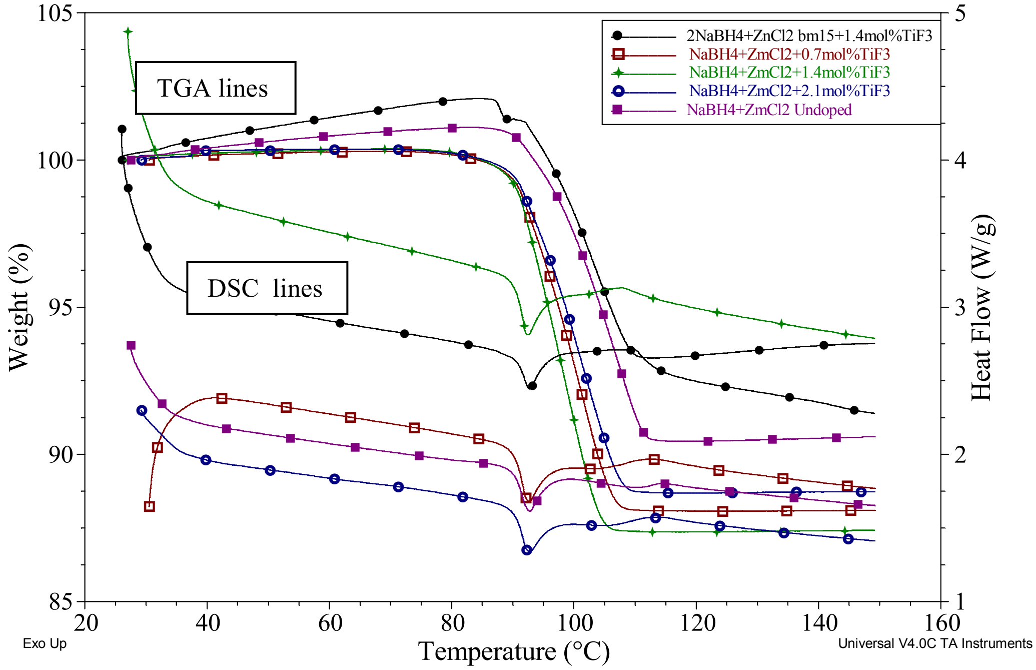

Figure 5.37 TGA and DSC profiles of $2NaBH_4$+$ZnCl_2$ doped with Xmol% TiF_3

The XRD profiles shown in Figure 5.38 correspond to the mixture of $2NaBH_4$+$ZnCl_2$ +Xmol% nanoNi (X=0.5, 1.0, 1.5, 2.0, 2.5) ball milled under an ambient of N_2 gas for 20 minutes, the nanoNi dopant was procured from Quantum Sphere. The presence of NaCl and $Zn(BH_4)_2$ remains the same at the different concentrations and no presence of Ni was found, except for the 2.5 mol% XRD pattern, where a small peak at 43.8° is formed; this peak is attributed to the presence of the Ni dopant, since concentration at 2.5 mol% is comparable to the concentration of precursor compounds ($2NaBH_4$, $ZnCl_2$). In this graph is also shown the XRD profile for the sample doped with 1.5 mol% nanoNi manufactured by Sigma Aldrich; no significant difference compared with the other dopants is observed.

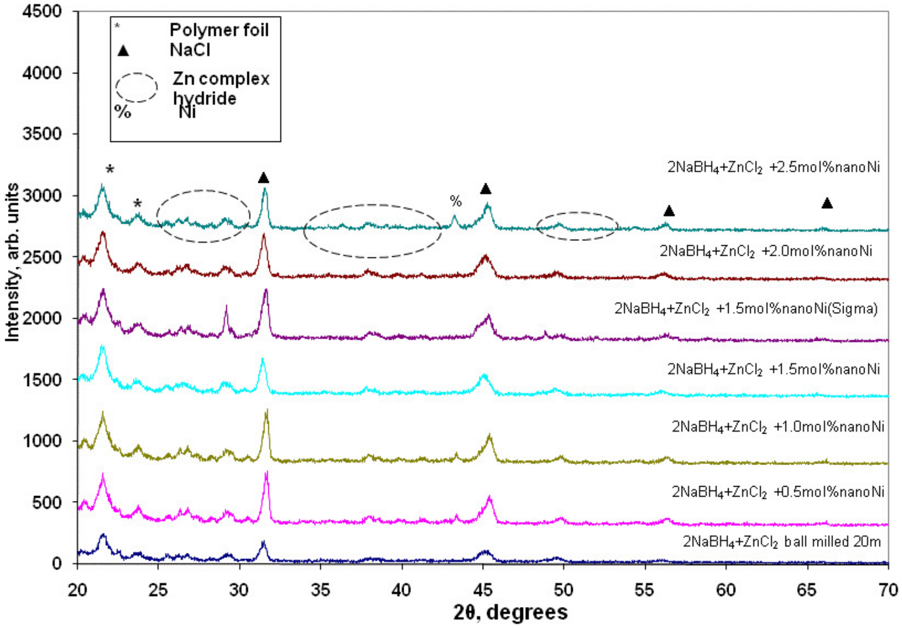

Figure 5.38 XRD patterns of $2NaBH_4$+$ZnCl_2$, doped with Xmol% of nano Ni

The TGA and DSC patterns for the undoped and nanoNi doped samples are given in Figure 5.39. As it can be seen, the decomposition occurs before the melting transition, a feature that is important when the gas analysis (GC/MS) will be done. The DSC/TGA analysis shows an alteration and advancing in the melting transition and thermal decomposition which has been tabulated in Table 5.5. A complete weight loss in relation with dopant concentrations and decomposition temperature is also tabulated in the same Table. For further comparison and characterization, the doping of 1.5 mol% nanoNi was chosen for having the best characteristics compared with the undoped $Zn(BH_4)_2$ sample: reduction in the temperature of the entire decomposition, from 112 °C of the undoped to 91 °C of the doped sample; no alteration in the structure (XRD), a weight loss of 10% and a separation between the starting decomposition temperature and the melting transition, from a difference of 0 °C in the undoped sample to 20 °C in the doped sample.

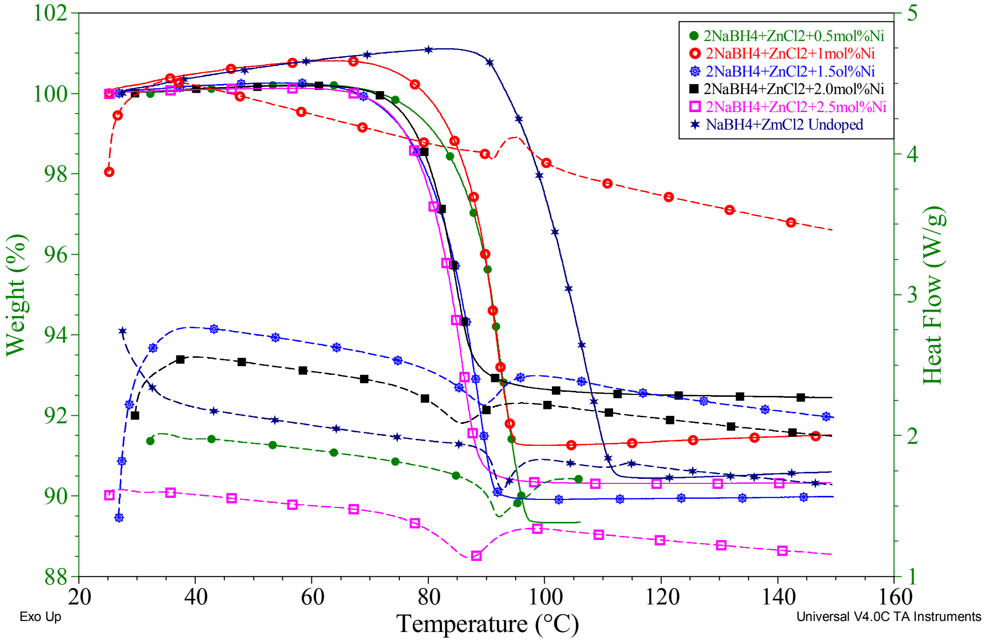

Figure 5.39 TGA and DSC profiles of $2NaBH_4$+$ZnCl_2$ doped with Xmol% Ni

Table 5.5 DSC and TGA analysis of undoped and nanoNi doped $Zn(BH_4)_2$

Xmol% nanoNi doped $Zn(BH_4)_2$	DSC melting transition (ºC)	TGA starting decomposition(ºC)	TGA complete decomposition (ºC)	Weight loss (%)
Undoped	93	100	115	9.5
0.5	93	75	98	10.5
1.0	92	80	94	8.5
1.5	90	70	91	10.0
2.0	86	72	92	7.4
2.5	86	70	90	9.5

Figure 5.40 shows the XRD profiles corresponding to the mixture of $2NaBH_4$+$ZnCl_2$+Xmol%Ti (X=1.0, 1.5, 2.0) and $2NaBH_4$+$ZnCl_2$+Xmol% nanoZn (X=1.0, 2.0) ball milled separately under an ambient of N_2 gas for 20 minutes.

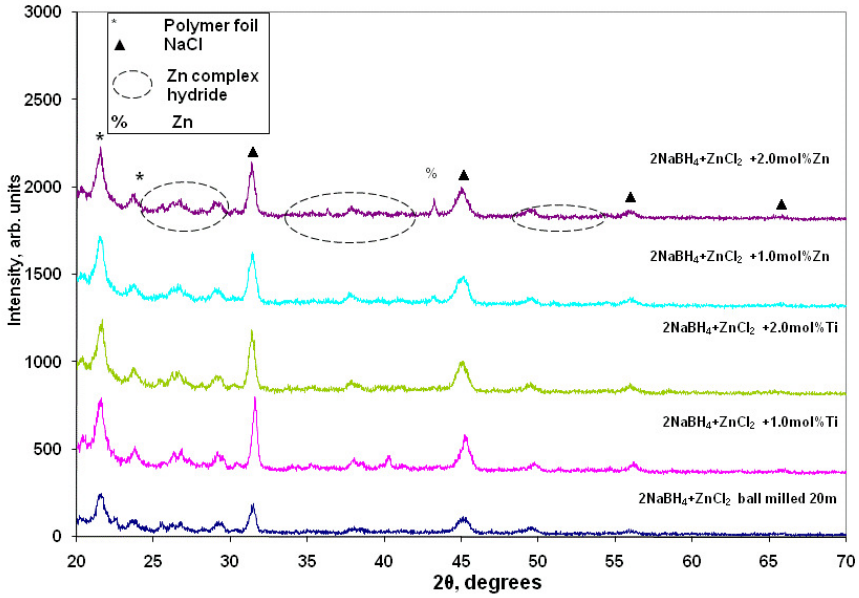

Figure 5.40 XRD patterns of $2NaBH_4$+$ZnCl_2$, doped with Xmol% of Zn and Ti

As the XRD patterns for Ti doped samples show, the presence of NaCl and $Zn(BH_4)_2$ remains the same at the different concentrations and no presence of Ti was found. On the other hand, The XRD patterns for Zn doped samples (1.0, 2.0 mol%), show a peak at 43 °, due to the presence of Zn. The TGA and DSC patterns for the undoped and doped samples (Ti and Zn) are shown in Figure 5.41. The DSC analysis shows the same melting transition peak at 93 °C for the undoped and doped samples. The TGA analysis shows a starting decomposition point for the doped samples at 90 °C for 1.0 mol% Ti, 87 °C for 1.5 mol %Ti, 88 °C for 2.0 mol% Ti and 87 °C for 1.0 and 2.0 mol% Zn. Although the decomposition occurs before the melting transition, it is not good enough as the sample doped with nanoNi. A complete weight loss of 8.75% take place at 105 °C for 1.0 mol% Ti doped $Zn(BH_4)_2$; with a doping of 1.5 mol% of nano Ti a complete weight loss of 15% is reached at 130 °C, for a doping of 2.0 mol% Ti a loss of 11% is achieved at 106 °C, a doping of 1.0 mol% Zn produces a weight loss 12% at 109 °C and for 2.0 mol% of nano Zn a complete weight loss of 11.5% is reached at 109 °C. Even though there is a significant increment in the weight losses, the temperature of decomposition completeness is still high compared with the nanoNi doping.

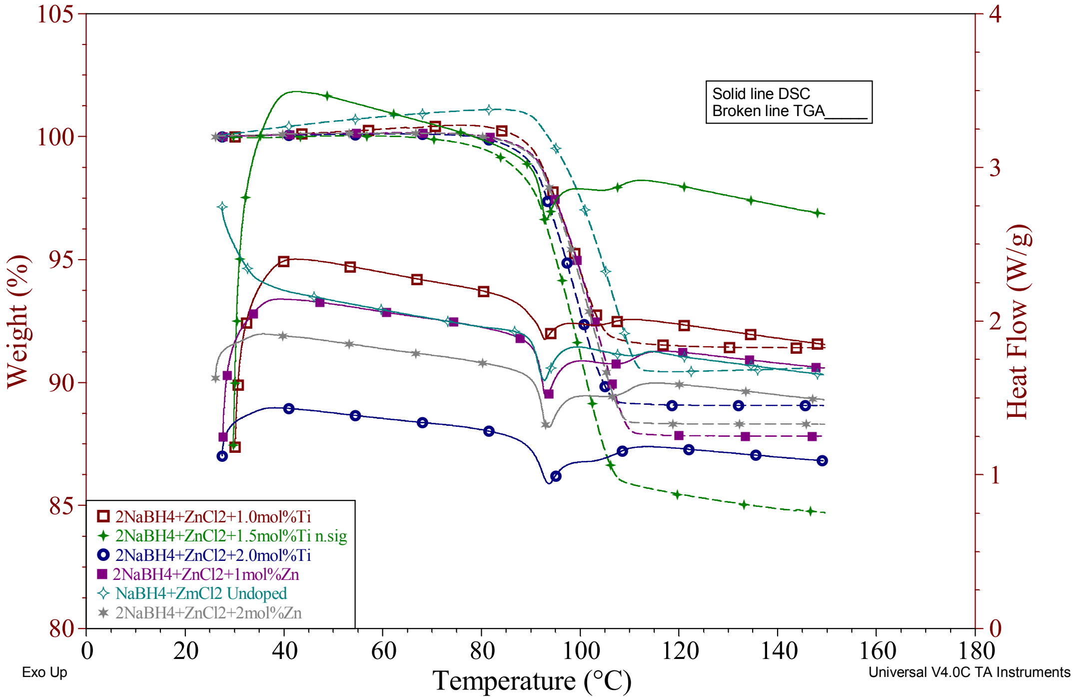

Figure 5.41 TGA and DSC profiles of $2NaBH_4$+$ZnCl_2$ doped with Xmol% of Zn and Ti

The XRD profiles shown in Figure 5.42 correspond to the mixture of $2NaBH_4$+$ZnCl_2$ doped with 1.5 mol% nanoFe, 1.5 mol% nanoTi and 1.5 mol% nanoNi + 2%weight MgH_2 ball milled separately under an ambient of N_2 gas for 20 minutes. The presence of NaCl and $Zn(BH_4)_2$ remain the same at the different concentrations and no presence of dopant was found, except for the MgH_2. A small peak at 43.9 ° is formed for the MgH_2 doped sample; this peak is attributed to the presence of MgH_2 dopant.

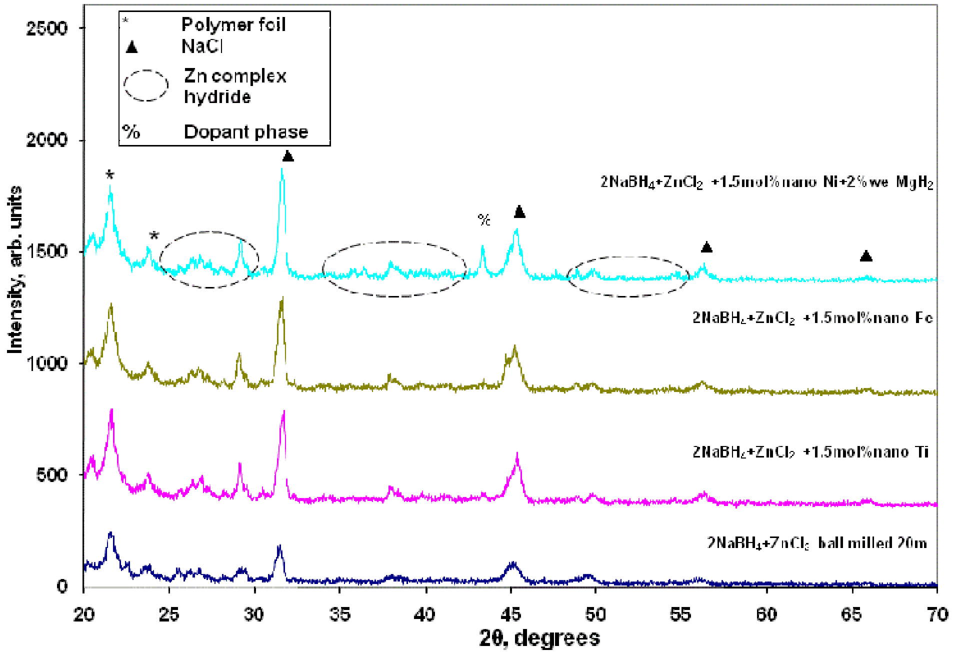

Figure 5.42 XRD patterns of $2NaBH_4$+$ZnCl_2$, doped with 1.5mol% of nanoFe, nanoTi and nanoNi+ 2%weight MgH_2, bm 20m

The TGA and DSC patterns for the undoped and doped samples are shown in Figure 5.43. The DSC analysis shows a significant alteration in the melting transition for the nano Ni (Quantum Spheres) doped samples. As it can be seen in the TGA analysis, the fastest decomposition occurs when the sample is doped with 1.5 mol% nanoNi. Although Fe, Ti and sigma nano Ni show some improvement in the decomposition, 1.5mol% concentration of nano nickel manufactured by QS is still the best performance. The dopant. MgH_2 didn't show any improvement in the DSC and TGA result.

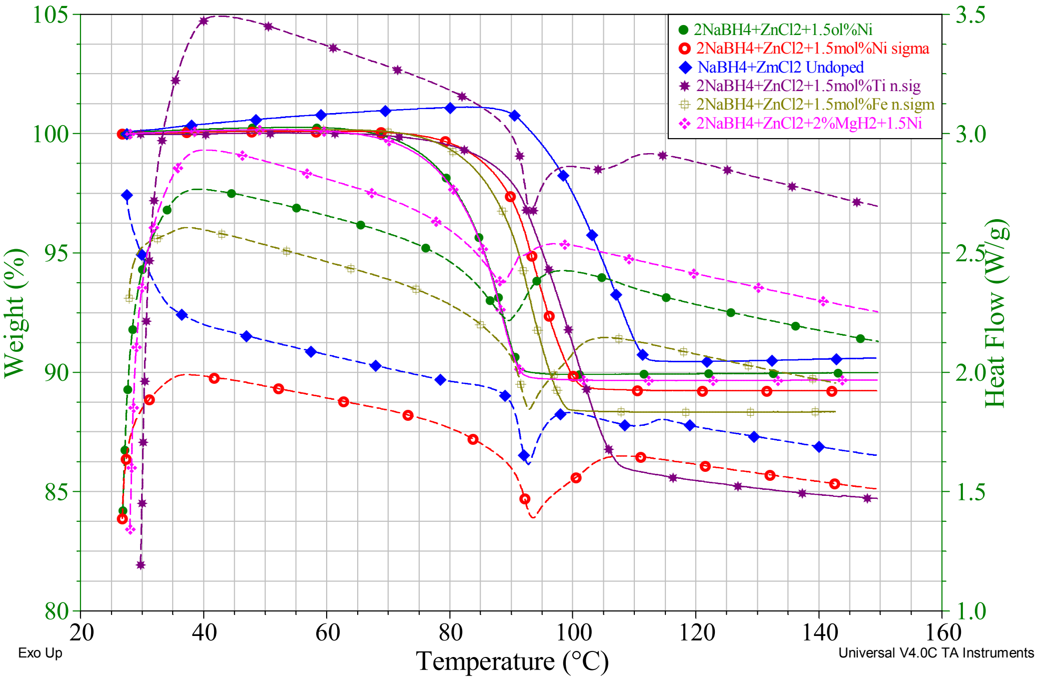

Figure 5.43 TGA(solid line) and DSC(broken line) profiles of $2NaBH_4$+$ZnCl_2$ doped with 1.5mol% concentration of various dopants

The FT-IR spectra shown in Figure 5.44 correspond to the mixture of the undoped $2NaBH_4$+$ZnCl_2$ and doped with 1.5mol% X (X = nanoFe, $TiCl_3$, TiF_3, nanoNi QS). As it can be noted, the FT-IR profile for the different doped samples is almost the same as the undoped sample, showing the presence of a band from B–H stretching between 2000 and 2500 cm^{-1}, a Zn–H stretching around 1450 cm^{-1}, and a BH_2 deformation around 1100 cm^{-1}, these bands confirm that no change in the bonding environment was made by adding dopants.

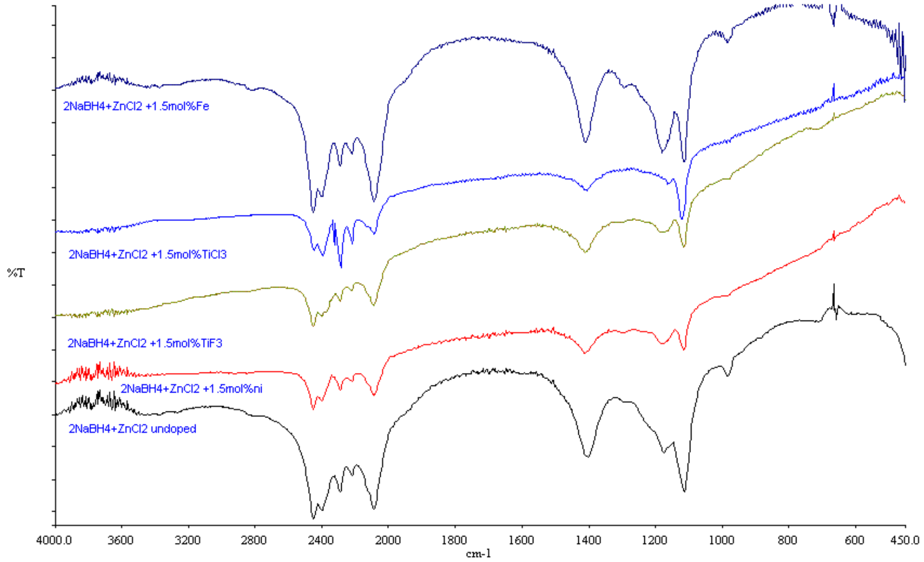

Figure 5.44 FTIR spectra of $2NaBH_4$+$ZnCl_2$ ball milled mixture doped and undoped

5.3.3 Undoped and doped $Zn(BH_4)_2$ decomposition analysis

The XRD profiles shown in Figure 5.45 correspond to the mixture of $2NaBH_4$+$ZnCl_2$ ball milled, before and after desorption cycle, NaCl pure sample and the ball milled sample of $2NaBH_4$+$ZnCl_2$+1.5mol% nanoNi after being exposed to desorption in the PCT apparatus. As it can be seen, after desorption, the remaining product is Na, Cl and Zn, for both doped and undoped samples. The remaining products after PCT are confirmed by using the EDS (Figure 5.46). After removing the NaCl product, can be concluded that $Zn(BH_4)_2$ thermally decomposes in Zn and some other gases (H_2, Borane family) desorbed in the PCT, according to the GC-MS analysis done and as is reported by [46]. The total decomposition is shown in equation 5.3

$$Zn(BH_4)_2 \longrightarrow Zn + B_2H_6 + H_2 \qquad (5.3)$$

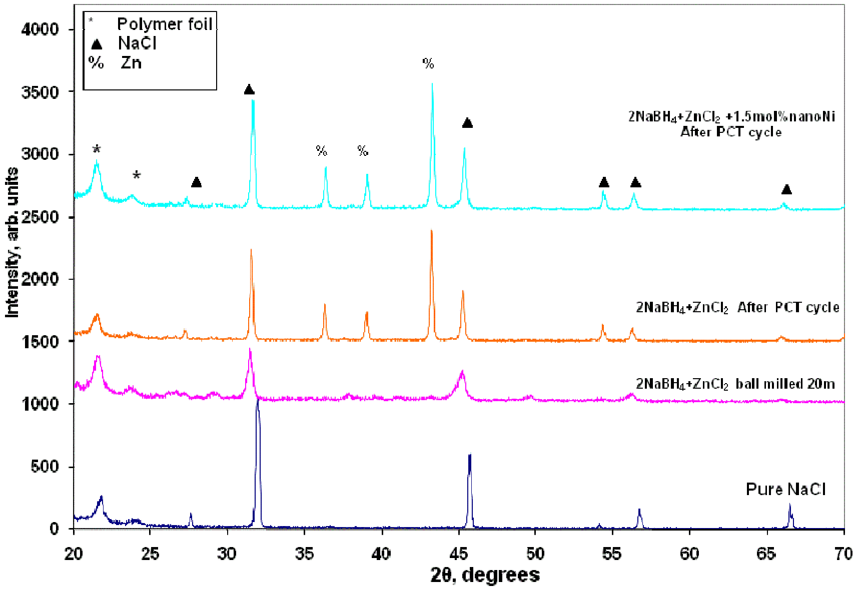

Figure 5.45 XRD patterns of doped/undoped $2NaBH_4+ZnCl_2$ mixture before and after PCT cycle

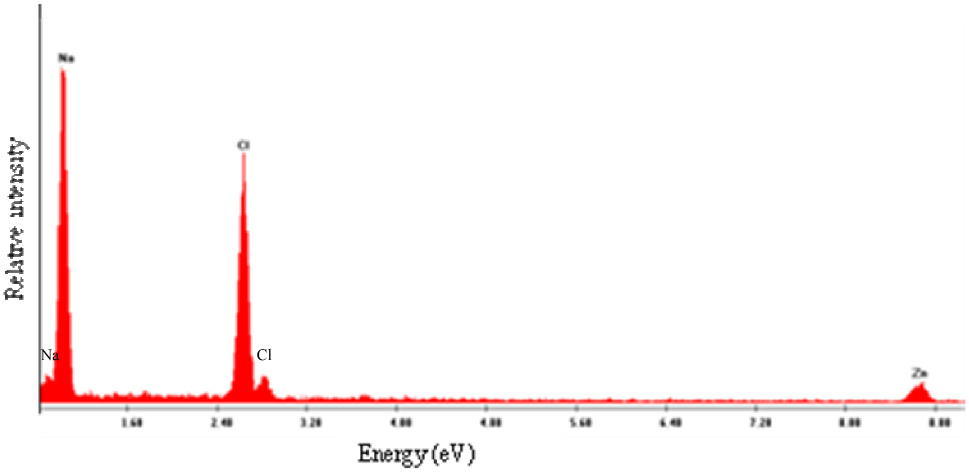

Figure 5.46 EDS profile of $Zn(BH_4)_2$+2NaCl after PCT cycle

5.3.3.1 Undoped and doped $Zn(BH_4)_2$ TPD analysis

Figure 5.47 shows TPD curves of undoped $Zn(BH_4)_2$ and the same complex hydride doped with 1.5 mol% nanoNi. As TCD signal is proportional to the quantity of molecules desorbed as the temperature increases, it can be seen in the graph that for the doped sample, the decomposition starts early (~ 40 °C) and for the undoped sample starts at 65 °C, 25 °C of difference, results very close to the TGA analysis (21°C). Other important feature of this graph is that for the doped sample, the signal becomes stronger compared with the undoped sample in the range of 40 to 120 °C, meaning that more decomposition gases are coming out from the sample.

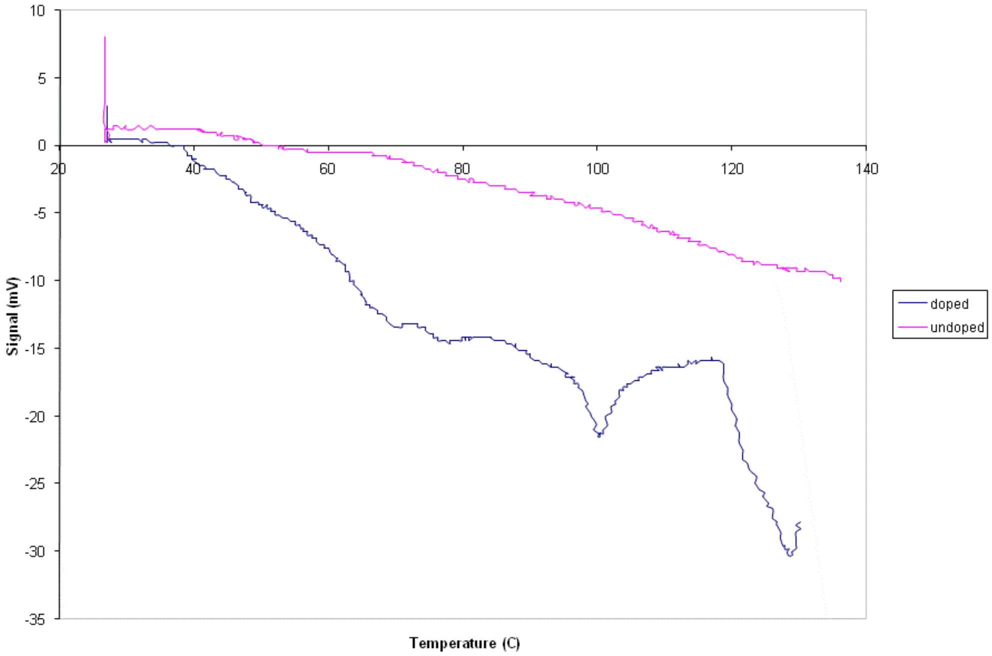

Figure 5.47 TPD patterns of doped and undoped $Zn(BH_4)_2$

In Figure 5.48 is shown a comparison among the TPD profiles of the doped $Zn(BH_4)_2$, before and after the first and second hydrogenation. The purple line indicates the TPD profile of the initial doped sample at a ramping temperature between 20 to 130 °C; a reduction in the signal intensity is shown in the blue line and a zero desorption is exposed in the green line. As the TPD analysis confirm, no reversibility of the doped $Zn(BH_4)_2$ was found, this lack of reversibility is attributed to evolution of borane gases.

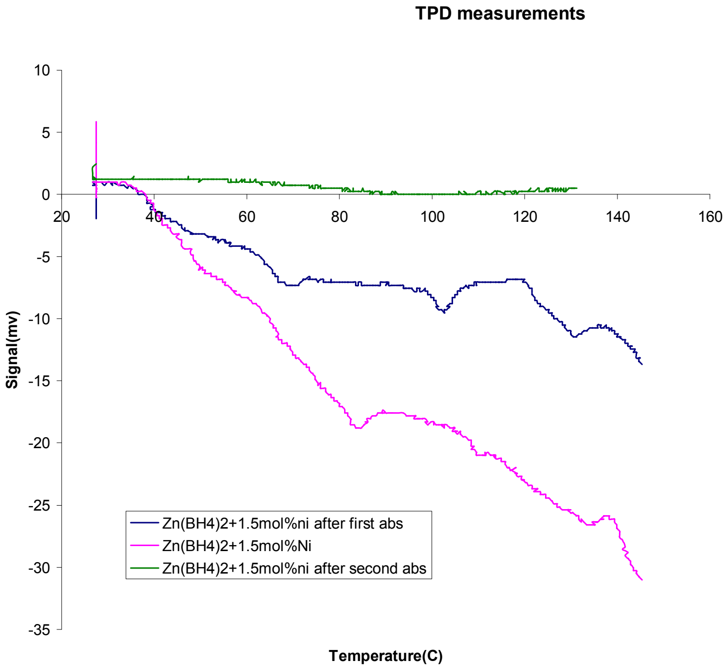

Figure 5.48 TPD patterns of doped $Zn(BH_4)_2$ before and after hydrogenation

5.3.3.2 Undoped and doped $Zn(BH_4)_2$ GC/MS analysis

Figure 5.49 and Figure 5.50 confirms the presence of borane family gases as it was stated before, this boron decomposition destroys the reversibility of $Zn(BH_4)_2$ due to the lack of boron to complete the reaction when the remaining product is hydrogenated. Although the borane is detected, mass spectrometer doesn't have the capability to detect hydrogen gas due to the electronic configuration. In Figure 5.49 is illustrated the GC/MS analysis of undoped $Zn(BH_4)_2$ at 110 °C and 120 °C, tetraborane and pentaborane presence increases when the temperature goes from 110 °C 120 °C and a hexaborane peak appears, when the sample is heated at 120 °C.

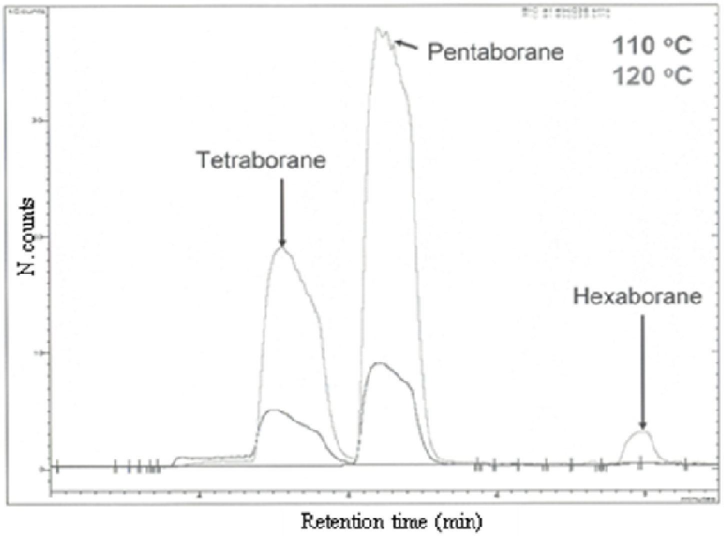

Figure 5.49 GC/MS analysis of undoped $Zn(BH_4)_2$ at 110 °C and 120 °C

Not only diborane is thermally decomposed from $Zn(BH_4)_2$ as reported by [46], other borane families are present, as show in the GC/MS analysis. The same feature is seen when the sample is doped with 1.5 mol% nanoNi (Figure 5.50), as the temperature increases, the borane peaks start growing.

An important aspect is noted when the GC/MS profile of the $Zn(BH_4)_2$ sample is compared with the profile of the Ni-doped sample (Figure 5.51). When the sample is doped, the borane gases are reduced almost 20 times compared with the undoped sample, confirming that most of hydrogen is decompose by the sample. Although borane has been reduced, boron is getting lost and therefore no reversibility is found in the doped sample.

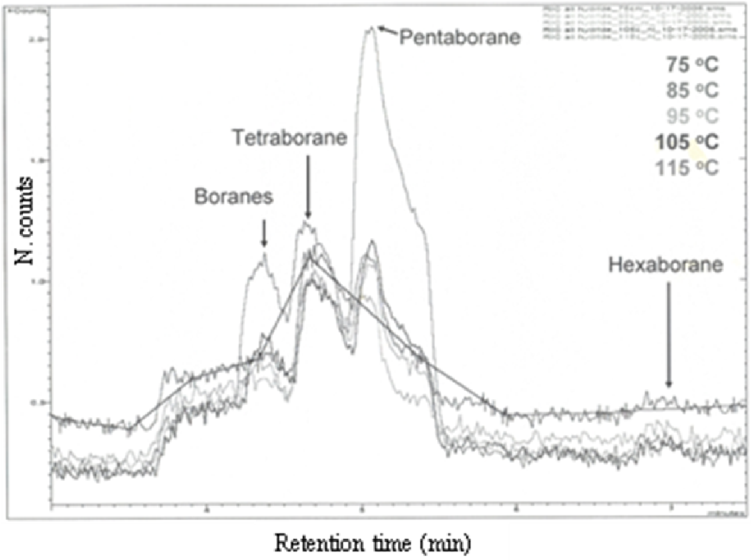

Figure 5.50 GC/MS analysis of Ni-doped $Zn(BH_4)_2$ from 75 °C to 115 °C

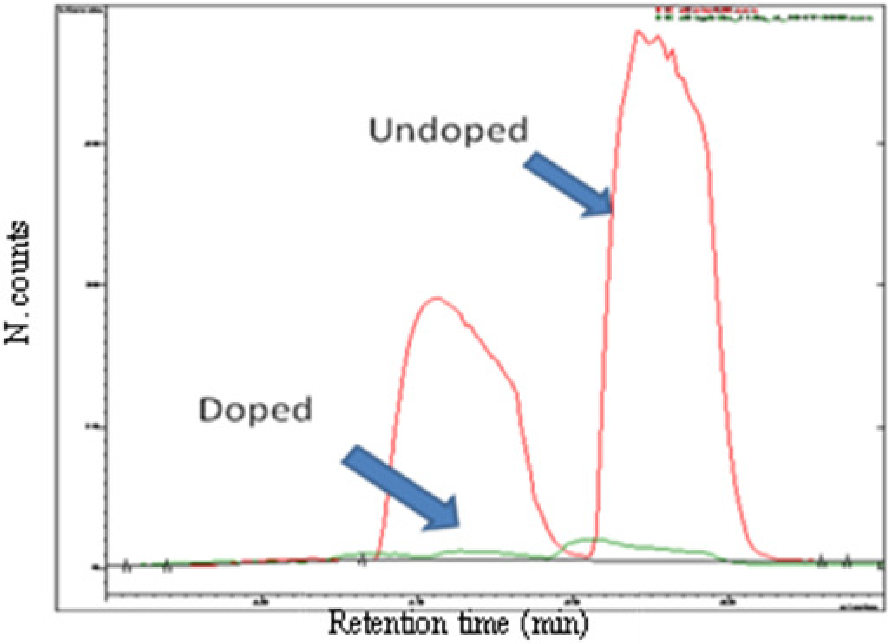

Figure 5.51 Comparison GC/MS analysis of Ni-doped and undoped $Zn(BH_4)_2$

CHAPTER 6

CONCLUSIONS AND RECOMMENDATIONS

6.1 Conclusions and recommendations for on-board hydrogen application materials ($Zn(BH_4)_2$)

The complex hydride $Zn(BH_4)_2$ has been synthesized by an inexpensive mechanochemical process involving ball milling of stoicheometry of $NaBH_4$ and $ZnCl_2$ under inert ambient at room temperature. Milling duration of 20 minutes was chosen since at this time length a complete reaction is reached and a high decomposition weight loss from $Zn(BH_4)_2$ is shown by the TGA.

The present investigation also attempted to study the catalytic behavior in $Zn(BH_4)_2$. Some catalyst dopants such as $TiCl_3$, TiF_3, nano Ni, nano Fe, Ti, nano Ti, Zn and MgH_2 were used in order to lower the decomposition temperature of $Zn(BH_4)_2$ in the range of 50-100 °C, without a significant reduction in the hydrogen content per total weigh, for getting a practical compound for on-board hydrogen storage applications. Nano nickel manufactured by Quantum spheres in a concentration of 1.5 mol% was confirmed as the best performance dopant for having the best characteristics compared with the undoped $Zn(BH_4)_2$ sample: reduction in the temperature of the entire decomposition, from 112 °C of the undoped to 91 °C of the doped sample; no alteration in the structure (XRD), a weight loss of 10% and a separation between the starting decomposition temperature and the melting transition, from a difference of 0 °C in the undoped sample to 20 °C in the doped sample.

Although $Zn(BH_4)_2$ was confirmed to decompose into various boranes (diborane, tetraborane, pentaborane, hexaborane) and hydrogen gas as well as Zn metal, the 1.5 mol% nanoNi doped sample shows a reduction of almost 20 times in the borane gas intensity and therefore an increment of hydrogen decomposition. The GC/MS result also gives the evidence of the lack of reversibility of both compounds, doped and undoped $Zn(BH_4)_2$, which is a critical point in on-board hydrogen storage applications.

Many possibilities for improvements could be pursued further by future work. A complete study of the decomposition gases of the 1.5 mol% nanoNi doped sample at different temperatures could be explored in order to determine the borane decomposition starting temperature; Some other nano catalysts could be investigated for making this compound completely reversible or a chemical method could be developed in order to trap the boron to complete the reaction when the remaining product is hydrogenated.

6.2 Conclusions and recommendations for hydrogen compression application materials ($ZrMn_2$, ZrNi)

Significant improvement in the hydrogen storage property (~ 26 times greater) was accomplished in the $ZrMn_2$ alloy. The annealing treatment was applied and the crystalline structure was recovered appreciably. Other important improvement shown in the XRD was reached when the $ZrMn_2$ sample was pelletized before the sintering action.

In ZrNi 1:1 an improvement in the kinetics was achieved when the sample was annealed for 10 hours at 1100 °C, the hydrogen is completely released after 0.8 hours at

375 and 350 °C compared with the slow kinetics (~3 hours) presented in the ball milled material, giving the evidence that the hydrogen absorption/desorption kinetics is influenced by the ball milling and sintering process.

Unlike $ZrMn_2$, ZrNi show comparatively better hydrogen absorption/desorption characteristics, they are still too low for a practical use. A recommendation for synthesizing and improving the hydrogen storage capacity of these metal hydrides is by arc-melting the single elements to form the specific alloy.

The best performance intermetallic alloy found from our experiments for the hydrogen compression applications was ZrNi 70/30. This alloy possesses several promises for this purpose, such as low cost of acquisition, no pretreatment is needed, good cyclic stability, respectable gravimetric density, low hysteresis, good hydriding/dehydriding kinetics and reasonable plateau pressures.

REFERENCES

[1] BP report (2006). “Statistical review of world energy 2006,” online posting, www.bp.com.

[2] Andreas Züttel (2004). “Hydrogen storage methods and materials,” University of Fribourg, Physics Department, Pérolles, CH-1700 Fribourg, Switzerland.

[3] Bulletin (2000), Magazin der Eidgenössischen Technischen Hochschule Zürich, pp. 276.

[4] McNicol BD, Rand DAJ, Williams KR. (2001). “Fuel cells for road transportation purposes—yes or no,” Journal of Power Sources, vol. 100, pp. 47–89.

[5] Jun Lu, Zhigang Zak Fang Hong Yong Sohn (2006). “A New Li-Al-N-H System for Reversible Hydrogen Storage,” J. Phys. Chem. B, 110, pp. 14236-14239.

[6] Viral Mehta, Joyce Smith (2003). “Review and analysis of PEM fuel cell design and manufacturing,” Journal of Power Sources, Vol. 114, Issue 1, pp. 32-53.

[7] Nick E. Tran, S.G. Lambrakos, M. Ashraf Imam (2006). “Analyses of hydrogen sorption kinetics and thermodynamics of magnesium–misch metal alloys,” Journal of Alloys and Compounds, vol. 407, pp. 240–248.

[8] Geoff Dutton (2002). “Hydrogen energy technology,” Tyndall Center for Climate Change Research, working Paper 17.

[9] Bellona report (2002). “Hydrogen technologies,” online posting, www.bellona.org.

[10] F. Schuth, B. Bogdanovic & M. Felderhoff (2004). “Light metal hydrides and complex hydrides for hydrogen storage,” Chem. Commun. 2249 – 2258.

[11] Li Zhou (2005). “Progress and problems in hydrogen storage methods,” Renewable and Sustainable Energy Reviews, vol. 9, pp. 395–408.

[12] Farnesi, M., Cozzani, V., Nicolella, C. and Zanelli, S. (2004). “Analysis and comparison of hydrogen storage systems”, Dipartimento di Ingegneria Chimica-Chimica Industriale-Scienza dei Materiali, Università di Pisa.

[13] Gary Chen, Samim Anghaie (2002). based on NASA/NIST databases, online posting, http://www.inspi.ufl.edu/ data/h_prop_package.html.

[14] Dillon, A.C., Jones, K.M., Bekkedahl, T.A., Kiang, C.H., Bethune, D.S., Heben, M.J. (1997). "Storage of hydrogen in single walled carbon nanotubes," Nature, vol. 386, pp. 377-9.

[15] U. Eberle, G. Arnold, R. von Helmolt (2006). "Hydrogen storage in metal–hydrogen systems and their derivatives," Journal of Power Sources, vol, 154, pp. 456–460.

[16] L. Kit Heung (2003). "Using Metal Hydride to Store Hydrogen," Fuel Cells 2003 - Third Annual BCC Conference Stamford, CT.

[17] J.H.N. van Vucht, F.A. Kuipers, H.C.A.M. Bruning (1970). "Reversible room-temperature absorption of large quantities of hydrogen by Intermetallic Compounds," Phillips Research Repts. 25.

[18] Z.P. Li, B.H. Liu, K. Arai, N. Morigazaki, S. Suda (2003). "Protide compounds in hydrogen storage systems," Journal of Alloys and Compounds, vol. 356–357, pp. 469–474.

[19] Ponniah Vajeeston (2004). "Theoretical Modeling of Hydrides," Dissertation presented for the degree of Doctor Scientiarum, University of Oslo.

[20] Gary Sandrock (1999). "A panoramic overview of hydrogen storage alloys from a gas reaction point of view," Journal of Alloys and Compounds, vol. 293–295, pp. 877–888.

[21] S. Bliznakov, E. Lefterova, L. Bozukov, A. Popov, P. Andreev (2005). "Techniques for characterization of hydrogen absorbtion/desorbtion in metal hydride alloys," proceedings of the International Workshop: Advanced Techniques for Energy Sources Investigation and Testing, Sofia, Bulgaria.

[22] L. Schlapbach, I. Anderson, J. Burger in: Buschov, K.H.J (1994). "Electronic and Magnetic Properties of Metals and Ceramics," VCH, Weinheim, part II, 331, p. 271.

[23] M. Yamaguchi, E. Akiba, in: Buschov, K.H.J (1994). "Electronic and Magnetic Properties of Metals and Ceramics," VCH, Weinheim, part II, p 334.

[24] J. Huot, C. Julien (2002). "Proc. of New Trends in Intercalation compounds for Energy Storage," Kluwer Academic Publishers, 61, pp. 109.

[25] T.B. Flanagan, W.A. Oates (2005). "Some thermodynamic aspects of metal hydrogen systems," Journal of Alloys and Compounds, vol. 404–406, pp. 16–23.

[26] M. Sastri, B. Vismanathan, S. Srinivasa (1998). “Metal hydrides,” Narosa publishing house, pp. 5, 10.

[27] M. Groll, H.-P. Klein (2002). “Metal hydride technology with special emphasis on thermodynamic machines,” Institut für Kernenergetik und Energiesysteme (IKE), Universität Stuttgart.

[28] M. Ram Gopal and S. Srinivasa Murthy (1995). “Prediction of Metal Hydride Heat Transformer Performance Based on Heat Transfer and Reaction Kinetics,” Ind. Eng. Chem. Res, 34, pp. 2305-2313.

[29] G. D. Sandrock, P. D. Goodell (1984). “Cyclic life of metal hydrides with impure hydrogen: Overview and engineering considerations,” journal of the less common mat. Volume 104, Issue 1, pp. 159-173.

[30] M. Wanner, G. Friedlmeier, G. Hoffmann, M. Groll (1996). “Thermodynamic and Structural Changes of Various Intermetallic Compounds during Extended Cycling in Closed Systems,” Int. Symp. on Metal-Hydrogen Systems, Les Diablerets.

[31] G. Thomas, G. Sandrock (2006). Hydride Information Center, online posting: http://hydpark.ca.sandia.gov.

[32] George G . Libowitz, Herbert F. Hayes & Thomas R. (1957). “The system zirconium-nickel and hydrogen,” Journal Chemistry and Physics, vol. 27, pp. 514.

[33] Amedeo Maddalena, Milo Petris, Petru Palade, Sabrina Sartori, Giovanni Principi, Eliseo Settimo, Bernardo Molinas and Sergio Lo Russo (2006). “Study of Mg-based materials to be used in a functional solid state hydrogen reservoir for vehicular applications,” International Journal of Hydrogen Energy, Volume 31, Issue 14, pp. 2097-2103.

[34] G. Sandrock (2005). “State-of-the-Art Review of Hydrogen storage in reversible metal Hydrides for Military Fuel cell applications,” Final Report for ONR.

[35] G. Sandrock (1995). “Hydrogen Energy System – Production and Utilization of Hydrogen and Future Aspects,” Kluwer Academic, Dordrecht, pp. 135.

[36] Z.P. Li, B.H. Liu, K. Arai, S. Suda (2005). “Development of the direct borohydride fuel cell,” Journal of Alloys and Compounds, vol. 404–406, pp. 648–652.

[37] Emilio Orgaz and Michèle Gupta (1999). “Electronic structure of BaReH9,” Journal of Alloys and Compounds, Volumes 293-295, pp. 217-221.

[38] Darlene K. Slattery and Michael D. Hampton (2002). “Complex Hydrides for Hydrogen Storage,” Proceedings of the 2002 U.S. DOE Hydrogen Program Review.

[39] B. Bogdanović, R. A. Brand, A. Marjanovic, M. Schwickardi, J. Tolle (2000). “Metal-doped sodium aluminium hydrides as potential new hydrogen storage materials,” J. Alloys and Compounds, vol. 302, pp. 36.

[40] Yuko Nakamori, Kazutoshi Miwa, Akihito Ninomiya, Haiwen Li, Nobuko Ohba, Shin-ichi Towata, Andreas Züttel & Shin-ichi Orimo (2006). “Correlation between thermodynamical stabilities of metal borohydrides and cation electronegativites: First-principles calculations and experiments ”, Physical Review B 74, 045126.

[41] International Energy agency (2006). “Hydrogen production and storage,” International Energy Agency (IEA), Head of Publications Service.

[42] Karl Joseph Gross (1998). “Intermetallic materials for hydrogen storage,” Institut de Physique, Universite de Fribourg, Suisse, Doctoral dissertation.

[43] Wojciech Grochala & Peter P. Edwards (2004). “Thermal Decomposition of the Non-Interstitial Hydrides for the Storage and Production of Hydrogen,” Chem. Rev. vol. 104, pp. 1283-□1315.

[44] J. Huot, G. Liang, R. Schulz (2001). “Mechanically alloyed metal hydride systems,” Appl. Phys. A 72, pp. 187–195.

[45] Gagik Barkhordarian, Thomas Klassen, Rudiger Bormann (2006). “Kinetic investigation of the effect of milling time on the hydrogen sorption reaction of magnesium catalyzed with different Nb2O5 contents,” Journal of Alloys and Compounds, vol. 407, pp. 249–255.

[46] Eun Jeon, YoungWhan Cho (2006). “Mechanochemical synthesis and thermal decomposition of zinc borohydride” Journal of Alloys and Compounds, vol. 422, pp. 273–275.

[47] M. Tajbakhsh, M. M. Lakouraj, F. Mohanazadeh & A. Ahmadi-nejhad (2003). “N-Methylpyrrolidine-zinc borohydride: as a new stable and efficient reducing agent in organic synthesis”, Synthetic Communications Vol. 33, No. 2, pp. 229–236.

[48] S.E. Hsu, V.M. Beibutian, M.T. Yeh (2002). “Preparation of hydrogen storage alloys for applications of hydrogen storage and transportation,” Journal of Alloys and Compounds, vol. 330–332, pp. 882–885.

[49] L. K. Heung (2002). “Design of metal hydride vessel for processing tritium,” 6th. International conference on tritium science and technology, Tsukuba, Japan.

[50] Z. Dehouche, N. Grimard, F. Laurencelle, J. Goyette, T.K. Bose (2005). “Hydride alloys properties investigations for hydrogen sorption compressor,” Journal of Alloys and Compounds, vol. 399, pp. 224–236.

[51] Xinhua Wang, Rugan Chen, Yan Zhang, Changpin Chen, Qidong Wang (2006). “Hydrogen storage alloys for high-pressure suprapure hydrogen compressor,” Journal of Alloys and Compounds, vol. 420, pp. 322–325.

[52] The Glassware Gallery. “Planetary ball milling,” online posting, www.ilpi.com/inorganic/glassware/ballmill.html.

[53] Fritsch company. “Pulverisette manual,” online posting, www.fritsch.de/data/prospekte/e_pulverisette6.pdf.

[54] C. Suryanarayana, Marcel Dekker (2005). “Mechanical Alloying and Milling,” Advanced Materials, vol. 17, pp. 2893-2894.

[55] Innovative Technology. “System One Glovebox,” online posting, www.gloveboxes.com.

[56] TA instrument website. “DSC tutorial,” online posting, www.tainstruments.com.

[57] TA instrument website. “SDT tutorial,” online posting, www.tainstruments.com.

[58] Fisk University (2005). “Simultaneous Differential Scanning Calorimetry & Thermogravimetric Analysis Statistical review of world energy,” online posting, www.fisk.edu.

[59] New Mexico tech. “FESEM types of signals,” online posting, http://infohost.nmt.edu/~maximino/fesem_types_of_signals.htm.

[60] ETH Zürich website. “SEM technology,” online posting, www.microscopy.ethz.ch/sem.htm.

[61] Bruce M. Clemens (2006). “GCEP technical report 2006,” online posting, http://gcep.stanford.edu.

[62] Quantachrome instruments web site. “Autosorb1-C Chemisorption - Physisorption Analyzer manual,” online posting, www.quantachrome.com.

[63] Keck Interdisciplinary Surface Science Center (2005). “Fourier Transform Infrared Spectroscopy (FT-IR),” online posting, www.nuance.northwestern.edu.

[64] University of Arizona, department of Chemistry. “Introduction to mass spectrometry,” online posting, http://www.chem.arizona.edu/massspec.

[65] I.I. Bulyk, Yu.B. Basaraba, A.M. Trostianchyn (2004). “Features of the HDDR process in ZrT2 (T = Cr, Mn, Fe, Co) compounds,” Journal of Alloys and Compounds, vol. 367, pp. 283–288.

[66] T. Matsumura, H. Yukawa, M. Morinaga (1998). “Alloying effects on the electronic structure of ZrMn2 intermetallic hydride,” Journal of Alloys and Compounds, vol. 279, pp. 192–200.

[67] T. Kodama (1998). “Proposal for new indexes describing the degree of hysteresis and those applications to the ZrMn2 –H systems,” Journal of Alloys and Compounds, vol. 278, pp. 194–200.

[68] M. Dorogova, T. Hirata, and S. M. Filipek (2003). “Hydrogen-induced volume changes in ZrCr2 and pseudo-binary compounds of ZrCr2, ZrMn2 and ZrV2,” physics state solid, vol. 198, No. 1, pp. 38– 42.

[69] Guanping Li, Nobuyuki Nishimiya(2004). “Phase relations of Zr(FexMn1−x)2–H2 systems studied by XRD and isothermal-calorimetric measurement,” Journal of Alloys and Compounds, vol. 375, pp. 205–211.

[70] L.E.A. Berlouis, N. Comisso, G. Mengoli (2006). “Changes in hydrogen storage properties of binary mixtures of intermetallic compounds submitted to mechanical milling,” Journal of Electroanalytical Chemistry, vol. 586, pp. 105–111.

[71] M. Hara, Y. Hatano, T. Abe, K. Watanabe, T. Naitoh, S. Ikeno, Y. Honda (2003). “Hydrogen absorption by Pd-coated ZrNi prepared by using Barrel-Sputtering System,” Journal of Nuclear Materials, vol. 320, pp. 265–271.

[72] S. Orimo, H. Fujii (1995). “Reactive mechanical grinding of ZrNi under various partial pressures of hydrogen,” Journal of Alloys and Compounds, vol. 217, pp. 287-294.

[73] K. H. J. Buschow (1981). “Thermal behaviour of amorphous alloys of Ni with Zr, Hf and Pr near 40 at % Ni,” Journal of physics, applied physics, vol. 14 pp. 1087- 97.

[74] J.S. Cantrell, R.C. Bowman Jr, L.A. Wade, S. Luo, J.D. Clewley, Ted B. Flanagan (1995). “Thermodynamic properties and the degradation of ZrNiHx at elevated temperatures,” Journal of Alloys and Compounds, vol. 231, pp. 518-523.

[75] P. Dantzer & P. Millet (2001). “Heat flux calorimetry in intermetallic compound-H2(g) systems: heat measurements and modeling in the low pressures range,” Thermochimica Acta 370, pp.1-14.

[76] A. Al-Hajry (2000). “Fast amorphization reaction in ZrNi system prepared by mechanical alloying,” Materials Research Bulletin 35, pp. 1989–1998.

[77] A. I. Zaitsev, N. E. Zaitseva, E. Kh. Shakhpazov & A. A. Kodentsov (2002). “Thermodynamic properties and phase equilibria in the nickel–zirconium system. The liquid to amorphous state transition,” Chem. Phys., vol. 4, pp. 6047–6058.

[78] R.A. Varin, Ch. Chiu (2005). “Structural stability of sodium borohydride (NaBH4) during controlled mechanical milling,” Journal of Alloys and Compounds, vol. 397, pp. 276–281.

[79] Z.P. Li a, B.H. Liu , J.K. Zhu, N. Morigasaki, S. Suda (2006). “NaBH4 formation mechanism by reaction of sodium borate with Mg and H2,” Journal of Alloys and Compounds, not published.

APPENDICES

Appendix A: Zr-Mn XRD profiles

Anchor scan parameters for XRD measurements:

Measurement Date / Time	27-07-2006 13:23:05
Operator	lrivera3
Raw Data Origin	XRD measurement (*.XRDML)
Scan Axis	Gonio
Start Position [°2Th.]	20.0100
End Position [°2Th.]	69.9900
Step Size [°2Th.]	0.0200
Scan Step Time [s]	0.5000
Scan Type	Continuous
Offset [°2Th.]	0.0000
Divergence Slit Type	Fixed
Divergence Slit Size [°]	0.9570
Specimen Length [mm]	10.00
Receiving Slit Size [mm]	0.2500
Measurement Temperature [°C]	25.00
Anode Material	Cu
Generator Settings	45 kV, 40 mA
Goniometer Radius [mm]	320.00
Dist. Focus-Diverg. Slit [mm]	91.00

Pure Zr powder peak list:

Table A.1 Pure Zr XRD peak identification

Pos. [°2Th.]	Height [cts]	FWHM [°2Th.]	d-spacing [Å]	Rel. Int. [%]	Tip width [°2Th.]	Matched by
31.9083	79.96	0.1968	2.80476	19.91	0.2000	03-065-3366
34.7397	105.75	0.1968	2.58237	26.33	0.2000	03-065-3366
36.4454	401.58	0.1181	2.46533	100.00	0.1200	03-065-3366
47.7917	74.64	0.1968	1.90319	18.59	0.2000	03-065-3366
56.7399	70.98	0.3936	1.62247	17.68	0.4000	03-065-3366
63.3469	84.45	0.1968	1.46824	21.03	0.2000	03-065-3366
68.3376	75.64	0.3840	1.37153	18.84	0.3200	03-065-3366

Appendix A: (Continued)

Identified patterns list: 03-065-3366 Zirconium (Zr)

Pure Mn powder peak list:

Table A.2 Pure Mn XRD peak identification

Pos. [°2Th.]	Height [cts]	FWHM [°2Th.]	d-spacing [Å]	Rel. Int. [%]	Tip width [°2Th.]	Matched by
36.4805	12.12	0.4723	2.46304	1.76	0.4800	
40.7510	40.36	0.1968	2.21425	5.85	0.2000	00-001-1237
43.3246	689.91	0.0984	2.08849	100.00	0.1000	00-001-1237
44.6368	22.21	0.9446	2.03010	3.22	0.9600	
48.1320	146.41	0.0984	1.89053	21.22	0.1000	00-001-1237
50.3897	66.49	0.1574	1.81099	9.64	0.1600	00-001-1237
52.6061	97.41	0.0960	1.73836	14.12	0.0800	00-001-1237

Identified patterns list: 00-001-1237 Manganese (Mn)

ZrO_2 peak list:

Table A.3 ZrO_2 XRD peak identification

Pos. [°2Th.]	Height [cts]	FWHM [°2Th.]	d-spacing [Å]	Rel. Int. [%]	Tip width [°2Th.]	Matched by
28.2016	151.18	0.1574	3.16439	83.28	0.1600	00-007-0343
31.5179	181.54	0.1968	2.83860	100.00	0.2000	00-007-0343
34.2009	52.20	0.3936	2.62181	28.76	0.4000	00-007-0343
35.3055	47.46	0.1574	2.54227	26.15	0.1600	00-007-0343
40.7415	31.23	0.2362	2.21474	17.20	0.2400	00-007-0343

Table A.3 (Continued)

44.8495	25.10	0.2362	2.02097	13.82	0.2400	00-007-0343
49.2901	54.02	0.1574	1.84879	29.76	0.1600	00-007-0343
50.2035	63.78	0.3149	1.81727	35.13	0.3200	00-007-0343
54.1689	48.58	0.3149	1.69324	26.76	0.3200	00-007-0343
55.3297	44.80	0.3149	1.66043	24.68	0.3200	00-007-0343
57.2029	20.67	0.3149	1.61043	11.39	0.3200	00-007-0343
59.8766	30.72	0.4723	1.54476	16.92	0.4800	00-007-0343
62.8439	42.49	0.3149	1.47877	23.40	0.3200	00-007-0343
65.7646	23.59	0.6720	1.41882	12.99	0.5600	00-007-0343

Identified patterns list: 00-007-0343 Baddeleyite (ZrO_2)

MnO peak list:

Table A.4 MnO XRD peak identification

Pos. [°2Th.]	Height [cts]	FWHM [°2Th.]	d-spacing [Å]	Rel. Int. [%]	Tip width [°2Th.]	Matched by
35.0100	14.22	0.3149	2.56305	9.84	0.3200	01-075-1090
36.1144	29.36	0.3149	2.48717	20.32	0.3200	
40.5405	144.50	0.2755	2.22525	100.00	0.2800	01-075-1090
44.5032	20.54	0.3149	2.03588	14.22	0.3200	
46.9447	17.86	0.2362	1.93554	12.36	0.2400	
58.6776	36.23	0.3149	1.57343	25.07	0.3200	01-075-1090
59.8891	19.11	0.2362	1.54446	13.22	0.2400	
64.6754	16.95	0.2880	1.44006	11.73	0.2400	

Appendix A: (Continued)

Identified Patterns List: 01-075-1090 Manganosite (MnO)

Zr-Mn manual mixture peak list:

Table A.5 Zr-Mn manual mixture XRD peak identification

Pos. [°2Th.]	Height [cts]	FWHM [°2Th.]	d-spacing [Å]	Rel. Int. [%]	Tip width [°2Th.]	Matched by
32.0113	124.01	0.1968	2.79597	22.34	0.2000	01-089-3045; 01-089-2105
34.8827	128.77	0.1378	2.57211	23.20	0.1400	01-089-3045; 01-089-2105
36.5527	555.11	0.1378	2.45834	100.00	0.1400	01-089-3045
40.6384	5.66	0.9446	2.22012	1.02	0.9600	01-089-2105
43.1647	135.39	0.2362	2.09586	24.39	0.2400	01-089-2105
47.9867	110.28	0.2362	1.89591	19.87	0.2400	01-089-3045; 01-089-2105
50.2317	15.79	0.2362	1.81632	2.84	0.2400	01-089-2105
52.4238	20.93	0.2362	1.74542	3.77	0.2400	01-089-2105
54.7287	5.00	0.9446	1.67724	0.90	0.9600	
56.9045	79.84	0.1968	1.61817	14.38	0.2000	01-089-3045; 01-089-2105
63.4633	68.61	0.1574	1.46582	12.36	0.1600	01-089-3045
68.4008	70.44	0.1968	1.37156	12.69	0.2000	01-089-3045; 01-089-2105
69.4754	53.66	0.4320	1.35183	9.67	0.3600	01-089-3045

Appendix A: (Continued)

Identified patterns list: 01-089-3045 Zirconium (Zr), 01-089-2105 Manganese (Mn)

Zr-Mn ball milled for 10h peak list:

Table A.6 Zr-Mn bm-10h XRD peak identification

Pos. [°2Th.]	Height [cts]	FWHM [°2Th.]	d-spacing [Å]	Rel. Int. [%]	Tip width [°2Th.]	Matched by
32.7719	12.55	0.6298	2.73279	28.84	0.6400	
43.5803	43.52	0.7872	2.07683	100.00	0.8000	00-001-1237
48.4451	6.85	1.1520	1.87749	15.74	0.9600	00-001-1237

Identified patterns list: 00-001-1237 Manganese (Mn)

Zr-Mn Ball milled for 24h peak list:

Table A.7 Zr-Mn bm-24h XRD peak identification

Pos. [°2Th.]	Height [cts]	FWHM [°2Th.]	d-spacing [Å]	Rel. Int. [%]	Tip width [°2Th.]	Matched by
43.1858	33.15	0.7872	2.09489	100.00	0.8000	00-001-1237
47.6927	6.84	1.1520	1.90534	20.65	0.9600	00-001-1237

Identified patterns list: 00-001-1237 Manganese (Mn)

Zr-Mn Ball milled 48h and annealed peak list:

Table A.8 Zr-Mn bm48h-annealed XRD peak identification

Pos. [°2Th.]	Height [cts]	FWHM [°2Th.]	d-spacing [Å]	Rel. Int. [%]	Tip width [°2Th.]	Matched by
28.3015	120.67	0.1574	3.15346	64.02	0.1600	03-065-3159

Table A.8 (Continued)

30.3926	94.27	0.1574	2.94108	50.01	0.1600	01-079-1771
31.5546	94.40	0.1968	2.83538	50.08	0.2000	03-065-3159
34.1307	188.50	0.0984	2.62704	100.00	0.1000	$ZrMn_2$
35.3556	28.27	0.2362	2.53879	15.00	0.2400	01-079-1771
39.5532	149.62	0.1378	2.27850	79.37	0.1400	$ZrMn_2$
40.5908	31.74	0.4723	2.22261	16.84	0.4800	03-065-3159
43.0585	151.75	0.2755	2.10078	80.50	0.2800	03-065-3159; 01-079-1771
44.6285	34.09	0.7872	2.03046	18.08	0.8000	$ZrMn_2$
47.8063	30.19	0.3149	1.90265	16.02	0.3200	03-065-3159
50.2409	31.16	0.2362	1.81601	16.53	0.2400	03-065-3159; 01-079-1771
54.1223	11.41	0.3149	1.69459	6.05	0.3200	01-079-1771
55.5288	16.69	0.3149	1.65495	8.85	0.3200	
57.1810	89.92	0.3360	1.60967	47.70	0.2800	

Identified patterns list: 01-079-1771 Zirconium oxide (ZrO2), 03-065-3159 Manganese (Mn).

Plot of Identified Phases:

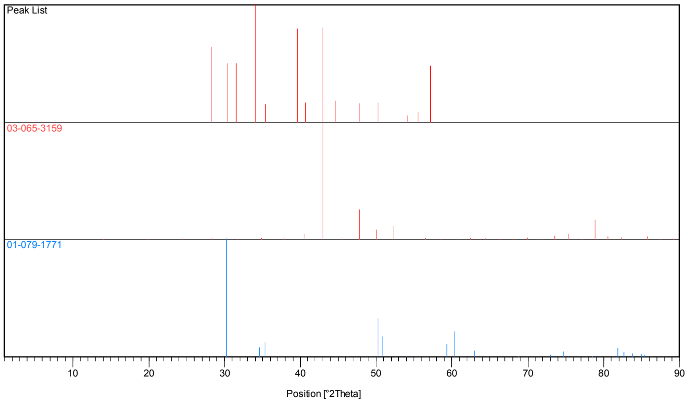

Figure A.1 XRD identified phases of Zr-Mn mixture ball milled 48h and annealed

Appendix B: ZrNi alloy XRD profiles

Anchor scan parameters for XRD measurements:

Comment	Z=3.980mm
Measurement Date / Time	29-08-2006 11:00:59
Operator	lrivera3
Raw Data Origin	XRD measurement (*.XRDML)
Scan Axis	Gonio
Start Position [°2Th.]	20.0100
End Position [°2Th.]	69.9900
Step Size [°2Th.]	0.0200
Scan Step Time [s]	0.5000
Scan Type	Continuous
Offset [°2Th.]	0.0000
Divergence Slit Type	Fixed
Divergence Slit Size [°]	0.9570
Specimen Length [mm]	10.00
Receiving Slit Size [mm]	0.2500
Measurement Temperature [°C]	25.00
Anode Material	Cu
Generator Settings	45 kV, 40 mA
Goniometer Radius [mm]	320.00

ZrNi 30/70 peak list:

Table B.1 ZrNi 30/70 XRD peak identification

Pos. [°2Th.]	Height [cts]	FWHM [°2Th.]	d-spacing [Å]	Rel. Int. [%]	Tip width [°2Th.]	Matched by
29.4360	25.31	0.2362	3.03445	7.82	0.2400	
37.8379	54.12	0.2362	2.37774	16.73	0.2400	03-065-0041
38.6156	41.03	0.3936	2.33163	12.69	0.4000	
44.8654	323.42	0.1378	2.02029	100.00	0.1400	03-065-0041
46.8393	52.67	0.3936	1.93965	16.29	0.4000	03-065-0041
68.4834	20.51	0.6720	1.36897	6.34	0.5600	03-065-0041

Identified patterns list: 03-065-0041 Nickel Zirconium ($ZrNi_5$)

Appendix B: (Continued)

ZrNi 70/30 peak list:

Table B.2 ZrNi 70/30 XRD peak identification

Pos. [°2Th.]	Height [cts]	FWHM [°2Th.]	d-spacing [Å]	Rel. Int. [%]	Tip width [°2Th.]	Matched by
27.0076	121.07	0.2362	3.30151	23.77	0.2400	01-089-2626
32.6411	348.47	0.3149	2.74344	68.42	0.3200	03-065-0745
34.1168	509.34	0.3936	2.62807	100.00	0.4000	01-089-2626
35.5275	97.13	0.1574	2.52689	19.07	0.1600	
36.3363	276.95	0.3542	2.47248	54.37	0.3600	01-089-2626; 03-065-0745
40.4072	135.04	0.3149	2.23229	26.51	0.3200	01-089-2626; 03-065-0745
42.2083	336.70	0.2755	2.14111	66.10	0.2800	01-089-2626
45.9443	12.45	0.6298	1.97532	2.44	0.6400	01-089-2626
52.0253	58.29	0.4723	1.75784	11.44	0.4800	01-089-2626; 03-065-0745
55.5107	86.79	0.5510	1.65545	17.04	0.5600	01-089-2626; 03-065-0745
56.7617	89.61	0.7085	1.62190	17.59	0.7200	01-089-2626
59.7082	6.14	0.9446	1.54871	1.20	0.9600	01-089-2626
62.6216	28.99	0.6298	1.48348	5.69	0.6400	03-065-0745
67.9655	63.73	0.9600	1.37813	12.51	0.8000	01-089-2626; 03-065-0745

Identified patterns list: 01-089-2626 Nickel zirconium hydride ($ZrNiH_3$), 03-065-0745 Zirconium hydride (ZrH_2)

ZrNi(1:1) hand mix peak list:

Table B.3 ZrNi(1:1) hand mix XRD peak identification

Pos. [°2Th.]	Height [cts]	FWHM [°2Th.]	d-spacing [Å]	Rel. Int. [%]	Tip width [°2Th.]	Matched by
21.6140	238.38	0.3936	4.11164	69.83	0.4000	01-071-0543
23.8186	39.96	0.4723	3.73583	11.71	0.4800	01-071-0543
26.9380	76.50	0.3149	3.30989	22.41	0.3200	03-065-1405
29.5852	30.15	0.1968	3.01949	8.83	0.2000	01-071-0543
32.5442	236.09	0.2755	2.75139	69.16	0.2800	03-065-0745; 01-071-0543
33.9308	341.37	0.2755	2.64206	100.00	0.2800	03-065-1405; 00-049-1690
35.3529	76.62	0.2362	2.53897	22.44	0.2400	00-049-1690; 01-071-0543
36.2344	192.70	0.3149	2.47921	56.45	0.3200	03-065-1405; 03-065-0745
37.9498	65.23	0.1574	2.37099	19.11	0.1600	
38.5475	82.85	0.2362	2.33559	24.27	0.2400	00-049-1690; 01-071-0543
40.3496	110.69	0.1968	2.23534	32.42	0.2000	03-065-1405; 03-065-0745; 01-071-0543
42.0627	242.10	0.3936	2.14818	70.92	0.4000	03-065-1405; 00-049-1690
43.4724	87.12	0.1574	2.08174	25.52	0.1600	01-071-0543
44.9694	267.84	0.0720	2.01419	78.46	0.0600	01-071-0543
45.4788	81.93	0.1968	1.99445	24.00	0.2000	03-065-1405; 01-071-0543

Table B.3 (Continued)

46.9181	68.79	0.2755	1.93657	20.15	0.2800	01-071-0543
51.8574	44.51	0.4723	1.76314	13.04	0.4800	03-065-1405
55.2574	64.82	0.6298	1.66244	18.99	0.6400	03-065-1405; 03-065-0745; 01-071-0543
56.9186	59.64	0.7085	1.61780	17.47	0.7200	03-065-1405; 01-071-0543
60.0083	12.31	0.4723	1.54168	3.61	0.4800	01-071-0543
62.6993	22.57	0.4723	1.48183	6.61	0.4800	03-065-0745; 01-071-0543
67.8772	48.98	0.9600	1.37971	14.35	0.8000	03-065-1405; 03-065-0745; 01-071-0543

Identified patterns list: 03-065-1405 Nickel zirconium hydride ($ZrNiH_3$), 03-065-0745 Zirconium hydride (ZrH_2), 00-049-1690 Zriconium nickel (Zr_3Ni_2), 01-071-0543 Zirconium nickel (Zr_2Ni_7)

ZrNi (1:1) ball milled 12h+annealed peak list:

Table B.4 ZrNi (1:1) ball milled 12h+annealed XRD peak identification

Pos. [°2Th.]	Height [cts]	FWHM [°2Th.]	d-spacing [Å]	Rel. Int. [%]	Tip width [°2Th.]	Matched by
28.1684	220.10	0.0787	3.16805	53.35	0.0800	03-065-1359; 01-078-1807
31.4722	129.03	0.1574	2.84262	31.28	0.1600	01-078-1807
33.8591	412.53	0.1378	2.64749	100.00	0.1400	
35.2718	25.36	0.3149	2.54462	6.15	0.3200	01-078-1807
36.2287	105.24	0.1968	2.47958	25.51	0.2000	03-065-1359

Table B.4 (Continued)

36.9584	174.98	0.0787	2.43228	42.42	0.0800	
37.8895	66.41	0.1968	2.37463	16.10	0.2000	
39.3156	345.84	0.0984	2.29171	83.83	0.1000	01-078-1807
40.3226	117.82	0.1378	2.23678	28.56	0.1400	
40.8278	36.68	0.2362	2.21026	8.89	0.2400	01-078-1807
42.7509	227.61	0.1771	2.11518	55.17	0.1800	03-065-1359
44.0876	22.53	0.2362	2.05410	5.46	0.2400	03-065-1359
44.7672	72.54	0.1968	2.02449	17.58	0.2000	03-065-1359; 01-078-1807
45.5304	17.93	0.2362	1.99231	4.35	0.2400	01-078-1807
47.4169	19.87	0.1574	1.91736	4.82	0.1600	
49.2500	41.53	0.3149	1.85020	10.07	0.3200	01-078-1807
50.1466	57.33	0.1968	1.81920	13.90	0.2000	01-078-1807
51.2775	23.27	0.3149	1.78171	5.64	0.3200	01-078-1807
53.9705	24.80	0.3936	1.69899	6.01	0.4000	03-065-1359; 01-078-1807
55.3688	32.95	0.3149	1.65935	7.99	0.3200	03-065-1359; 01-078-1807
56.8062	191.13	0.3149	1.62073	46.33	0.3200	
59.9265	39.72	0.2755	1.54359	9.63	0.2800	03-065-1359; 01-078-1807
62.7455	19.87	0.3149	1.48085	4.82	0.3200	01-078-1807
65.0748	35.90	0.2362	1.43337	8.70	0.2400	01-078-1807
67.7797	115.00	0.3840	1.38146	27.88	0.3200	

Identified Patterns List: 03-065-1359 Zirconium nickel (ZrNi), 01-078-1807 Zirconium oxide (ZrO_2)

Appendix B: (Continued)

ZrNi(1:1) ball-milled12h+annealed+hydride peak list:

Table B.5 ZrNi(1:1) ball-milled12h+annealed+hydride XRD peak identification

Pos. [°2Th.]	Height [cts]	FWHM [°2Th.]	d-spacing [Å]	Rel. Int. [%]	Tip width [°2Th.]	Matched by
28.2260	21.15	0.2362	3.16172	6.76	0.2400	00-012-0478
33.7747	122.69	0.2362	2.65391	39.19	0.2400	01-089-4768
36.4175	130.82	0.3149	2.46715	41.79	0.3200	00-012-0478
37.2787	43.82	0.3149	2.41211	14.00	0.3200	
39.1975	106.71	0.2755	2.29835	34.08	0.2800	00-012-0478; 01-089-4768
39.7774	32.67	0.2362	2.26617	10.43	0.2400	
42.9968	313.08	0.2755	2.10365	100.00	0.2800	00-012-0478
45.0527	83.00	0.3936	2.01232	26.51	0.4000	00-012-0478
50.4048	11.39	0.6298	1.81049	3.64	0.6400	
56.6237	61.09	0.4723	1.62552	19.51	0.4800	00-012-0478; 01-089-4768
59.9983	5.01	0.9446	1.54191	1.60	0.9600	00-012-0478
62.8404	6.69	0.9446	1.47884	2.14	0.9600	
65.3961	38.03	0.7872	1.42710	12.15	0.8000	
67.4055	34.34	0.6720	1.38822	10.97	0.5600	01-089-4768

Identified patterns list: 00-012-0478 Zirconium nickel (ZrNi), 01-089-4768 Zirconium oxide (ZrO)

Appendix B: (Continued)

ZrNi 70/30 hydride peak list:

Table B.6 ZrNi 70/30 hydride XRD peak identification

Pos. [°2Th.]	Height [cts]	FWHM [°2Th.]	d-spacing [Å]	Rel. Int. [%]	Tip width [°2Th.]	Matched by
26.7849	39.09	0.2362	3.32846	18.82	0.2400	03-065-1405
32.3963	207.70	0.2755	2.76361	100.00	0.2800	01-073-2076
33.8893	194.31	0.2755	2.64520	93.55	0.2800	03-065-1405
35.2627	34.65	0.2362	2.54526	16.68	0.2400	
36.1744	136.75	0.1968	2.48318	65.84	0.2000	03-065-1405; 01-073-2076
37.1457	59.53	0.1968	2.42045	28.66	0.2000	
40.2485	70.73	0.4723	2.24072	34.06	0.4800	03-065-1405; 01-073-2076
41.9232	138.64	0.3936	2.15501	66.75	0.4000	03-065-1405
51.9266	41.76	0.3149	1.76095	20.11	0.3200	03-065-1405; 01-073-2076
55.3492	69.64	0.6298	1.65989	33.53	0.6400	03-065-1405; 01-073-2076
56.6286	52.85	0.7085	1.62539	25.45	0.7200	03-065-1405
62.5649	35.23	0.7872	1.48469	16.96	0.8000	01-073-2076
67.9988	55.66	0.8640	1.37754	26.80	0.7200	03-065-1405; 01-073-2076

Identified patterns list: 03-065-1405 Zirconium nickel ($ZrNiH_3$), 01-073-2076 Zirconium hydride (ZrH_2)

Plot of Identified Phases:

Appendix B: (Continued)

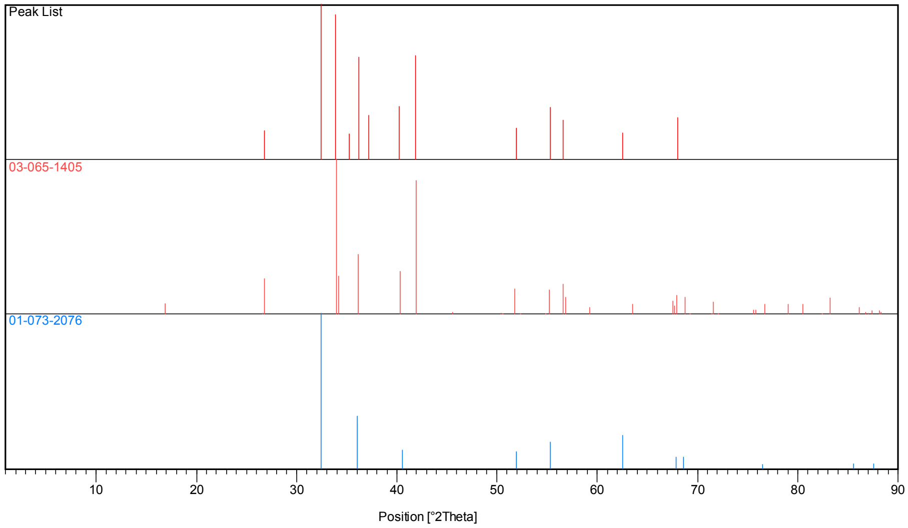

Figure B.1 XRD identified phases of ZrNi 70/30 hydride

Appendix C: Enthalpy calculation of ZrNi 70/30

The ZrNi 70/30 enthalpy (ΔH) is evaluated from the slope of the straight line plot of ln P_{H2} vs 1/T according to the following equations (Van't Hoff equation) as is shown in chapter 3:

$$\ln \frac{P_2}{P_1} = \ln P_2 - \ln P_1 = \frac{-\Delta H}{R}\left[\frac{1}{T_2} - \frac{1}{T_1}\right] \tag{C.1}$$

$$\Delta H = -R \frac{(\ln P_2 - \ln P_1)}{\left[\frac{1}{T_2} - \frac{1}{T_1}\right]} \tag{C.2}$$

The PCT desorption plateau pressures from Figure 5.20 at different temperatures is tabulated in Table C.1

Table C.1 Plateau pressures at different desorption temperatures for ZrNi 70/30

Temp. (C)	T(K)	Pressure(bar)	(atm)
300	573	1.5	1.48038
325	598	3	2.96076
350	623	5	4.9346
375	648	7.2	7.105824
395	668	10.08	9.948154

In Table C.2 is shown the inversed of the temperature of the plateau pressures and the natural log (ln) of the pressures in which the plateau occurs.

Table C.2 Inversed of the temperature and ln of the pressure at different plateau pressures

1/T (K^{-1})	ln (pressure)
0.003333333	0.392298812
0.003076923	1.085445992
0.002857143	1.596271616
0.002666667	1.960914729
0.002531646	2.297386966

A linear approximation was made in Microsoft excel software to approximate the 1/T vs ln pressure plot (Table C.2) into a linear graph. The result is show in Figure C.1

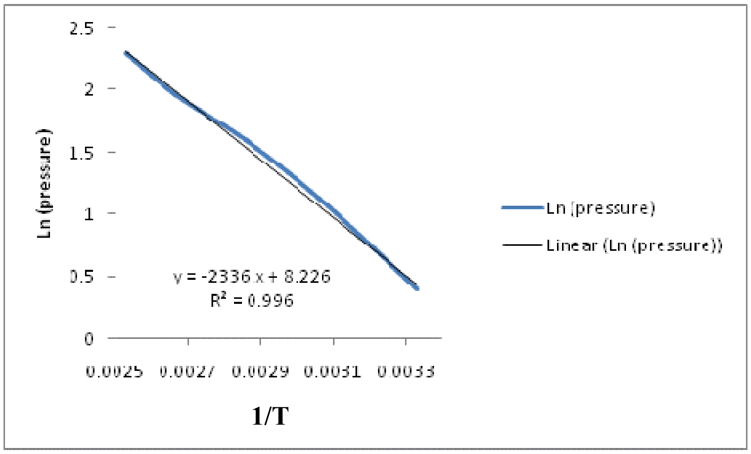

Figure C.1 Result and linear approximation of the natural log of the pressure vs inversed of temperature

As it was shown, the slope of the linear approximation in Figure C.1 is equal to ΔH/R, therefore ΔH is equal to 19.4215 kJ/mol, in terms of H_2 release, it must be multiplied by two, remaining ΔH equals to 38.84 kJ/molH_2